

UC San Diego

UC San Diego Electronic Theses and Dissertations

Title

An experimental study of a vertical tube gas-fluidized bed

Permalink

<https://escholarship.org/uc/item/8ws840r0>

Author

Mandich, Kevin Matthew

Publication Date

2010

Peer reviewed|Thesis/dissertation

UNIVERSITY OF CALIFORNIA, SAN DIEGO

An Experimental Study of a Vertical Tube Gas-Fluidized Bed

A thesis submitted in partial satisfaction of the requirements for the degree Master of
Science

in

Engineering Sciences (Mechanical Engineering)

by

Kevin Matthew Mandich

Committee in charge:

Professor Robert Cattolica, Chair
Professor Joe Goddard
Professor Daniel Tartakovsky

2010

The thesis of Kevin Matthew Mandich is approved, and it is acceptable in quality and form for publication on microfilm and electronically:

Chair

University of California, San Diego

2010

Table of Contents

Signature Page.....	iii
Table of Contents.....	iv
List of Symbols.....	vi
List of Figures.....	viii
List of Tables.....	xi
Preface.....	xii
Abstract.....	xv
1 Fluidized Bed Fundamentals.....	1
1.1 Flow Regimes.....	1
1.2 Particle Characterization.....	4
1.3 Pressure Drop Across a Fluidized Bed.....	6
1.4 Bed Height and Expansion Ratio.....	8
1.5 Predicted Value of Minimum Fluidization Velocity.....	9
2 Granular Temperature Theory.....	13
2.1 Characterization of Granular Flows.....	13
2.2 The Extension of Kinetic Theory to Granular Flows.....	14
2.3 Acoustic Shot Noise Method	18
2.4 Experimental Determination of Granular Temperature Near The Wall..	21
2.5 Summary of Computational Methods.....	25
3 Experimental Investigations.....	32
3.1 Bed Material Characterization and Determination of Particle Dimensions.....	32
3.2 Experimental Setup.....	36
3.3 Note on Pressure Probe Design and Maintenance.....	44
3.4 Distributor Plate Design.....	45
3.5 Pressure Drop and Minimum Fluidization Measurements.....	49
3.6 Bed Height and Mean Expansion Ratio Measurements.....	51
3.7 Determination of Average Transfer Function.....	52
3.8 Acoustic Shot Noise Measurement.....	54
4 Results.....	56
4.1 Pressure Drop, Void Fraction, and Minimum Fluidization Velocity.....	56
4.2 Bed Expansion Ratio.....	64
4.3 Cylinder Transfer Function.....	73
4.4 Mean-Squared Acceleration at the Wall.....	77

4.5	Average Particle Normal Velocity.....	81
4.6	Comparison of Particle Normal Velocity with Simulation.....	85
5	Conclusions.....	92
	Appendix A: Data Acquisition System.....	94
	Appendix B: Experimental and Simulated Particle Normal Velocity Plots.....	99
	References.....	103

List of Symbols

a^2	Experimental mean-squared acceleration at the wall
a_m^2	Total mean-squared acceleration at the wall
a_n^2	Mean-squared acceleration at the wall due to noise
ΔA	Area of prescribed element of cylinder wall [m ²]
A	Total surface area of cylinder wall under consideration [m ²]
A_o	Open orifice area of the distributor plate [m ²]
A_d	Total area of the distributor plate [m ²]
A_f	Cross-sectional area of flow through bed cylinder [m ²]
Ar	Archimedes number, dimensionless
$c(r, t)$	Instantaneous particle velocity [ms ⁻¹]
$C_{d,or}$	Orifice drag coefficient, dimensionless
c_w	Dimensionless quantity comparing inertial and gravitational forces, used in flow regime diagram
d	Drag constant, dimensionless
d_p	Mean particle diameter [m]
d_t	Inner diameter of bed tube [m]
d_{or}	Diameter of orifice holes in distributor plate [m]
f_a	Arrival frequency of particles [s ⁻¹]
$F(t, R_i)$	Time-dependent force caused by particle impact [N]
$F(f, R_j)$	Frequency-dependent particle impact force
g_i	Gravitational acceleration [ms ⁻²]
g_o	Radial distribution function at contact, dimensionless
h	Expanded bed height [m]
\bar{h}	Mean expanded bed height [m]
\bar{h}_{max}	Mean maximum expanded bed height [m]
h_{mf}	Expanded bed height at minimum fluidization [m]
\bar{h}_{min}	Mean minimum expanded bed height [m]
$H(f, R_i)$	Transfer function determined from excitation of accelerometer at location R due to impulsive force at location R_i
I^2	Integral of the average transfer function of the cylinder
k_o	Ratio of open orifice area to total area of the distributor plate, dimensionless
m	Total mass of bed material [kg]
m_{part}	Mean mass of a particle [kg]
N	Number of prescribed elements of cylinder wall, dimensionless
Δp_b	Pressure drop across the fluidized bed [Pa]
Δp_d	Pressure drop across the distributor plate [Pa]
P	Pressure [Pa]
$Re_{p,mf}$	Particle Reynolds number at fluidization, dimensionless
Re_t	Reynolds number of flow through fluidization tube, dimensionless

$S_a(f, R_i)$	Power spectrum of wall acceleration at location R_i
$S_F(f, R_j)$	Power spectrum of particle impact force
t, T	Time [s]
\mathbf{u}	Velocity vector [ms^{-1}]
U_s	Superficial gas velocity [ms^{-1}]
U_{mf}	Superficial gas velocity at minimum fluidization [ms^{-1}]
v_n	Particle velocity in the direction normal to the cylinder wall [ms^{-1}]
$v(r, t)$	Mean hydrodynamic velocity of a particle [ms^{-1}]
$w(r, t)$	Fluctuation velocity of a particle [ms^{-1}]
x	Coordinate [m]

Greek Letters

$\bar{\delta}$	Mean bed expansion ratio, dimensionless
$\delta(H)$	Bed expansion ratio, dimensionless
$\delta(t)$	Dirac delta function
$\Delta\delta$	Relative mean height of fluctuations, dimensionless
ε	Volume fraction, dimensionless
ε_0	Void fraction at packing, dimensionless
ε_{mf}	Void fraction at minimum fluidization conditions, dimensionless
Θ	Granular temperature, [m^2s^{-2}]
μ	Dynamic viscosity of gas (atmospheric air at standard conditions) [$\text{kgm}^{-1}\text{s}^{-1}$]
ρ_B	Bulk density of fluid-solid mixture [kgm^{-3}]
ρ_g	Density of gas (atmospheric air at standard conditions) [kgm^{-3}]
ρ_s	Mass density of solid particles [kgm^{-3}]
φ_s	Mean sphericity of particles, dimensionless
Ω	Dimensionless quantity used in flow regime diagram

List of Figures

1.1 Vertical fluidized bed schematic depicting possible flow regimes.....	2
1.2 Geldart particle classification diagram.....	5
1.3 Ideal pressure drop graphs as a function of superficial gas velocity.....	7
1.4 Ideal void fraction behavior of a fluidized bed as a function of superficial gas velocity.....	8
1.5 Flow regime diagram for vertical fluidized beds.....	11
2.1 Granular flow regimes.....	14
2.2 Sample plot of instantaneous particle velocity as a function of time.....	15
2.3 Energy cascade diagram showing dissipation in granular flows	17
2.4 Visualization of instantaneous particle velocity component normal to the wall.....	19
2.5 Schematic of impulse force application at a location relative to the accelerometer.....	22
3.1 Images of each particle type used in experiment.....	33
3.2 Geldart diagram overlaid with markings corresponding to the particles tested.....	35
3.3 CAD drawing of the fluidized bed, including outer support structure.....	38
3.4 Schematic of pressure tap system.....	39
3.5 CAD drawing of acrylic fixture used to attach accelerometer to the wall.....	40
3.6 Schematic of the experimental setup	42
3.7 CAD drawing of distributor plate used for Glass Spheres material.....	48
3.8 CAD drawing of distributor plate used for EconoProp material.....	48
3.9 CAD drawing of distributor plate used for CarboHSP material	49
3.10 Calibration curve of the P1 pressure transducer.....	50
3.11 Photograph of accelerometer attachment to fluidized bed wall	54
4.1 Pressure drop over mean bed height vs. superficial gas velocity for Glass Spheres material.....	56
4.2 Pressure drop over mean bed height vs. superficial gas velocity for EconoProp material.....	57
4.3 Pressure drop over mean bed height vs. superficial gas velocity for CarboHSP material.....	58
4.4 Pressure drop over mean bed height vs. normalized gas velocity for all materials.....	59

4.5 Void fraction vs. superficial gas velocity for Glass Spheres material.....	60
4.6 Void fraction vs. superficial gas velocity for EconoProp material.....	60
4.7 Void fraction vs. superficial gas velocity for CarboHSP material.....	61
4.8 Void fraction vs. normalized gas velocity for all materials.....	62
4.9 Flow regime diagram for vertical fluidized beds, overlaid with markings corresponding to each material.....	63
4.10 Mean bed expansion ratio vs. normalized gas velocity for Glass Spheres material.....	65
4.11 Mean bed expansion ratio vs. normalized gas velocity for EconoProp material.....	65
4.12 Mean bed expansion ratio vs. normalized gas velocity for CarboHSP material.....	66
4.13 Comparison between experiment and simulation of mean bed expansion ratio for Glass Spheres material.....	68
4.14 Comparison between experiment and simulation of mean bed expansion ratio for EconoProp material.....	70
4.15 Comparison between experiment and simulation of mean bed expansion ratio for CarboHSP material.....	71
4.16 Time signals of impulse hammer and accelerometer, along with corresponding transfer function.....	73
4.17 Squared transfer function determined at various locations on the cylinder..	74
4.18 Transfer function determined at different circumferential positions of the cylinder	75
4.19 Power spectral density of the accelerometer signal taken with the bed at rest.....	78
4.20 Power spectral density of accelerometer signals at various gas velocities for Glass Spheres material.....	79
4.21 Power spectral density of accelerometer signals at various gas velocities for EconoProp material.....	79
4.22 Power spectral density of accelerometer signals at various gas velocities for CarboHSP material.....	80
4.23 Particle normal velocity vs. superficial gas velocity for Glass Spheres material.....	81
4.24 Particle normal velocity vs. superficial gas velocity for EconoProp material.....	82

4.25 Particle normal velocity vs. superficial gas velocity for CarboHSP material.....	82
4.26 Particle normal velocity vs. normalized gas velocity for all materials.....	84
4.27 Comparison between experiment and simulation of particle normal velocity for Glass Spheres material.....	86
4.28 Comparison between experiment and simulation of particle normal velocity for EconoProp material.....	88
4.29 Comparison between experiment and simulation of particle normal velocity for CarboHSP material.....	90

List of Tables

3.1 Composition, by percentage, of each bed material used in this experiment.....	32
3.2 Comparison between published and experimentally-determined mean particle diameters.....	34
3.3 Experimentally-determined values of mean surface area and particle mass for each material.....	36
3.4 Correlation between fluidization chamber Reynolds number and orifice drag coefficient.....	46
3.5 Calculated pressure drops and corresponding number of orifices used in each distributor plate.....	48
4.1 Comparison of minimum fluidization values determined through experiment and theory.....	64
4.2 I^2 values computed with the cylinder filled with each material type, along with an empty cylinder.....	76

Preface

This project was undertaken at the University of California, San Diego as part of a biomass-to-liquid alcohol project sponsored by the U.C. Discovery program and West Biofuels, LLC. The thermo-chemical conversion of feedstock into a producer gas mixture, the first major step in this process, takes place in a circulating gas-fluidized bed. It is of interest to understand the fluidization characteristics of the bed materials used in this system. The goal of this experimental work is to investigate methods of measuring important fluidization properties in a simplified vertical tube gas-fluidized bed. These measurements can be used to test models for predicting fluidization in a full-scale industrial system.

The experimental apparatus used consists of a 1.22*m* polycarbonate tube of inner diameter 8.26*cm* filled halfway with a granular bed material. Experiments were conducted using three particle types, each having separate mean particle diameters and densities, with the latter two being candidate bed materials for full-scale operations. With the introduction of pressurized air through a porous plate beneath the bed, various regimes of fluidization were observed. The pressure drop across the bed and the distributor plate, mean bed height, and minimum fluidization velocity were determined through non-invasive measurement techniques and compared with well-established theories to verify the performance of the experimental setup.

A quantity of great interest, granular temperature near the wall, was also determined under various fluidization conditions. An extension of kinetic gas theory to granular flows provides a method for estimating the average particle velocity

fluctuations inside a fluidized bed. An Acoustic Shot Noise probe, developed by Cody et al. (1996), provides a non-invasive method of correlating the vibrational energy at the wall to the average particle velocity normal to this surface through the use of a mechanical transfer function. The transfer function of the cylinder wall was determined by performing an impulse-response analysis between an impact of known force and the corresponding response measured by a wall-mounted accelerometer. Using this information, an estimate of the average granular temperature near the wall was obtained through a spectral analysis of the wall acceleration time signal, which was recorded while the system was under fluidization.

Experimentally-determined values of pressure drop, mean bed height, and minimum fluidization velocity agreed well with predicted values. Average granular temperature values also agreed with those obtained in previous similar experiments. The mean bed expansion ratio and average granular temperature data sets were compared with those obtained from a Computational Fluid Dynamics simulation (Didwania et al., to appear). The computational model was developed from MFIx-based code (Syamlal et al., 1993). Good agreement between experiment and simulation was obtained for various combinations of four main parameters found in the model: solid phase stress model, boundary conditions at the fluidized bed wall, particle-particle restitution coefficient, and particle-wall restitution coefficient. Simulations performed using the Princeton (Srivastava and Sundaresan, 2003) solid phase stress model achieved more accurate results than those using the Schaeffer (Schaeffer, 1987) model. The partial-slip Johnson and Jackson boundary condition at the wall (Johnson and Jackson, 1987) yielded better results than the free-slip condition

when implemented into the model. The particle-particle and particle-wall restitution coefficients used for which the computer model achieved the most accurate results were 0.85 and 0.9, respectively.

ABSTRACT OF THE THESIS

An Experimental Study of a Vertical Tube Gas-Fluidized Bed

by

Kevin Matthew Mandich

Master of Science in Engineering Sciences (Mechanical Engineering)

University of California, San Diego 2010

Professor Robert Cattolica, Chair

The goal of this experimental work was to investigate methods of measuring important fluidization properties in a vertical, cold-flow, gas-fluidized bed to gain an understanding of the fluidization characteristics of the bed materials used. Quantities such as pressure drop across the bed, mean bed height, and minimum fluidization velocity were determined using non-invasive methods and were compared to fundamental fluidized bed theories to verify proper performance of the experiment. Granular temperature near the wall, a quantity of great interest in this system, was also

determined using a non-invasive technique. An Acoustic Shot Noise probe, developed by Cody et al. (1996), was used to correlate the vibrational energy at the fluidized bed wall to the average particle velocity normal to this surface. By determining the mechanical transfer function of the confining tube, it was possible to obtain an estimate for the granular temperature near the wall by performing a spectral analysis of the wall acceleration time signal. Experimentally-determined values of pressure drop, mean bed height, and minimum fluidization velocity agreed well with the values predicted from theory. Average granular temperature values also agreed well with those obtained through similar means (Cody et al., 1996). The mean bed expansion ratio and average granular temperature results were compared with those obtained from a Computational Fluid Dynamics simulation (Didwania et al., to appear). Good agreement was observed between experiment and simulation, and special attention was given to the effects of changing key parameters in the model.

1. Fluidized Bed Fundamentals

Fluidized beds are characterized by their high rates of mixing between the fluid and solid phases. It is for this reason that these systems exhibit high rates of heat and mass transfer between the phases, and are thus desirable for use in various physical and chemical processes. Upon fluidization, the weight of the bed material is balanced by the pressure drop across the bed. This results in a fluid-like behavior of the solid phase, hence the name “fluidized bed.”

There is a large amount of published theory on fluidized beds and their behavior. Particle and flow regime classifications form the basis of any fluidized bed experiment. The theory (Kunii, 1991) regarding pressure drop across the fluidized bed, mean bed height, and minimum fluidization velocity proves to be invaluable to the successful design and validation of an associated experiment.

1.1 Flow Regimes

A simple setup of a fluidized bed is shown in Figure 1.1. The particulate phase, consisting of the bed material, is confined by the sides of the cylindrical tube and rests on top of a porous plate. With the introduction of a pressurized gas through the porous plate, various flow regimes are possible, depending on the average velocity of the gas. Figure 1.1 illustrates the range of flow regimes possible in a vertical fluidized bed.

The superficial gas velocity, U_s , is defined as the volumetric flow rate of the gas through the tube divided by the cross-sectional area of the fluidized bed, A_f . At

low values of superficial gas velocity (pre-fluidization), the gas flows through the interstitial spaces between the particles. The pressure drop across the bed, Δp_b , increases linearly with U_s but is not large enough to balance the bed weight $m_{bed}g$, where m_{bed} is the mass of the bed and g is the gravitational acceleration constant. This fixed bed is illustrated in Figure 1.1(a).

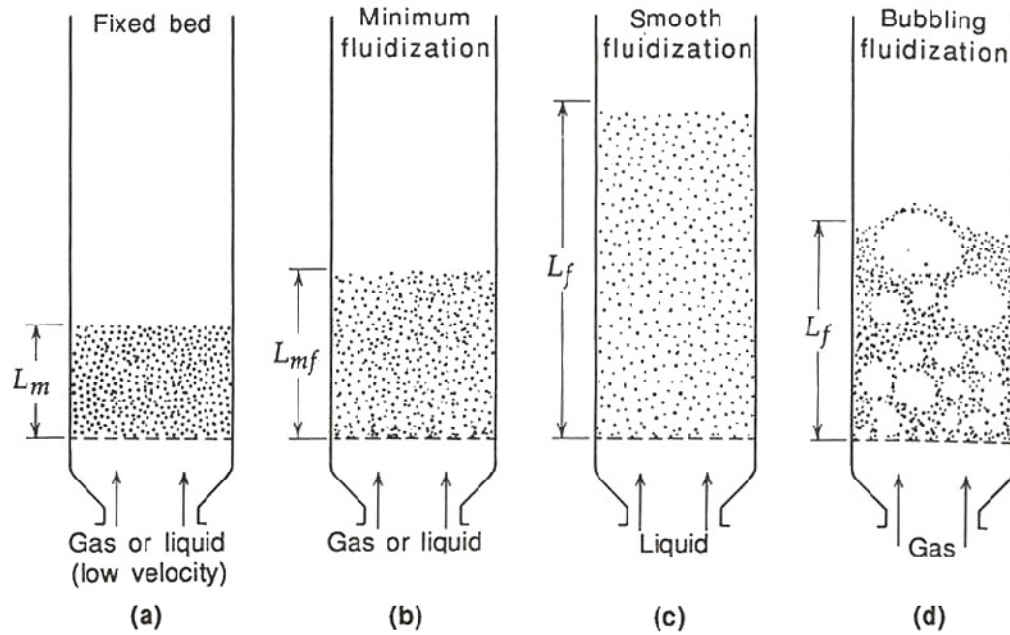


Figure 1.1: Basic vertical fluidized bed schematic depicting possible flow regimes. Kunii (1991)

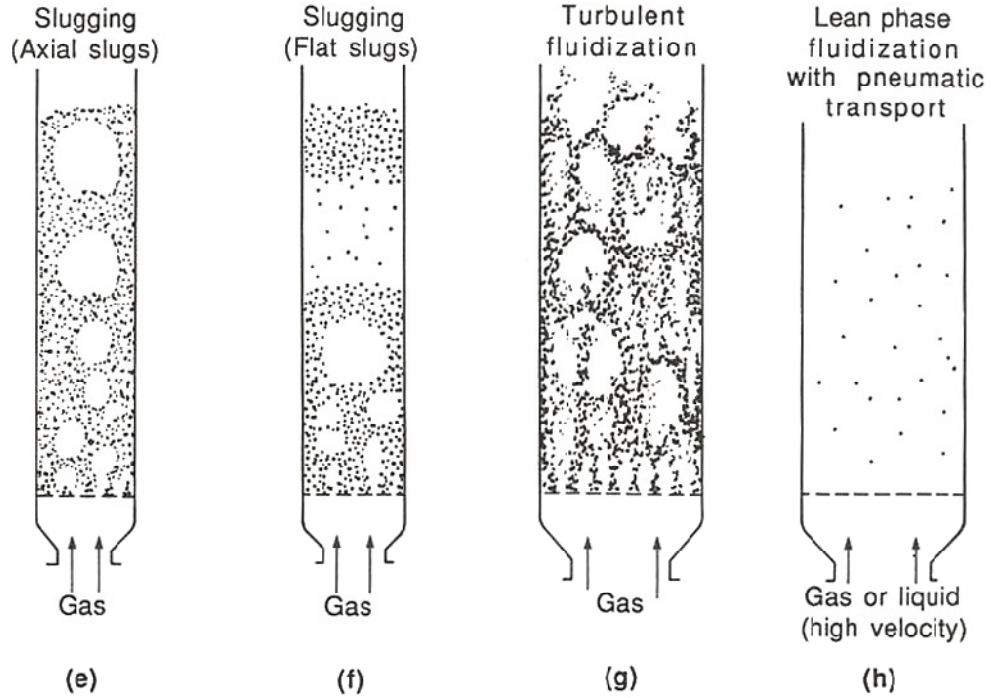


Figure 1.1: Basic vertical fluidized bed schematic depicting possible flow regimes. Kunii (1991)

Raising the superficial gas velocity until the pressure drop equals the bed weight, $\Delta p_b = mg$, yields minimum fluidization, exhibited in Figure 1.1(b). Here, the superficial gas velocity is defined as the minimum fluidization velocity, U_{mf} . As mentioned, the particle phase begins to behave like a fluid.

Further increasing U_s yields various flow regimes of increasing intensity. Initially, the bed will continue to expand as shown in Figure 1.1(c). Bubbling occurs either at the onset of fluidization or shortly thereafter (Figure 1.1(d)), depending on particle and gas properties. The velocity at which bubbles are first present is U_{mb} , the minimum bubbling velocity. For sufficiently narrow beds at higher gas velocities, slugs may begin to form. This occurs when the diameters of the bubbles approach that

of the confining tube, as illustrated in Figure 1.1(e). As seen in Figure 1.1(f), large enough slugs may lift portions of the bed.

The next regime is described by turbulent motion of the bed (Figure 1.1(g)). Here, the clearly-defined upper surface of the bed visible in the previous regimes disappears. With a high enough superficial gas velocity, the drag force from the fluid will match the weight of each particle. This is known as pneumatic transport, illustrated by Figure 1.1(h).

The flow regimes tested in this experiment range from the low-velocity fixed bed to the flat slug regime seen in Figure 1.1(f). Turbulent fluidization and pneumatic transport occur at superficial gas velocities beyond those which are tested in this experiment.

1.2 Particle Characterization

Particles exhibit varying fluidization behaviors based on their solid density ρ_s and mean diameter d_p . Geldart (1973) constructed a helpful and widely-used classification of bed materials based on the mean particle diameter and the difference between the fluid and solid phase densities, $\rho_s - \rho_g$.

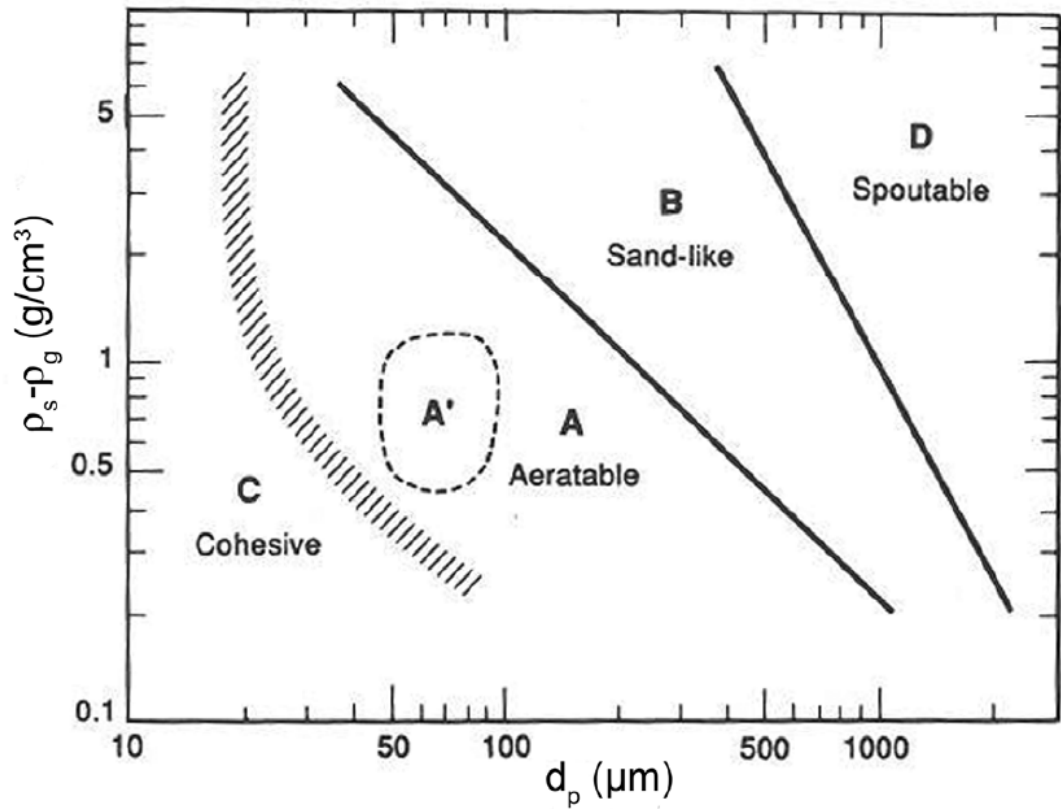


Figure 1.2: Geldart particle classification diagram. Geldart (1973)

There are four main classes of particles, as shown in Figure 1.2, which is valid for fluidization using atmospheric air. Geldart B particles include the type of materials most commonly found in industrial fluidized beds. This type of particle exhibits bubbling right at the onset of fluidization ($U_{mb} = U_{mf}$). Most types of beach sand can be found in this category. Geldart A particles are smaller and lighter than those from group B, and generally fluidize at lower superficial gas velocities. Upon minimum fluidization, beds of this material type undergo smooth, homogenous expansion. A further increase in gas velocity is required to obtain bubbling.

Particles in the Geldart C domain are extremely light and small. An example is a fine powder, such as flour. Fluidization of this particle type is difficult due to the fact that cohesive forces between particles tend to be higher than the drag forces imparted onto the particles by the fluid. Geldart D materials, on the other hand, are large and dense. Particles in this domain tend to exhibit spouting when a pressurized gas is introduced, making fluidization very difficult.

The particles used in the current experiment all lie within the Geldart B domain. These were chosen due to the ease with which fluidization using these particles is possible, along with the fact that their sizes and densities are commonly used in industrial applications.

1.3 Pressure Drop Across a Fluidized Bed

As previously mentioned, the pressure drop across the bed is linearly proportional to the superficial gas velocity up until the point of minimum fluidization. After this point, the weight of the solid phase is balanced by the pressure drop over the bed. This is expressed by the following relation:

$$\frac{\Delta p_b}{\bar{h}} = (1 - \varepsilon)(\rho_s - \rho_g)g \quad (1.1)$$

Here, ε is the void fraction, and \bar{h} is the average bed height which will be defined shortly. The void fraction can be expressed in terms of the solid density and the bulk density of the solid-fluid mixture, ρ_B :

$$\varepsilon = 1 - \frac{\rho_B}{\rho_s} = 1 - \frac{m_{bed}}{\rho_s A_f \bar{h}} \quad (1.2)$$

After the point of minimum fluidization, the pressure drop across the bed remains constant, while the average height of the bed increases with U_s . This is illustrated in

Figure 1.3.

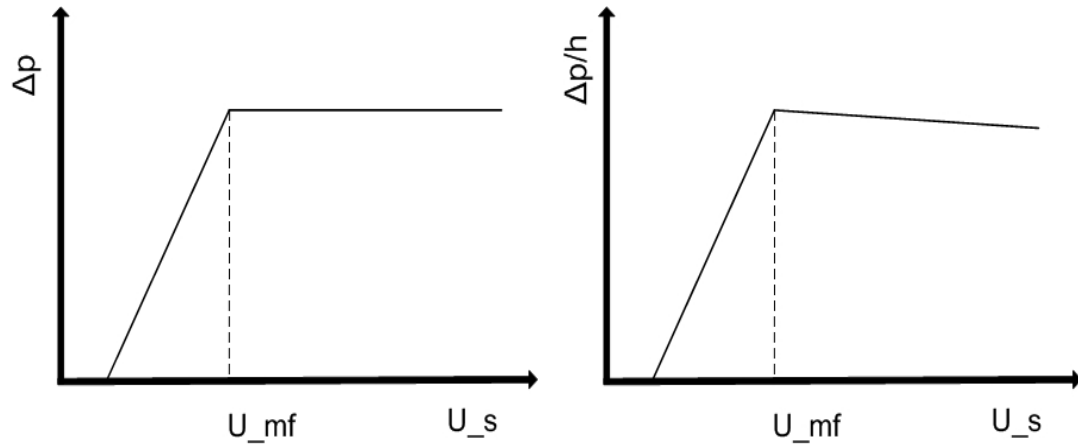


Figure 1.3: Ideal pressure drop of a fluidized bed as a function of superficial gas velocity (Left); Ideal pressure drop over average bed height as a function of superficial gas velocity (Right)

Indeed, the quantity $\Delta p_b / \bar{h}$ is seen to drop after minimum fluidization. This follows from the fact that the mean bed height continues to rise after this point. The minimum fluidization velocity can be easily determined by recording pressure drop values at various gas velocities. Connecting the two linear sections, as shown in Figure 1.3, yields the desired value of U_{mf} .

Similarly, plotting values of void fraction versus superficial gas velocity yields another estimate of the minimum fluidization velocity. The average bed height and, thus, void fraction, remain constant until the onset of fluidization, as seen in Figure 1.4.

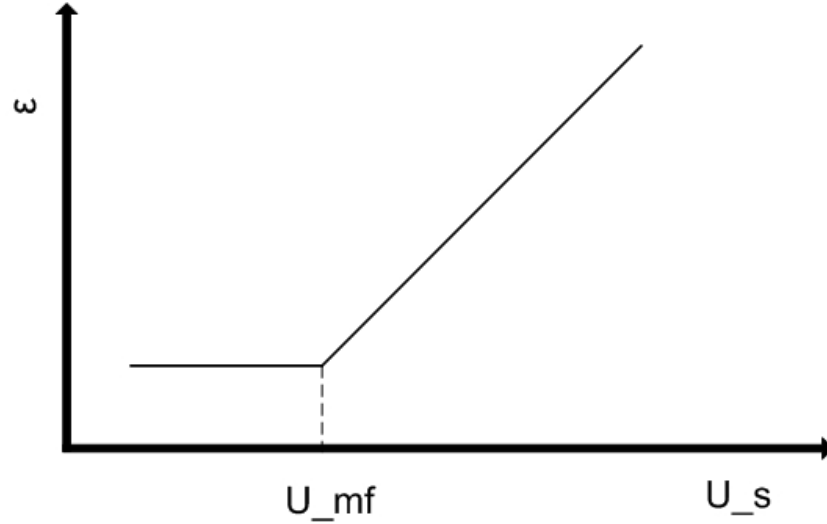


Figure 1.4: Ideal void fraction behavior of a fluidized bed as a function of superficial gas velocity

1.4 Bed Height and Expansion Ratio

The bed height h of a fluidized bed is defined as the distance from the porous plate to the upper surface of the bed. It is well-established (Kunii, 1991) that the bed height is constant prior to minimum fluidization, and begins to rise when $U_s = U_{mf}$. Thus, plotting bed height versus superficial gas velocity is another method through which one can determine the minimum fluidization velocity. As the current experiments stay well within the slugging regime of fluidization, the upper surface is always well-defined. A parameter which is very useful in verifying CFD simulations is known as the bed expansion ratio. Following Reuge et al. (2008), this value is defined as

$$\delta(h) = \frac{h - h_{mf}}{h_{mf}} \quad (1.3)$$

Here, h_{mf} is the bed height at the onset of fluidization. The average bed height, \bar{h} , is defined as the mean of the average maximum and minimum bed heights, \bar{h}_{max} and \bar{h}_{min} . As bubbles and slugs move throughout the bed, it follows naturally that the upper surface of the bed will fluctuate. Visual inspection and recording of several values of the maximum and minimum bed heights, more accurately described as the release and buildup of bubbles, respectively, will yield averages of these values. From this one can easily determine the average bed height, $0.5(\bar{h}_{max} + \bar{h}_{min})$. Following from this is the mean bed expansion ratio, defined as

$$\bar{\delta} = \delta \left(\frac{\bar{h}_{max} + \bar{h}_{min}}{2} \right) = \delta(\bar{h}) \quad (1.4)$$

Another useful parameter is the relative fluctuation height, given by

$$\Delta\delta = \delta(\bar{h}_{max}) - \delta(\bar{h}_{min}) \quad (1.5)$$

It follows from Figure 1.1 that both the mean bed expansion ratio and the relative fluctuation height will increase with superficial gas velocity.

1.5 Predicted Value of Minimum Fluidization Velocity

As mentioned, fluidization begins when the weight of the bed is balanced by the pressure drop across the fluidized bed. The pressure drop through a bed of mean height \bar{h} , assuming a single diameter size d_p of isotropic solid particles, has been correlated by Ergun (1952) as:

$$\frac{\Delta p_b}{\bar{h}} g = 150 \frac{(1 - \varepsilon)^2}{\varepsilon^3} \frac{\mu U_{mf}}{(\phi_s d_p)^2} + 1.75 \frac{1 - \varepsilon}{\varepsilon^3} \frac{\rho_g U_{mf}^2}{\phi_s d_p} \quad (1.6)$$

Here, μ is the dynamic viscosity of the fluid and ϕ_s is particle sphericity, defined as the ratio of the surface area of a sphere to the surface area of a particle having the same volume. Particle sphericity values range from 0 to 1, with a perfect sphere having $\phi_s=1$. Combining this equation with the pressure drop equation (1.1) yields a quadratic in U_{mf} :

$$\frac{d_p^3 \rho_g (\rho_s - \rho_g) g}{\mu^2} = \frac{1.75}{\varepsilon_{mf}^3 \phi_s} Re_{p,mf}^2 + \frac{150(1 - \varepsilon_{mf})}{\varepsilon_{mf}^3 \phi_s^2} Re_{p,mf} \quad (1.7)$$

where $Re_{p,mf} = \frac{d_p U_{mf} \rho_g}{\mu}$ is the particle Reynolds number at minimum fluidization.

Following Kunii (1991), in the case of small particles, such that $Re_{p,mf} \ll 20$, equation 1.7 simplifies to:

$$U_{mf} = \frac{d_p^2 (\rho_s - \rho_g) g}{150 \mu} \frac{\varepsilon_{mf}^3 \phi_s^2}{1 - \varepsilon_{mf}} \quad (1.8)$$

This small-particle estimate is used to verify experimentally-determined values of U_{mf} since each of the particle types tested fall within the desired Reynolds number range.

Other useful tools for estimating the minimum fluidization velocity include flow regime diagrams. An example of such a diagram from Reh (1968) is shown in Figure 1.5. This log-log plot can be helpful in determining which regime of fluidization a system may be under, given certain operating conditions. The Archimedes number Ar , for example, which is constant for a particular gas-particle system, can be used to estimate the minimum fluidization velocity of a system by finding the corresponding particle Reynolds number Re_p . The Archimedes number is defined as the ratio of gravitational to viscous forces:

$$Ar = \frac{d_p^3(\rho_s - \rho_g)\rho_g g}{\mu^2} \quad (1.9)$$

By locating the intersection of the constant Ar value with the point at which the bed transitions from fixed to fluidized (here, where $\varepsilon=0.4-0.5$), one can locate the particle Reynolds number at fluidization, and thus the minimum fluidization velocity.

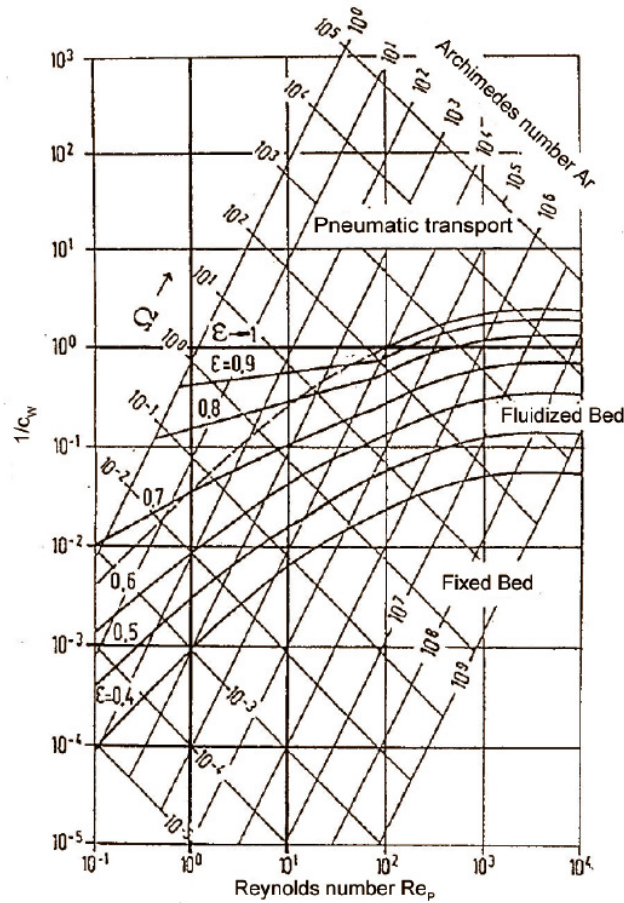


Figure 1.5: Flow regime diagram for vertical fluidized beds. Reh (1968)

The other non-dimensional terms, Ω and $1/c_w$, are defined, but not used to estimate the minimum fluidization velocity:

$$\Omega = \frac{\rho_g^2 U^3}{(\rho_s - \rho_g) g \mu} \quad (1.10)$$

$$1/c_w = \frac{3U^2\rho_g}{4(\rho_s - \rho_g)d_pg} \quad (1.11)$$

2. Granular Temperature Theory

The average granular temperature of the particles in a gas-fluidized bed is a key quantity associated with the CFD modeling of such flows. These granular flows involve random particle motion and, as such, are analogous in several ways to the random molecular motion in a gas. It follows that the kinetic theory of gases may be extended to the granular temperature of the system under investigation, while taking care to note the similarities and differences between the two.

The characterization of granular flows will be discussed, followed by an extension of kinetic theory to the modeling of granular temperature, along with a summary of the computational modeling of granular flows. Finally, a description of the Acoustic Shot Noise (ASN) probe method, which is used to experimentally determine the average granular temperature near the wall, will be discussed.

2.1 Characterization of Granular Flows

Granular flows are defined by the interaction between a continuous fluid phase and a solid particulate phase. The solid, or granular, phase experiences forces and stresses imparted by the fluid phase. Depending on the stresses produced by the continuous fluid phase moving through the interstitial spaces between the particles, one of several granular flow regimes may be defined. Figure 2.1 provides a visualization of the possible regimes in granular flows, as described by Ranade (2002).

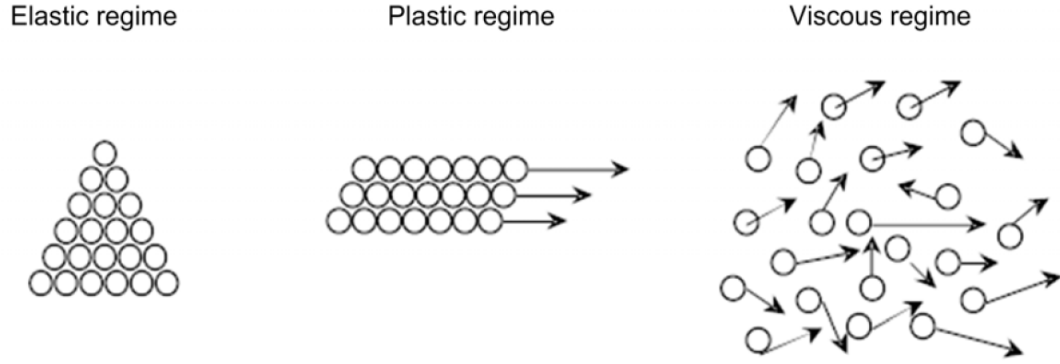


Figure 2.1: Granular flow regimes. Kravanja (2008)

The elastic regime is as the name implies: the solid particle phase acts like an elastic solid, returning to its initial configuration following the release of an applied stress. Likewise, the plastic regime is described by a plastic deformation due to an applied stress, much like that of a solid material. In the viscous regime, which is of interest to the current investigation, particle motion is random, similar to the chaotic motion of molecules in a gas. It is for this reason that this regime is known as “rapid granular flow,” coined by Campbell (1990). It appears natural to extend the kinetic theory of gases, which describes molecular motion and trajectories, to the model of a viscous granular flow.

2.2 The Extension of Kinetic Theory to Granular Flow

To begin, the instantaneous velocity vector of a particle \mathbf{c} at a location \mathbf{r} and time t is defined as $\mathbf{c}(\mathbf{r}, t)$. Taking the ensemble average yields the particle drift velocity at location \mathbf{r} , $\mathbf{V}(\mathbf{r}, t)$, where $\mathbf{V}(\mathbf{r}, t) = \langle \mathbf{c}(\mathbf{r}, t) \rangle$. This is equivalent to the mean velocity of the bulk material. $\mathbf{V}(\mathbf{r}, t)$ is manifested in the visible bulk upward

and downward flow of particles corresponding to slugging in a fluidized bed. The fluctuation velocity (not distinguishable by the human eye), whose ensemble average is zero by definition, is given by:

$$w(r, t) = c(r, t) - V(r, t) \quad (2.1)$$

Figure 2.2 shows a visualization of the particle velocity decomposition at a given time.

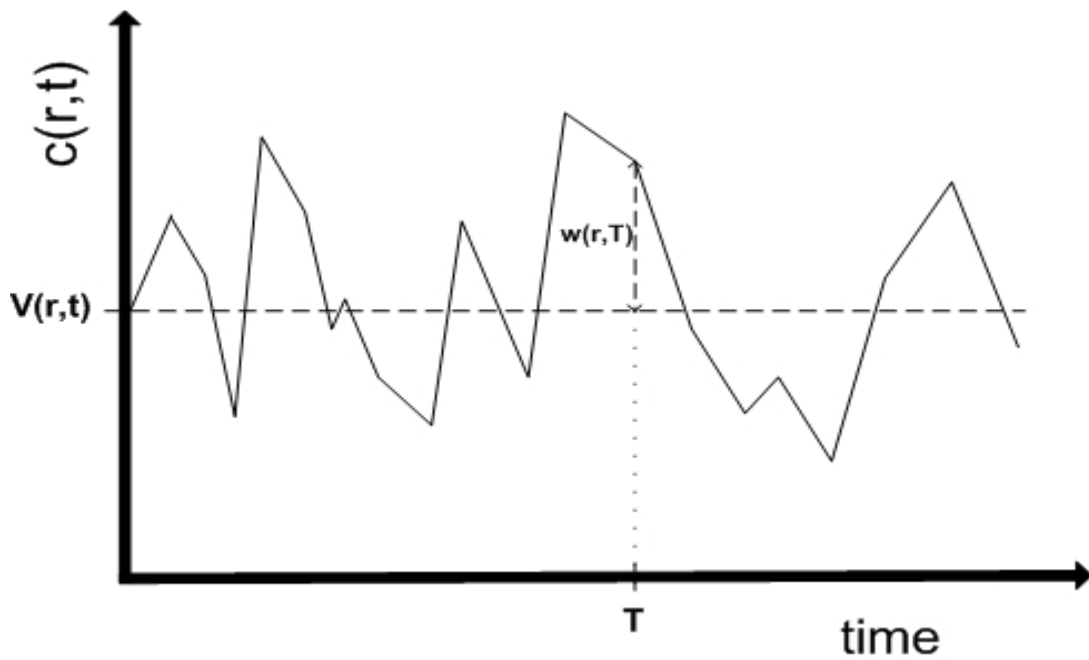


Figure 2.2: Sample plot of instantaneous particle velocity c versus time, with mean bulk velocity V and fluctuation velocity w

As the mean of the fluctuations is equal to zero, it is necessary to describe the intensity of particle velocity fluctuations by the average of its square, just as the thermodynamic temperature of a gas is defined. This mean square velocity of the fluctuations in a granular flow is analogous to the kinetic energy of molecular motion

in a gas. The granular temperature Θ is given by the ensemble average of the squared fluctuation velocity:

$$\Theta = \frac{1}{3} \langle \mathbf{w}(\mathbf{r}, t)^2 \rangle = \frac{1}{3} [\langle \mathbf{c}(\mathbf{r}, t)^2 \rangle - [\mathbf{V}(\mathbf{r}, t)]^2] \quad (2.2)$$

In the case of fluidized beds,

$$\langle \mathbf{c}(\mathbf{r}, t)^2 \rangle \gg [\mathbf{V}(\mathbf{r}, t)]^2 \quad (2.3)$$

implying that the mean square of the instantaneous particle velocity contributes the most to granular temperature. The granular temperature can be expressed by one component of $\langle \mathbf{c}(\mathbf{r}, t)^2 \rangle$ with the assumptions of isotropy and spatial uniformity. Since the quantity of interest is granular temperature near the wall, and since granular temperature in this experiment was determined from vibrational energy at the wall, the chosen component of \mathbf{c} is that which is normal to the wall. Denoting this velocity as $V_n(\mathbf{r}, t)$, the granular temperature may be written as:

$$\Theta = \frac{1}{3} \langle \mathbf{w}(\mathbf{r}, t)^2 \rangle \approx \langle V_n(\mathbf{r}, t)^2 \rangle \quad (2.4)$$

$$\Theta = V_n^2 \quad (2.5)$$

The granular temperature plays a key role in modeling the behavior of particles in a granular flow. Similar to the temperature described in a gas, the granular temperature of this type of system generates a pressure resulting from the impact due to random particle motion. It is this impact which is used to determine the granular temperature, as will be described shortly. As Campbell (1990) and Gidaspow (1994) have pointed out, the role of the analogous temperatures is the determination of important parameters, such as effective viscosity, which can be described through the use of the generated pressure.

It is important to note the differences between granular temperature and the thermodynamic temperature of a gas. First, Θ is not a thermodynamic property, as in a gas, but rather a function of the viscous and inertial forces imparted by the fluid phase. The kinetic theory of gases enforces the equipartition of energy and the Maxwell-Boltzmann velocity distribution. Kinetic theory assumes elastic collisions between molecules; the same is not true for granular flows. Energy is dissipated by particle-particle and particle-wall collisions, and compensation is required for the energy that is lost in this way. This follows from the notion that the granular temperature of this system remains constant. Campbell (1990) described an energy cascade showing how energy is dissipated in granular flows, as visualized in **Figure 2.3**.

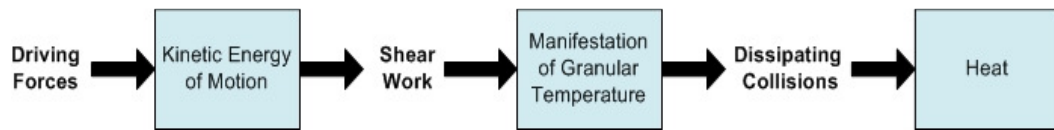


Figure 2.3: Energy cascade diagram showing dissipation in granular flows

As shown, the driving forces (e.g. gas pressure) bring energy into the system, which is transformed into the kinetic energy of the fluid molecules. The shear work which defines the regime of granular flow transforms the kinetic energy into the random particle motion, or granular temperature. Inelastic particle-particle and particle-wall collisions act to further disperse energy into the form of heat. As will be described shortly, the restitution coefficients between particle-particle and particle-wall collisions are two of the key parameters needed to fit the computational model.

Also worth noting is the difference between mean-free paths of molecules in a gas and particles in a rapid granular flow. It is generally known that the mean-free path of a molecule in a gas under moderate conditions is several orders of magnitude higher than its diameter. Dense granular flows, however, have mean-free paths that are on the same order of magnitude of the particle diameters (Cody et al. 1996).

Another difference pointed out by Campbell (1990) is the fact that gases need not have a driving force to have a temperature. Granular temperature, however, is dependent on this driving force and cannot exist without it.

Despite the differences between the temperature of a granular flow and that of a gas, the granular temperature remains one of the most important concepts in modeling and describing the behavior of this type of flow.

2.3 Acoustic Shot Noise Method

As mentioned, granular temperature is one of the most important quantities for understanding and describing the behavior of granular flows, in particular the dynamics of fluidized beds. It is therefore important to be able to verify granular temperature values which are determined through computational modeling. The method employed in this project is a non-invasive probe, first explored by Cody et al. (1996) that relates the vibrational energy at the wall to the average granular temperature of particles near the wall. An overview of this method is given, with particular attention paid to the correlation between wall acceleration and particle velocity normal to the wall.

The Acoustic Shot Noise (ASN) probe developed by Cody et al. (1996) is a non-invasive method of measuring the granular temperature inside a gas-fluidized bed. This acoustic sensor was pioneered in 1996 (Cody et al. 1996) on a laboratory-scale fluidized bed. Further work in 2000 (Cody et al. 2000) included employment of the technique to industrial-scale applications. The granular temperature results obtained were verified using several different experimental techniques that measured particle velocity and granular temperature, as will be discussed.

As previously mentioned, the component of the instantaneous particle velocity vector $\mathbf{c}(\mathbf{r}, t)$ that is of interest is the particle velocity normal to the wall, V_n . When fluidized, the particles in a bed will fluctuate and some will collide with the wall of the bed, as shown in Figure 2.4.

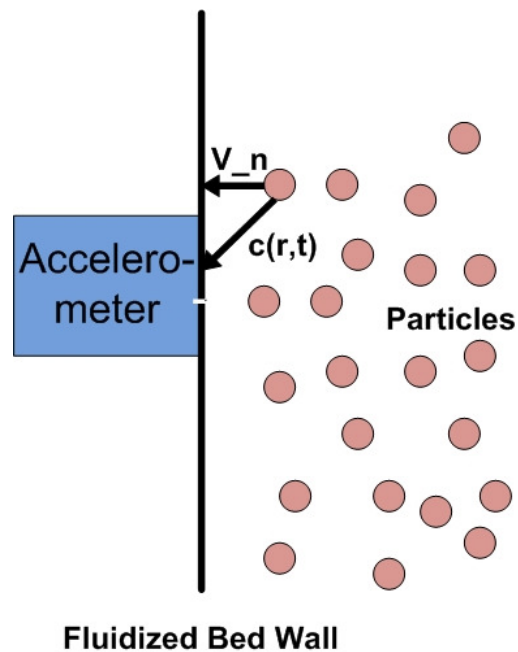


Figure 2.4: Visualization of instantaneous particle velocity, and velocity component normal to the fluidized bed wall

With a wall-mounted accelerometer capturing acceleration data in the direction normal to the wall, the vibrational energy caused by random particle impact may be recorded. This excitation of the vibrational energy at the wall is the basis of the ASN probe. The particle velocity on the bed side of the wall and the wall vibrations outside of the bed are proportional to the momentum transferred through the wall. This allows for the measurement of the particle velocity normal to the wall in the form of wall acceleration.

Random particle collisions are the cause of acoustic noise. Fluctuations in a measured acceleration signal resulting from these random collisions are dominated by this noise. Following the comparison of granular motion to the molecular motion in gases, one can consider the acoustic shot noise caused by random molecular collisions an analogous phenomenon. As pointed out by Cody et al. (1996), if the sensitivity of the human ear were much higher, the shot noise caused by gas molecules would create a constant hissing noise due to random impacts on our ear drums. Similarly, one is incapable of detecting the minor, extremely rapid wall perturbations caused by individual particles colliding with the surface of the fluidized bed wall. One would instead register the large-scale, low-frequency vibrations caused, for example, by slugging, much as one's ear registers large pressure fluctuations caused by a loud noise.

To separate the wall vibrations caused by particle impact and those caused by other sources, it is necessary to display the signal in terms of its frequency components. In general, influences such as structural vibrations and slugging inside the bed take place on different time scales than those caused by particle impact. A

frequency domain analysis of the wall accelerometer time signal will be able to separate these causes due to their different frequency components. For a random signal such as the type under investigation, it is customary to obtain the power spectral density (PSD) of the time signal. The PSD of a random function is obtained by taking the Fourier transform of the signal's autocorrelation function (van der Ziel, 1970). Analysis of the PSD of the wall acceleration signal was used to obtain an estimate of the average particle normal velocity.

2.4 Experimental Determination of Granular Temperature Near the Wall

Defining the momentum transfer Δi caused by a particle of mass m_{part} colliding elastically with the fluidized bed wall, we write:

$$\Delta i = 2m_{part}V_n \quad (2.6)$$

Landau (1970) noted that the power spectral density resulting from particles between 50-500 μm in diameter traveling between 1-100cm/s is estimated to be of constant magnitude up to 300kHz, corresponding to white noise in this frequency range. To determine the time-dependent force $F(t)$ caused by a particle impact on an area element ΔA , the Dirac delta function $\delta(t)$ can be used in this frequency range:

$$F(t) = \sum_i 2m_{part}V_n\delta(t - t_i) \quad (2.7)$$

where m_{part} is the mean particle mass. Assuming a uniformly-distributed particle arrival time T' with a number of particles $f_a T'$, where f_a is the arrival frequency of particles, the time-averaged force resulting from random impact is:

$$\langle F(t) \rangle = 2m_{part}V_n f_a \quad (2.8)$$

Evaluation of the power spectrum of $F(t)$ yields the frequency-dependent force acting on a cylinder element ΔA :

$$S_F(f, R_i) = (2m_{part}V_n)^2 f_a = 4m\rho_B V_n^3 \Delta A \quad (2.9)$$

where the dilute gas expression $f_a = \rho_B V_n \Delta A$ is used, along with the bed mass density $\rho_m = m_{part}\rho_B$. Here, R_i is the element corresponding to ΔA .

To calculate the wall response, we introduce a transfer function $H(t, R_{ij})$ which relates the time response of acceleration at the wall at location R_i , $a(t, R_i)$, to that of an impulsive force $F(t, R_j)$, at location R_j , through convolution. As noted, the force resulting from random particle impacts is expected to be independent of frequency. The acceleration response $a(t, R_i)$ depends on the momentum transfer caused by particle collision and the response of the structure to this stimulus. The usual impulse-response analysis, illustrated in Figure 2.5, is used to determine the frequency-dependent transfer function.

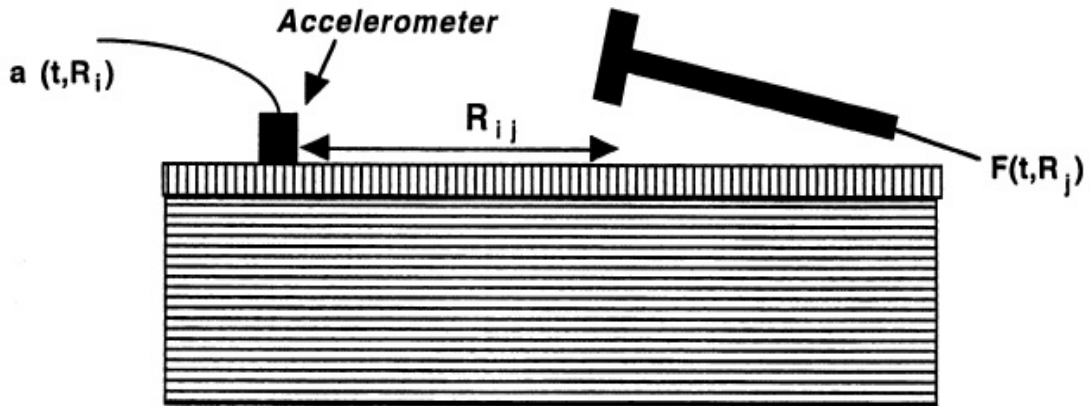


Figure 2.5: Impulse force at location R_j measured by accelerometer at location R_i . Cody et al. (2000)

An expression of the transfer function in frequency space is given by:

$$a(f, R_i) = H(f, R_{ij})F(f, R_j) \quad (2.10)$$

along with the corresponding power spectrum representation (van der Ziel, 1970):

$$S_a(f, R_i) = |H(f, R_{ij})|^2 S_F(f, R_j) \quad (2.11)$$

Substituting the expression relating the power spectrum of the accelerometer signal to the particle normal velocity and summing over all surface elements yields the equation:

$$S_a(f, R_i) = \sum_j |H(f, R_{ij})|^2 (4m\rho_m V_n^3 \Delta A) \quad (2.12)$$

Averaging over the entire wall surface yields the expression:

$$S_a(f, 0) = \langle |H(f)|^2 \rangle \langle 4m\rho_B V_n^3 \rangle A = \langle |H(f)|^2 \rangle (4m\rho_B V_n^3 A) \quad (2.13)$$

where it is assumed that $4m\rho_m V_n^3$ does not change throughout the bed. This assumption is validated in Cody (1996), who noticed no significant change in $S_a(f, 0)$ when the bed height was changed by a factor of 50%. This equation relates the acceleration at one point on the wall to the average acoustic shot noise across the cylinder wall. The experimental mean-squared acceleration at the wall is given by

$$a^2 = a_m^2 - a_n^2 = \int_{f_1}^{f_2} S_a(f, 0) df - \int_{f_1}^{f_2} S_n(f, 0) df \quad (2.14)$$

Here, a_n is the contribution of noise independent of particle and gas movement. $S_n(f, 0)$ is measured with the bed at rest to determine noise. As stated, it is assumed that the impact time of particles at the wall is less than 0.1 ms. Indeed, it is shown extensively in Cody et al. (1996) that the dominant contribution to the wall

acceleration power spectrum occurs above 10KHz. We adopt this lower limit due to similarities between particles used, flow conditions specified, and bed geometry in both experiments. Despite differences in the wall material used, it is assumed that the power spectral densities are caused by the same physical processes. Combined with the upper limit restriction of the accelerometer used, this places our wall acceleration measurements in the 10-20 KHz range. The upper and lower bounds of the integral in equation 2.14, f_2 and f_1 , are then 20,000 Hz and 10,000 Hz, respectively. Defining an integral of the average mechanical transfer function

$$I^2 = \int_{f_1}^{f_2} \langle |H(f)|^2 \rangle df \quad (2.15)$$

and combining with Eqn. (A) relates the particle normal velocity to the acceleration at the wall:

$$V_n = \left(\frac{1}{d_p \rho_s^{1/3} \rho_B^{1/3}} \right) \left(\frac{3a^2}{2\pi I^2 A} \right)^{1/3} \quad (2.16)$$

The integral I^2 is computed over the same frequency range as the acceleration measurements. This value is constant for a structure and is a measurement of the momentum transfer through the wall. Equation 2.16 correlates the average normal particle velocity to the vibrational energy at the wall. The mean-squared acceleration defined by equation 2.14 was determined experimentally at various superficial gas velocities for the three materials. The unknown value I^2 was determined through an impulse-response analysis of the vertical tube. V_n as given by Equation 2.16 is the root mean squared velocity fluctuation, with the granular temperature given simply as the square of V_n .

2.5 Summary of Computational Methods

With the validation of computational models and the determination of key parameters being one of the goals of this project, it is worthwhile to summarily describe the process employed to model granular flows. There are two main methods used to describe these processes. The Eulerian-Lagrangian approach models the solid phase as discrete particles, with the fluid phase described using an Eulerian framework and the discrete particles, Lagrangian. Here, the fluid phase is modeled as a continuum. The momentum and energy equations of the continuum phase include terms that account for fluid-solid phase interactions. The advantage of this method lies in the ability to emulate reactions on a particle level since each particle is treated as a discrete body. Disadvantages include a heavy amount of computational effort imposed by treating each particle as a discrete entity, especially when increasing the number of particles in a model. This method is fitting for small-scale simulations, including laboratory-scale experiments, but is not suitable for larger-scale models.

In the Eulerian-Eulerian approach, the solid phase is also described as a continuum. Both phases are modeled in an Eulerian framework, as the name implies. Conservation equations are employed for both phases, as well as constitutive relations, which include equations of state. The constitutive equations concerning the solid phase are derived from the application of kinetic theory to granular flow, as implemented in the computer code by “Fluent” (2005). Parameters such as granular pressure and solid phase viscosity are determined using these equations, and are

invaluable when used in the conservation equations for the solid phase. Volume fractions for each phase are introduced and integrated into these equations. The Eulerian-Eulerian approach is best suited for large-scale models or those dealing with a large solid phase volume fraction. The computational cost is much lower as compared to the Eulerian-Lagrangian approach and is better suited to for large-scale, industrial applications. This was the method employed in the computational modeling for which the present experiment is providing data.

By treating each phase as separate continua, the governing equations may be written as follows (Didwania et al., to appear). The continuity equation for a phase k , where $k = g$ for gas or m for solids, is given by:

$$\frac{\partial}{\partial t}(\varepsilon_k \rho_k) + \frac{\partial}{\partial x_i}(\varepsilon_k \rho_k u_{ki}) = 0 \quad (2.17)$$

Momentum conservation for a phase k is given by:

$$\frac{\partial}{\partial t}(\varepsilon_k \rho_k u_{ki}) + \frac{\partial}{\partial x_j}(\varepsilon_k \rho_k u_{ki} u_{kj}) = -\varepsilon_k \frac{\partial P_g}{\partial x_i} + \frac{\partial \tau_{kij}}{\partial x_j} + I_{gmi} + \varepsilon_k \rho_k g_i + \delta_{kg} f_{gi} \quad (2.18)$$

The void fraction, density, velocity, and pressure in these equations are as defined before. f_{gi} represents body forces imparted onto the gas phase. The two terms that are added to the Navier-Stokes equations, I_{gmi} and τ_{kij} , need to be closed. I_{gmi} is the interfacial drag term, which represents interactions between the gas and solid phases. τ_{kij} represents the stress term which requires special attention. This term also appears in the granular energy transport equation for the solid phase:

$$\frac{3}{2} \varepsilon_m \rho_m \left[\frac{\partial \Theta_m}{\partial t} + u_{mj} \frac{\partial \Theta_m}{\partial x_j} \right] = \frac{\partial}{\partial x_i} \left(\kappa_m \frac{\partial \Theta_m}{\partial x_i} \right) + \tau_{mij} \frac{\partial u_{mi}}{\partial x_j} + \Pi_m - \varepsilon_m \rho_m J_m \quad (2.19)$$

This is the equation to be solved to determine the granular temperature of the solids phase. It is to this value that the experimental granular temperature will be compared.

In this equation, the solids conductivity of granular energy κ_m is given by:

$$\kappa_m = \left(\frac{\kappa_m^*}{g_0}\right) + \left[\left(1 + \frac{12}{5}\eta\varepsilon_m g_0\right) \left(1 + \frac{12}{5}\eta^2(4\eta - 3)\varepsilon_m g_0\right) + \frac{64}{25\pi}(41 - 33\eta)\eta^2(\varepsilon_m g_0)^2 \right] \quad (2.20)$$

where

$$\kappa_m^* = \frac{\varepsilon_m \rho_m \Theta_m g_0 \kappa}{\rho_m \Theta_m \varepsilon_m g_0 + \left(\frac{6\beta_{gm}\kappa}{5\varepsilon_m \rho_m}\right)} \quad (2.21)$$

and

$$\kappa = \frac{75\rho_m d_p \sqrt{\pi\Theta_m}}{48\eta(41 - 33\eta)} \quad (2.22)$$

The collisional dissipation term, J_m , is given by:

$$J_m = \frac{48}{\sqrt{\pi}}\eta(1 - \eta)\frac{\varepsilon_m g_0}{d_p}\Theta_m^{3/2} \quad (2.23)$$

where

$$\eta = \frac{1 + e}{2} \quad (2.24)$$

It is important to note the appearance of the particle-particle restitution coefficient, e , which appears in the last expression. This term appears in the collisional dissipation term as well as the solids conductivity of the granular energy, and is one of the parameters of interest in comparisons between simulation and experiment. The interphase exchange term, Π_m , is represented as:

$$\Pi_m = -3\beta_{gm}\Theta_m + \frac{81\varepsilon_m\mu_g^2|\mathbf{u}_g - \mathbf{u}_m|^2}{g_0d_p^3\rho_m\sqrt{\pi\Theta_m}} \quad (2.25)$$

The stress term in the momentum and energy equations, τ_{mij} , is given by:

$$\tau_{mij} = \left(-P_m + \eta\mu_b \frac{\partial u_{mi}}{\partial x_i}\right) \delta_{ij} + 2\mu_m S_{mij} \quad (2.26)$$

where

$$S_{mij} = \frac{1}{2} \left(\frac{\partial u_{mi}}{\partial x_j} + \frac{\partial u_{mj}}{\partial x_i} \right) - \frac{1}{3} \frac{\partial u_{mi}}{\partial x_j} \quad (2.27)$$

The solids pressure P_m is represented as:

$$P_m = \varepsilon_m \rho_m \Theta_m [1 + 4\eta\varepsilon_m g_0] \quad (2.28)$$

Note the appearance of the term η , which is proportional to the particle-particle restitution coefficient. The solids viscosity is represented as:

$$\mu_m = \left(\frac{2+\alpha}{3}\right) \left[\frac{\mu_m^*}{g_0\eta(2-\eta)} \left(1 + \frac{8}{5}\eta\varepsilon_m g_0\right) \left(1 + \frac{8}{5}\eta(3\eta-2)\varepsilon_m g_0\right) + \frac{3}{5}\eta\mu_b \right] \quad (2.29)$$

where

$$\mu_m^* = \frac{\varepsilon_m \rho_m \Theta_m g_0 \mu'}{\rho_m \Theta_m \varepsilon_m g_0 + \left(\frac{2\beta\mu'}{\varepsilon_m \rho_m}\right)} \quad (2.30)$$

$$\mu' = \frac{5}{96} \rho_m d_p \sqrt{\pi\Theta_m} \quad (2.31)$$

and

$$\mu_b = \frac{256}{5\pi} \mu' \varepsilon_m^2 g_0 \quad (2.32)$$

This model is acceptable for use in the dilute regime of particle flow (e.g. pneumatic regime), where collisional effects are dominant. One of two different models are applied, however, as the granular flow approaches the plastic regime, and frictional

stresses are created. The Schaeffer model (Schaeffer, 1987; Syamlal et al., 1993) proposes the following relations for solids pressure and viscosity:

$$P_c = \begin{cases} 10^{25}(\varepsilon_g^* - \varepsilon_g)^{10} & \text{if } \varepsilon_g < \varepsilon_g^* \\ 0 & \text{if } \varepsilon_g \geq \varepsilon_g^* \end{cases} \quad (2.33)$$

$$\mu_f = \begin{cases} \min\left(\frac{P_c \sin \phi}{\sqrt{4I_{2D}}}, \mu_m^{max}\right) & \text{if } \varepsilon_g < \varepsilon_g^* \\ 0 & \text{if } \varepsilon_g \geq \varepsilon_g^* \end{cases} \quad (2.34)$$

where $\mu_m^{max} = 1000P$,

$$I_{2D} = \frac{1}{6}[(D_{m,11} - D_{m,22})^2 + (D_{m,22} - D_{m,33})^2 + (D_{m,33} - D_{m,11})^2] + D_{m,12}^2 + D_{m,23}^2 + D_{m,31}^2 \quad (2.35)$$

and

$$D_{m,ij} = \frac{1}{2} \left(\frac{\partial u_{mi}}{\partial x_j} + \frac{\partial u_{mj}}{\partial x_i} \right) \quad (2.36)$$

In this model it is assumed that the critical void fraction ε_g^* , below which particle interaction is purely frictional, is equal to ε_{mf} . Another approach by Srivastava and Sundaresan (2003) modifies the Schaeffer model by accounting for strain rate fluctuations. This so-called Princeton model of frictional stress affects flow behavior for instances in which the void fraction of the particle assembly is less than the critical void fraction (below maximum packing). The solids pressure is given as:

$$\frac{P_f}{P_c} = \left(1 - \frac{\nabla \cdot u_m}{n\sqrt{2} \sin \phi \sqrt{\mathbf{S} : \mathbf{S} + \Theta_m/d_p^2}} \right)^{n-1} \quad (2.37)$$

Here,

$$P_c = \begin{cases} 10^{25}(\varepsilon_g^* - \varepsilon_g)^{10} & \varepsilon_g < \varepsilon_g^* \\ Fr \frac{((1 - \varepsilon_g) - \varepsilon_{sf}^{min})^r}{(\varepsilon_g - \varepsilon_g^*)^s} & \varepsilon_g^* \leq \varepsilon_g \leq (1 - \varepsilon_{sf}^{min}) \\ 0 & \varepsilon_g \geq (1 - \varepsilon_{sf}^{min}) \end{cases} \quad (2.38)$$

where $r = 2$, $s = 5$, and the Froude number $Fr = 0.05$. The solids viscosity is represented as:

$$\mu_f = \frac{\sqrt{2}P_f \sin \phi}{\sqrt{\mathbf{S}:\mathbf{S} + \Theta_m/d_p^2}} \left\{ n - (n - 1) \left(\frac{P_f}{P_c} \right)^{\frac{1}{n-1}} \right\} \quad (2.39)$$

The coefficient n is set differently depending on whether the granular material experiences dilation or compaction:

$$n = \begin{cases} \frac{\sqrt{3}}{2 \sin \phi} & \nabla \cdot \mathbf{u}_m \geq 0 \\ 1.03 & \nabla \cdot \mathbf{u}_m < 0 \end{cases} \quad (2.40)$$

In addition to the different stress models employed in the simulations, one of two boundary conditions at the wall is employed. The first is a simple free-slip condition, in which it is assumed that there is no tangential force exerted onto the confining wall by the solid phase. The second condition, proposed by Johnson and Jackson (1987), accounts for partial slip at the wall. In this model, the tangential force per unit area of the wall is equated to the stress within the particle assembly in the region near the wall. The tangential solids velocity at the wall is related by:

$$\mu_m \frac{\partial u_m}{\partial x} = - \frac{\phi_p \pi \rho_m \varepsilon_m g_0 \sqrt{\Theta_m}}{2\sqrt{3}\varepsilon_m^{max}} u_m \quad (2.41)$$

where ϕ_p is the friction angle. The granular energy at the wall is given by:

$$\kappa_m \frac{\partial \Theta_m}{\partial x} = \frac{\phi_p \pi \rho_m \varepsilon_m g_0 \sqrt{\Theta_m}}{2\sqrt{3}\varepsilon_m^{max}} u_m^2 - \frac{\sqrt{3}\pi \rho_m \varepsilon_m g_0 (1 - e_w^2) \sqrt{\Theta_m}}{4\varepsilon_m^{max}} \Theta_m \quad (2.42)$$

Notable in this equation is the appearance of the particle-wall restitution coefficient, e_w .

To summarize, there are four parameters which were varied in the computational modeling of this system. The most important item is the type of frictional stress model (Schaeffer or Princeton) used for situations in which the solids volume fraction is high, or when the void fraction of the system is near that of its value at minimum fluidization. Next, one of two boundary conditions is employed at the wall: free-slip or Johnson & Jackson's condition of partial slip of the solid phase. Within the Johnson & Jackson model appears the third parameter, the particle-wall restitution coefficient e_w . The final parameter is the particle-particle restitution coefficient, e , which appears in the solids conductivity term, the collisional dissipation term, and the solids pressure term used for dilute particle assemblies. Comparisons between experimental results of the mean bed expansion ratio and granular temperature will be compared to those obtained through simulation stemming from the preceding theory.

3. Experimental Investigations

3.1 Bed Material Characterization and Determination of Particle Dimensions

As mentioned, the particles used in the experiment all fall within the Geldart B range. The first particle type consists of soda-lime glass spheres, while the other two materials are ceramic particles of a sand-like consistency. The compositions of the EconoProp and CarboHSP materials are displayed in Table 3.1.

Table 3.1: Composition, by percentage, of each bed material used in this experiment

EconoProp 40/70		CarboHSP 30/60	
Compound	Composition [weight %]	Compound	Composition [weight %]
Al ₂ O ₃	48.0	Al ₂ O ₃	83.0
SiO ₂	48.0	SiO ₂	5.0
TiO ₂	2.0	TiO ₂	3.5
Fe ₂ O ₃	1.0	Fe ₂ O ₃	7.0
Other	1.0	Other	1.5

The combination of particle density and mean diameter size of each material results in a bubbling situation at the onset of fluidization. The determination of mean diameter size was determined prior to fluidization. The respective positions of each material on the Geldart diagram are shown in Figure 3.2 to provide confirmation of their Geldart classification.

The average particle diameter for each of the three materials was determined using an Olympus GX 51 optical microscope. Shadowed areas of the sampled particles were recorded, along with the perimeter and the largest diameter length scale. For the Glass Spheres, the circular diameter was recorded due to the fact that each

particle has a perfectly spherical shape. Diameter distributions were compared to mesh size distributions published by the manufacturer.

Digital images were captured using the Paxcam 3 camera and were analyzed using the Pax-It! v.6 software. The total magnification used was 50x. 470 glass beads were analyzed, along with 613 particles of the EconoProp and 902 particles of the CarboHSP material. More samples were obtained for the larger particle sizes due to higher diameter variability of the larger materials. Digital images of each particle type are shown in Figure 3.1:

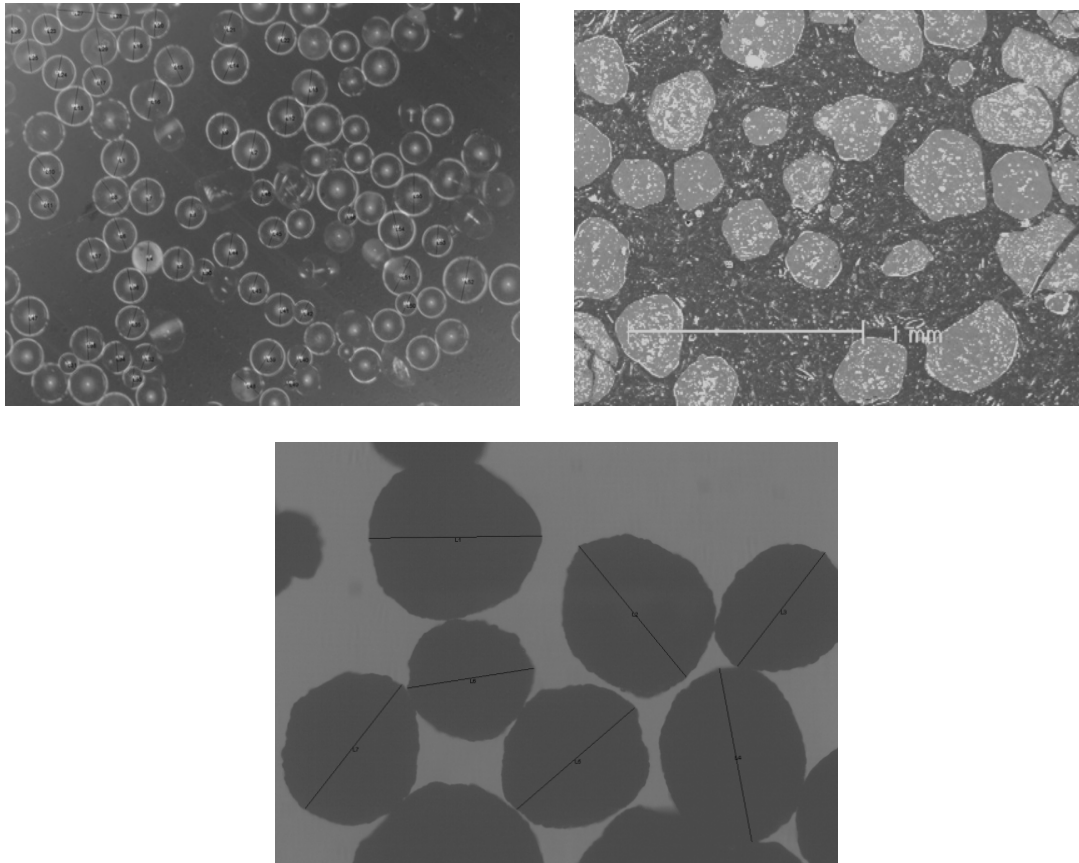


**Figure 3.1: Zoomed images of the three bed materials used in this experiment.
Clockwise, from top left: Glass Spheres, EconoProp, and CarboHSP**

The spherical shape of the glass beads is apparent, along with the near-circular shape of the larger material. The lines, which were drawn using a click-and-drag mouse mechanism, were recorded for all of the samples. Using objective and lens focus values, the Pax-It! software was able to determine the length of the lines. These particle diameter values were exported into a Microsoft Excel spreadsheet, where the appropriate statistical analysis was performed. A normal distribution of particle diameters was assumed, following the work of Kravanja (2008).

The mean particle diameters for each material, along with the standard deviation, are compared with the published values in Table 3.2.

Table 3.2: Comparison between published and experimentally-determined mean particle diameters for each of the three materials tested

Material	Published mean diameter [μm]	Experimental mean diameter	Standard Deviation σD_p [μm]	Published roundness
Glass Spheres	123.0	122.8	17.5	1.0
Carbo EconoProp	334.0	350.1	54.5	0.9
Carbo HSP	430.0	440.0	62.6	0.9

Due to the small standard deviation of the Glass Spheres particle diameter distribution, this bed material was assumed to be monodisperse. The significantly larger standard deviations of the EconoProp and CarboHSP particle diameter distributions suggest they be classified as polydisperse. The Geldart chart, marked with the density-diameter cross of each material based on the experimentally-determined mean diameter, is shown in Figure 3.2:

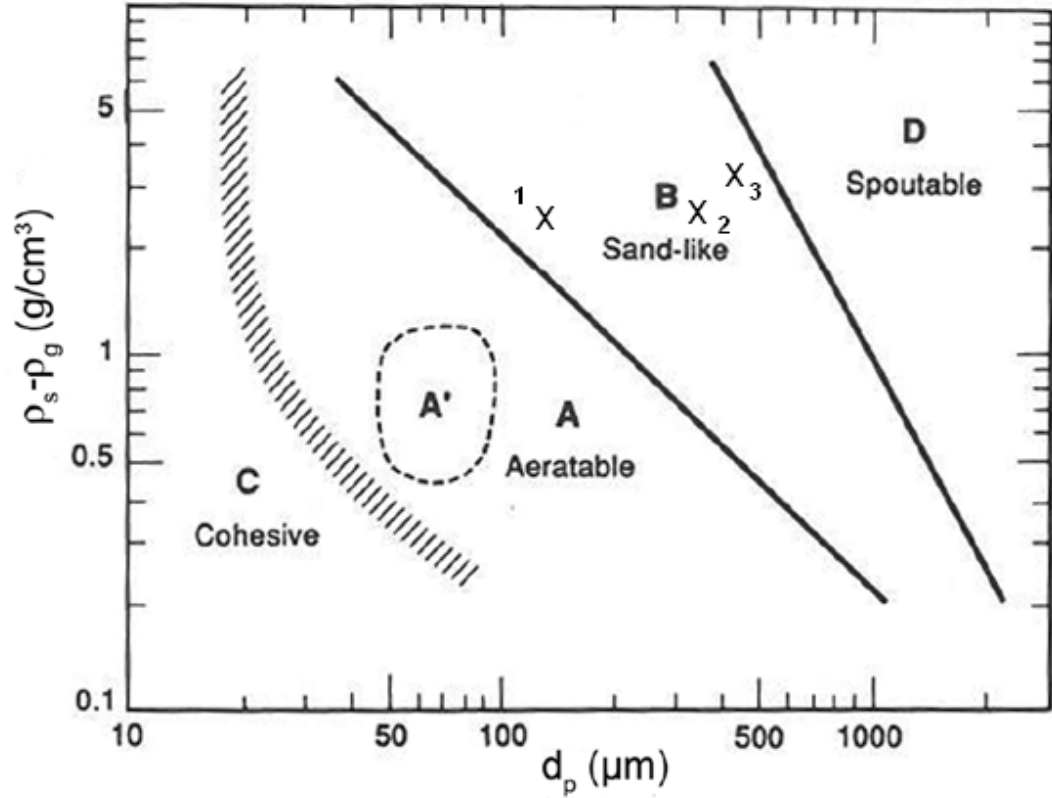


Figure 3.2: Geldart diagram overlaid with markings showing where each bed material used in this experiment falls. 1: 123 μm Glass Spheres (density 2520 kg/m^3); 2: 334 μm ceramic EconoProp particles density 2700 kg/m^3 ; 3: 430 μm ceramic CarboHSP particles density 3560 kg/m^3)

As mentioned, each of the particle types falls comfortably within the Geldart B range. To estimate the mean particle mass and surface area, a normal distribution was assumed for the diameters of each particle type. The probability density function (PDF) for the normal distribution of diameter is defined as follows:

$$f(x) = \frac{1}{\sigma\sqrt{2\pi}} \exp\left(\frac{-(x - \mu)^2}{2\sigma^2}\right) \quad (3.1)$$

$$\int_{-\infty}^{+\infty} f(x)dx = 1.0 \quad (3.2)$$

where 'x' is the diameter. The formulas for surface area and volume of a sphere, respectively, are:

$$S(x) = \pi x^2 \quad (3.3)$$

$$V(x) = \frac{\pi x^3}{6} \quad (3.4)$$

So, the formula to be solved for the average surface area is:

$$\overline{SA} = \frac{\int_a^b S(x)f(x)dx}{\int_a^b f(x)dx} = \frac{\int_a^b \frac{\pi x^2}{\sigma\sqrt{2\pi}} \exp\left(\frac{-(x-\mu)^2}{2\sigma^2}\right) dx}{\int_a^b \frac{1}{\sigma\sqrt{2\pi}} \exp\left(\frac{-(x-\mu)^2}{2\sigma^2}\right) dx} \quad (3.5)$$

The formula to determine the average mass of a particle is:

$$\bar{m} = \rho \int_a^b V(x)f(x)dx = \rho \int_a^b \frac{\pi x^3}{6\sigma\sqrt{2\pi}} \exp\left(\frac{-(x-\mu)^2}{2\sigma^2}\right) dx \quad (3.6)$$

Using a MATLAB code which performs the 1/3 Simpson method of numerical integration with 256 increments, the values were determined and the results have been tabulated in Table 3.3:

Table 3.3: Experimentally-determined values of mean surface area and particle mass for all three materials tested

	Glass Spheres	EconoProp	CarboHSP
Mean Surface Area [μm^2]	1.94×10^5	1.62×10^6	2.48×10^6
Mean Particle Mass [g]	2.55×10^{-6}	6.22×10^{-5}	1.14×10^{-4}

3.2 Experimental Setup

A CAD drawing of the experimental structure is shown in Figure 3.3. The basic components include the polycarbonate fluidized bed tube, the aluminum reservoir underneath through which the fluidizing gas enters the system, and the porous distributor plate connecting the two. The dimensions of the mock reactor are 1.22 m (4.00 ft) in length, with inner and outer diameters of the tube being 8.26 cm

(3.25 in) and 8.89 cm (3.50 in), respectively. Markings were etched onto the vertical axis of the tube in intervals of 1.0 cm (0.4 in) to determine bed height. Visible in Figure 3.3 are the locations of the five pressure taps running alongside the tube, along with a sixth pressure tap under the distributor plate. The bottom pressure measurement was used to calculate the pressure drop over the porous plate at various gas velocities for the purpose of validating the distributor plate design. Proper design of this component was necessary to ensure smooth and uniform fluidization inside the bed. Theoretical design considerations and actual dimensions of the plate are discussed shortly.

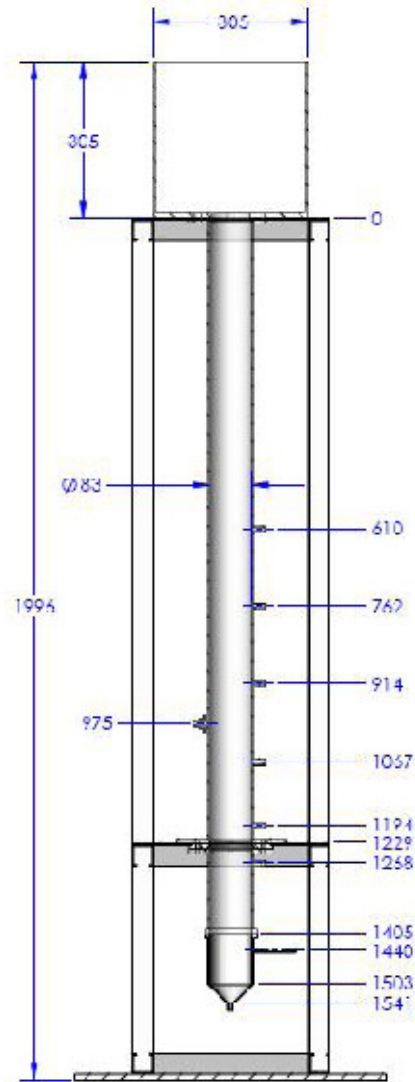


Figure 3.3: Cad drawing of the fluidized bed, including outer support

The pressure taps running along the vertical axis of the tube served to record pressure fluctuations throughout the bed during fluidization. Pressure taps above the distributor plate fit through 1.27 cm (0.50 in) diameter holes bored directly into the side of the polycarbonate tube. Below the porous plate, the bottom pressure tap fits into the aluminum reservoir via a threaded insert. The numbering of the pressure taps

begins at the top and increases downward. The top-most pressure tap is denoted P1, and the probe located below the distributor plate is P6. A schematic of the pressure tap system used for P1-P5 is shown in Figure 3.4.

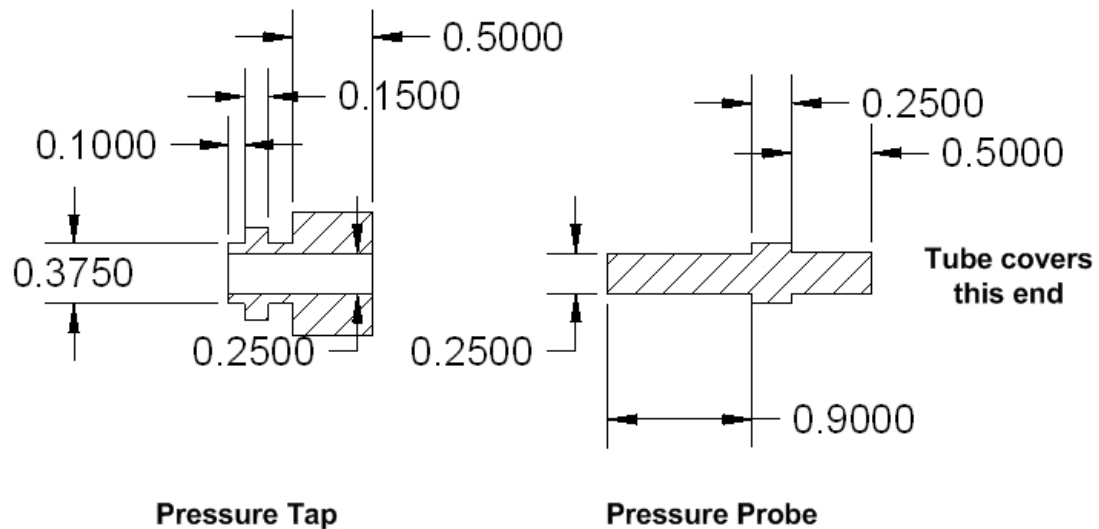


Figure 3.4: Schematic of pressure tap system. Dimensions given in inches

The pressure probe was inserted into the pressure tap, the end of which rests flush with the inner surface of the polycarbonate bed wall. Tubing, which fits snugly over the opposite end of the pressure probe, runs to the corresponding pressure transducer.

The hollow tap shown in Figure 3.4 was inserted into the bored holes along the cylinder wall. General purpose RTV 108 was used to secure the taps onto the wall. Since the tangential and normal forces incident on the taps in the direction of the tube wall were very small, and since the torque caused by the weight of the attached tubing was negligible, this method was used for simplicity of installation. A mesh screen was

attached to the tip of the pressure probe to prevent particle flow into the pressure line. As a further precaution, a small amount of fine steel wool was inserted into the stainless steel tubing to further block any particles from entering into the line, including the pressure transducers to which the taps are connected. Another advantage of using RTV to connect the pressure tap to the wall was the ease of replacement of the mesh screens, and periodic cleaning of the tap, probe, and line to the transducer.

The accelerometer was attached to the side of the cylinder wall via an acrylic fixture, with dimensions shown in Figure 3.5. The fixture was attached to the tube using an epoxy resin adhesive. Special care was taken to ensure proper attachment, making sure that the piece was fastened on straight and with as little interstitial space as possible. This was necessary to reduce error related to non-normal orientation of the accelerometer and to ensure proper energy transfer from tube to accelerometer. The fixture was mounted such that the bottom end lay 25.4cm (10.0 in) above the distributor plate.

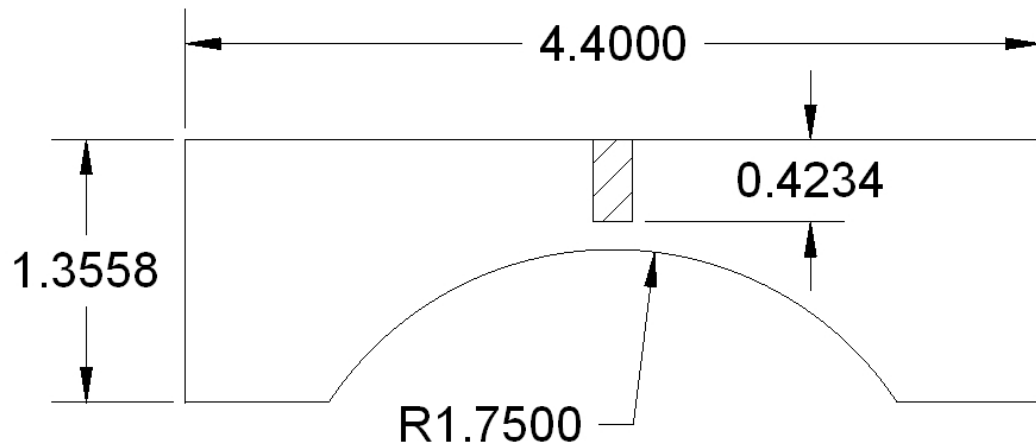


Figure 3.5: CAD drawing of acrylic fixture used to attach the accelerometer to the bed of the wall. The hatched portion denoted a tapped hole. Dimensions are given in inches

The model used was an ACC-310 Omega accelerometer, powered and amplified by an Omega ACC-PS2 power supply and signal amplifier. The accelerometer signal traversed the same path as the pressure signals. A schematic of the acquisition of the acceleration is shown in Appendix A.

The vertical tube was supported by a rigid structure consisting of 4.128 cm x 4.128 cm (1.625 in x 1.625 in), three-sided, hollowed steel strut bar. Necessary components including wiring board, signal conditioning circuit boards, rotameters, and power supplies were connected to the steel structure via aluminum mounting panels.

A schematic of the entire experimental setup is shown in Figure 3.6.

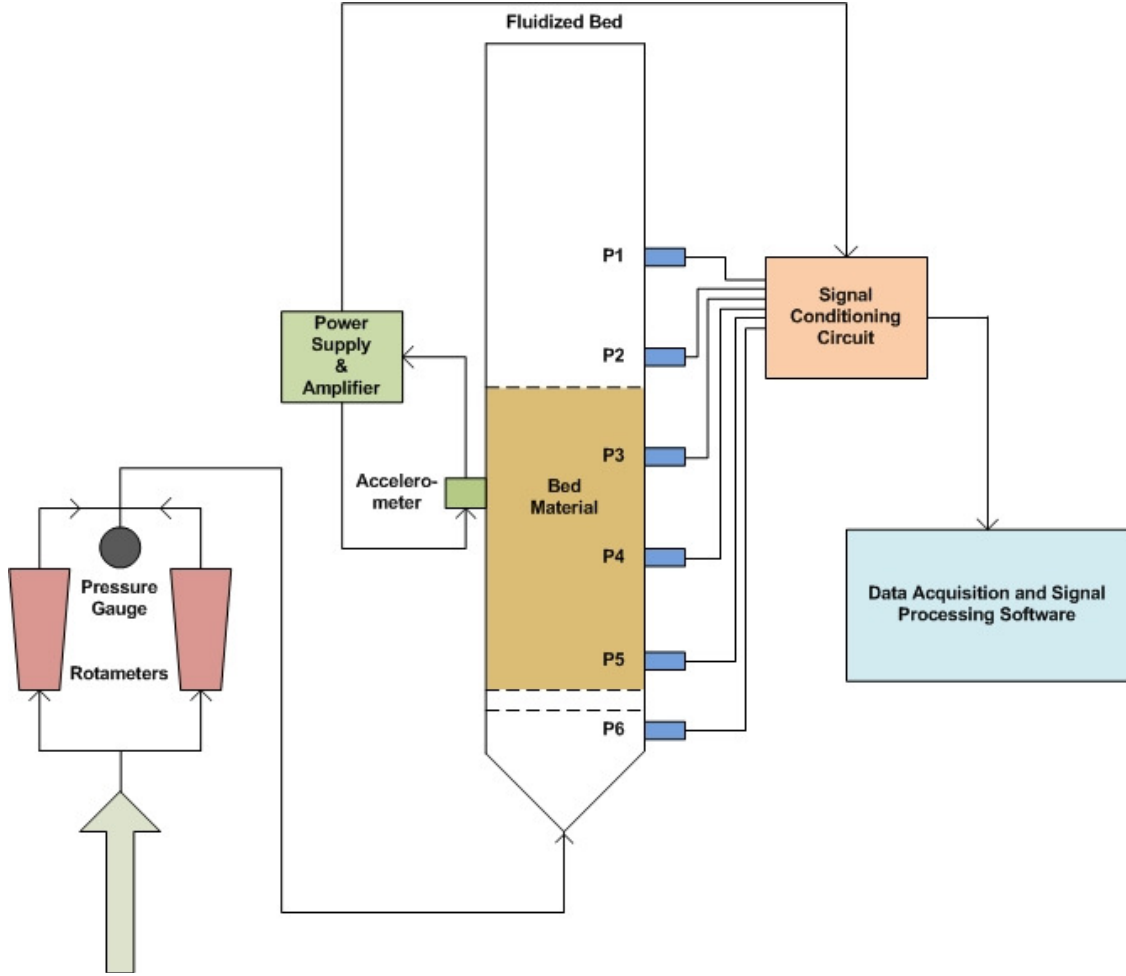


Figure 3.6: Schematic of the experimental setup

Atmospheric air is introduced through a pressure regulator and flows through two Omega FL-3440C rotameters. Each rotameter has a flow range of 0 – 66.3 liters/min at standard atmospheric pressure and feeds directly into the aluminum reservoir located directly underneath the porous distributor plate. A flow correction factor was employed, taking into account the non-atmospheric pressure of the air flowing through each rotameter. The actual flow rate through each rotameter, Q_s , is expressed as a function of the equivalent flow at standard atmospheric pressure, Q_a ,

and the ratio of atmospheric pressure p_o to the pressure of air after flowing through the rotameters, p_g :

$$Q_s = Q_a \sqrt{\frac{p_o}{p_g}} \quad (3.7)$$

Corrections due to temperature were ignored due to the negligible difference between the temperature for the calibrated flow rates, 21.0°C (69.8°F) and the actual operating temperature, which remained nearly constant at about 20.0°C (68.0°F). A 0.9525 cm (3/8 in) four-way union connected the two flows from the rotameter to the tube leading to the reservoir. The fourth connection led to a digital pressure gauge, used for determining the flow pressure p_g as well as calibrating the pressure transducers. The Omega DPG1000AD-100G pressure gauge has a range of 0-100 psig and is accurate to 0.1 psi.

The pressure taps P1-P6 were connected via 0.635 cm (0.25 in) clear plastic tubing to Omega PX26-005GV (5 psig-maximum) and PX-015GV (15 psig-maximum) gage pressure transducers. The reservoir probe was connected to the 15 psig-maximum transducer due to the higher pressure in this region below the porous plate. The upper five bed transducers had a maximum rating of 5 psig. The transducers were connected to a signal conditioning circuit board which amplified the signals from the transducers to a 0-10V output. A schematic of the circuit board is shown in Appendix A. The output signal were connected to a National Instruments (NI) SCB-68 shielded I/O connector block and sent to a NI PCI-MIO-16E-4 data acquisition (DAQ) board. From here, the captured 0-10V signals were recorded and

processed using NI LabVIEW v6.1 software. The pressure acquisition virtual instrument (VI) program is displayed in Appendix A.

3.3 Note on Pressure Probe Design and Maintenance

It is important to keep in mind the effects of clogging and pressure dampening when designing and maintaining pressure for this application. As mentioned, a small portion of wire mesh was attached to the end of each pressure probe. When considering mesh size for this application, it is important to find a compromise between larger mesh sizes, which cannot contain particles of certain diameters, and finer meshes, which may become clogged more readily.

Eventually, the mesh used to keep particles out of the pressure probe line will inevitably become clogged, at least to some degree, by fine particles. As such, it is necessary to periodically clean out the pressure lines and protective meshes. In the present experiment, noticeable differences in the pressure levels and fluctuations occurred after 10 – 15 minutes of runtime for the Glass Spheres. The same occurred for the larger materials, though at later stages (typically ~ 30 min).

Also worthy of mention is the steel wool which was used as a secondary line of defense against penetrating particles. After a simple comparison between pressure probes with and without any steel wool, there was no noticeable dampening effect caused by the addition of steel wool. This design consideration was therefore an excellent choice in preventing stray particles from reaching the pressure transducers after coming through the initial mesh shield.

Each pressure probe was connected to its respective pressure transducer through 0.635 cm (0.25 in) inner diameter tubing, as noted. The length of each tube was set at 45.7 cm (18.0 in) so as to prevent any discrepancy caused by differences in this dimension. This is in agreement with Van Ommen et al. (1999) who found, after testing several probe-transducer setups, that the connecting tube should be no longer than 2.5 m (98.4 in). Indeed, it follows from intuition that, for any dynamic measurement of pressure, a shorter connecting tube yields more accurate measurements.

3.4 Distributor Plate Design

Proper design of the gas distributor is necessary to ensure uniform flow and smooth fluidization of the bed material. Relevant factors include, but are not limited to, the size of pore holes, the geometric distribution of the holes, the spacing in between each pore, and the ratio of open flow area to total plate area. In terms of measurable quantities, the pressure drop across the distributor gives the greatest indication of proper distributor plate function. One must strike a compromise between having a large enough pressure drop to ensure proper fluidization and keeping the energy input to a reasonable level. Another consideration is having a high enough flow rate through each pore to prevent penetration of the bed material into the reservoir.

To compensate for various particle diameters and densities, three separate plates were designed. The simple design employed consists of a thin, circular aluminum plate with drilled holes through which the air may pass. The diameter of

the plate was 8.89 cm (3.50 in) with a thickness of 1.00 mm (0.04 in). Kunii (1991) described an experimentally-verified design process for a gas distributor which is utilized here.

To begin, as a rule of thumb, the pressure drop across the distributor Δp_d is generally 20-40% of the pressure drop across the bed:

$$\Delta p_d / \Delta p_b = (0.2 - 0.4) \quad (3.8)$$

Δp_d is defined as $P_1 - P_2$, and Δp_b as $P_2 - P_6$. The calculated pressure drops of each bed material ranged from 11.0 to 15.5 Pa (1.60 to 2.25 psi). Δp_d for each distributor plate was designed to be 3800 Pa (0.55 psi), corresponding to a $\Delta p_d / \Delta p_b$ ratio range of 0.25 to 0.35.

The next step in design is the estimation of the orifice coefficients, $C_{d,or}$. Table 3.4 displays a correlation between the orifice coefficient and the Reynolds number Re_t of the flow, taken from Kunii (1991).

Table 3.4: Correlation between fluidization chamber Reynolds number and coefficient through the orifice. Kunii (1991)

Re_t	100	300	500	1000	2000	>3000
C_{d,or}	0.68	0.70	0.68	0.64	0.61	0.60

The flow Reynolds number is given as:

$$Re_t = \frac{d_t U_s \rho_g}{\mu} \quad (3.9)$$

Here, d_t is the inner diameter of the tube approaching the distributor plate. U_s is the superficial gas velocity, as previously described. ρ_g and μ are the respective density and dynamic viscosity of standard atmospheric air.

With the proper orifice coefficient chosen, the gas velocity through the orifice is determined using Bernoulli's equation, modified for lost energy:

$$U_{or} = C_{d,or} \sqrt{\frac{2\Delta p_d}{\rho_g}} \quad (3.10)$$

Through conservation of mass, the ratio of gas velocities U_s/U_{or} is equal to the fraction of open orifice area of the distributor plate, k . In terms of total plate area and total open orifice area, A_o , this relation is expressed as:

$$k = \frac{U_s}{U_{or}} = \frac{A_o}{A_f} \quad (3.11)$$

The superficial gas velocity used in each case was twice the minimum fluidization velocity, $2U_{mf}$. It is with this information that the number, size and shape of the orifices were calculated. Circular holes were chosen because they tend to yield uniform and reliable flow, and are the easiest to manufacture. In terms of orifice size, one must compromise between diameters which are large enough to prevent clogging by bed particles, but are small enough to maintain an even distribution of gas. Following Hofbauer (n.d.), orifice diameters d_{or} are generally chosen to be 3 – 10 times the mean particle diameter d_p . A drill bit with a diameter of 1.320 mm (0.052 in) was chosen because the d_{or}/d_p values corresponding to this size range from 3.28 for the largest particle size to 10.73 for the smallest beads. The corresponding orifice area is given by the simple relation

$$A_{or} = \frac{\pi d_{or}^2}{4} \quad (3.12)$$

and through which the number of required orifices can be determined:

$$N_{or} = \frac{A_o}{A_{or}} \quad (3.13)$$

Table 3.5 displays the values determined for the three material types tested.

Table 3.5: Calculated pressure drops and corresponding number of orifices determined for each bed material type

Material	Δp_b [Pa]	N_{or}
Glass Spheres	10980	7
EconoProp	12764	19
CarboHSP	15511	34

The number of orifices was the variable quantity in the design of each distributor plate. Dimensioned CAD drawings of each of the three plates designed are shown in Figures 3.7-3.9:

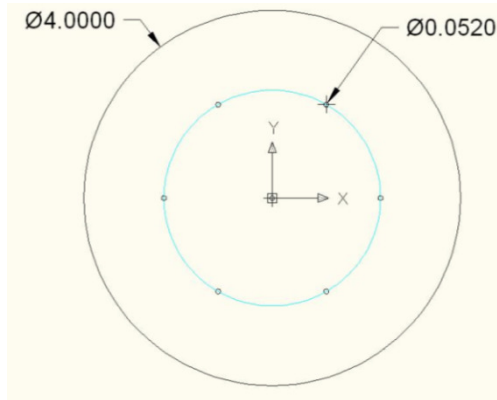


Figure 3.7: CAD drawing of distributor plate used for Glass Spheres. $N_{or} = 7$. Dimensions in inches

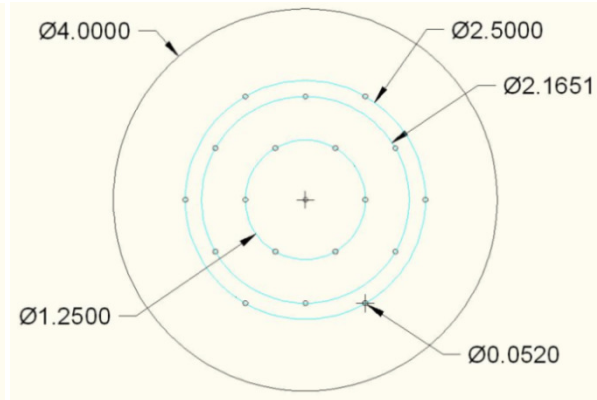


Figure 3.8: CAD drawing of distributor plate used for EconoProp. $N_{or} = 19$. Dimensions in inches

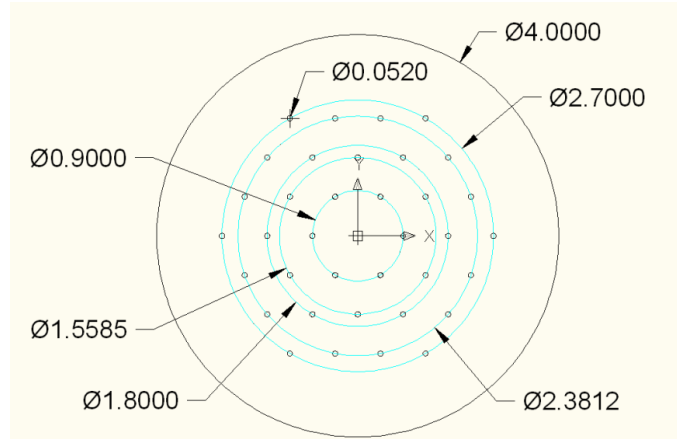


Figure 3.9: CAD drawing of distributor plate used for CarboHSP. $N_{or} = 34$. Dimensions in inches

3.5 Pressure Drop and Minimum Fluidization Measurements

Pressure transducers were calibrated using the Omega digital pressure gauge. Pressure readings were taken in intervals of 0.5 psi, and the output voltage plotted against pressure to obtain scale and offset values for each transducer. The pressure calibration curve for the P1 transducer is shown in Figure 3.10. The relationship between pressure and voltage is highly linear, as expected. Calibration curves for the other pressure transducers are not included due to the similarity between these curves and the triviality of this process.

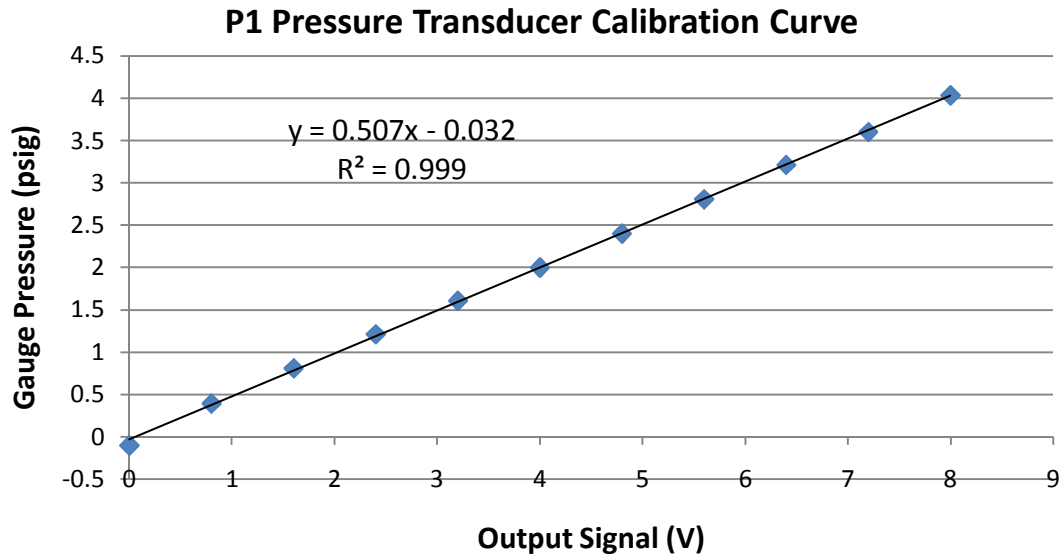


Figure 3.10: Calibration curve of the P1 pressure transducer

Prior to fluidization, the system was checked for leaks using Snoop leak detector on all of the fittings. Bed material was loaded into the vertical tube such that the fixed bed height lay between the P3 and P2 pressure probes. The CarboHSP material, however, was loaded below the P3 pressure tap due to the high gas velocities required for fluidization. The packed bed height was recorded, and was seen to vary between materials due to obvious density differences. All pressure transducers were sampled at a rate of 120 Hz. This is somewhat arbitrary; in the frequency spectrum the region of interest deals with pressure fluctuations up to about 10 Hz. It was also observed that major pressure fluctuations occurring from bubble release in the bed are on the order of ~ 0.05 s. The chosen sampling rate was capable of recording all of the pertinent behavior. When computing the pressure drop at a given superficial gas velocity, the time signals were measured for 20 seconds and averaged using

LabVIEW. This time interval was chosen such that the error margins for all measurements in this way are within $\pm 1\%$.

Pressure drop over the bed was computed for several values of U_s/U_{mf} for each material. As shown in Figure 1.3, determining the minimum fluidization velocity as a function of pressure drop was a matter of finding the superficial gas velocity at which the two linear regions intersect.

To test for repeatability, each recording was carried out on two separate occasions, with the results being averaged to determine the experimental minimum fluidization velocity. Once determined, U_{mf} was compared to the values predicted by equation 1.8 to verify the proper design and function of the fluidized bed being tested.

3.6 Bed Height and Mean Expansion Ratio Measurements

The packed bed height of each material was recorded after the particles were loaded into the tube. Bed height data were then recorded for various U_s/U_{mf} values for each of the three materials tested. From a superficial gas velocity of zero up to the minimum fluidization velocity, the upper surface of the bed was well-defined and non-fluctuating. Bed height measurements were simple to record in this region, and the bed height at minimum fluidization h_{mf} was recorded. After minimum fluidization, bubbling and slugging resulted in a fluctuating bed height. However, the upper surface of the bed remained well-defined for all flow regimes under study, and for each material type tested.

To determine the mean bed height at a specific fluidization velocity, the maximum bed height was measured ten consecutive times and then averaged to find \bar{h}_{max} , the mean maximum bed height. The same was done to find the mean minimum bed height, \bar{h}_{min} , and the process was repeated at several gas velocities for the three materials. The mean bed height was then determined as a function of superficial gas velocity by averaging the mean minimum and maximum bed heights. Using equations 1.4 & 1.5, the mean bed expansion ratios and relative fluctuation heights were defined and plotted against the normalized gas velocity, U_s/U_{mf} .

Plots of mean bed height also yield another estimate for the minimum fluidization velocity. Obtaining this value was a simple matter of realizing that the mean bed height remains constant until minimum fluidization. In terms of the mean bed expansion ratio, $\bar{\delta}$ is negative before fluidization and assumes a positive value after $U_s=U_{mf}$.

3.7 Determination of Average Transfer Function of the Fluidized Bed Wall

The frequency response of the cylinder resulting from an impulse excitation was determined with the bed at rest. A transfer function $H(f, R_i)$ was computed at each of 8 circumferential points at 14 equally-spaced vertical locations. The top vertical location was chosen such that the average of the mean maximum bed heights \bar{h}_{max} of each material under a flow of $U_s=2U_{mf}$ would reach no further than this height. Each location represents an element of the cylinder ΔA , so that $N \Delta A=A$, where N is the number of locations hit (in this experiment $8 \times 14=112$). A is the surface area of the cylinder wall that is contacted by particles during fluidization. As a

visualization, one can imagine a 14x8 rectangular grid, with each element having area ΔA . The long dimension is equal to the bed height at minimum fluidization and the short being the circumference of the vertical tube. Wrapping the grid around the vertical tube would then yield the locations of each spot tested, given as the middle point of each element.

Each point was tapped with an impulse hammer in a direction normal to the surface 10 times to improve accuracy in computing the averaged squared transfer function over the entire fluid bed/wall interface, $\langle |H(f)|^2 \rangle$. Care was taken to perform a so-called “clean hit,” in which the hammer comes into contact with the cylinder wall only once. Poor “drum roll” impacts produce inaccurate transfer functions.

Signals were captured using a trigger response system in LabVIEW. The data acquisition system began recording data at a specified force value of the impulse hammer (i.e. a “hit”). Amplifier gains of 100 were used for both the accelerometer and the hammer signal as this value yielded the highest signal-to-noise ratio. After the trigger, the time signals of the impulse hammer and the wall-mounted accelerometer were recorded for 100ms, through which the frequency-dependent transfer function was determined. Following the Nyquist theorem, each signal was sampled at 40 kHz so that the desired frequency range of the transfer function, 10-20 kHz, could be determined. A filtering operation was performed in LabVIEW to produce a clearly-defined transfer function. This procedure highlighted the resonant frequencies, and gave a better picture of the average value over the frequency range of interest. A schematic of the VI program used for this operation is given in Appendix A.

This entire process was repeated with the bed full of the three materials used, as well as with an empty cylinder.

3.8 Acoustic Shot Noise Measurement

The particle normal velocity V_n was determined by capturing the time signal of the wall-mounted accelerometer. Figure 3.11 displays the accelerometer attached to the bed wall by its acrylic fixture.



Figure 3.11: Accelerometer attachment to the fluidized bed wall. The bed is shown filled with the Glass Spheres material

The accelerometer was placed 25.4 cm (10.0 in) above the distributor plate. Measurements were taken under various fluidization conditions during intervals of ten seconds. Each of these measurements were acquired three times and averaged. As when determining the cylinder transfer function, samples were recorded at 40 kHz, such that the acceleration power spectrum from 0-20 kHz could be determined.

Likewise, an amplifier gain of 100 was applied to the accelerometer signal to ensure a high signal-to-noise ratio.

The wall acceleration time signal was converted to its power spectrum using LabVIEW. A schematic of the VI program used for this operation is shown in Appendix A. An averaged power spectral density was found by applying RMS averaging to the signal, in which the 10 second time signal was divided up into 20 samples of 0.5 seconds each.

This procedure was applied to each acquired data set. The power spectral density of the acceleration signal was integrated from 10-20 kHz as per equation 2.14, resulting in the total mean-squared acceleration a_m^2 at each fluidization velocity. Subsequent measurement with the bed at rest was integrated in the same manner to determine the mean-squared acceleration resulting from any background noise, a_n^2 . This value was determined for three separate runs, with the average being defined as the background acceleration value. To find the experimental mean-squared acceleration a^2 at each gas velocity tested, the averaged a_n^2 was subtracted from each value of a_m^2 . Application of equation 2.16 yielded the corresponding plots of granular temperature as a function of normalized superficial gas velocity.

4. Results

4.1 Pressure Drop, Void Fraction and Minimum Fluidization Velocity

The plots of bed pressure drop versus minimum fluidization velocity for each material exhibited two linear regions, as expected. Figures 4.1-4.3 display the pressure drop plots for each of the three materials tested.

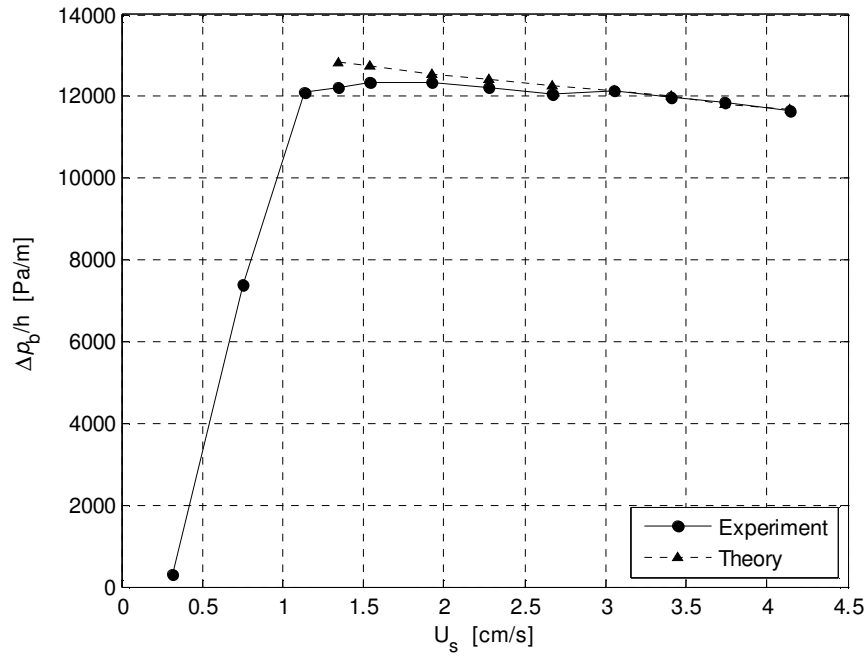


Figure 4.1: Pressure drop over mean bed height plotted against superficial gas velocity for the Glass Spheres material

The predicted pressure drop after fluidization, expressed by equation 1.1, is also plotted alongside the experimental data. Experimental values of pressure drop over average bed height are within 8% of theory, with the accuracy increasing as the gas velocity is increased. In accordance with Geldart B behavior, all of the materials exhibited bubbling at the onset of fluidization.

At the point of minimum fluidization, especially for the glass beads, bubbles were observed at the upper surface of the bed, much as in a boiling pot of water. With increasing gas velocities, bubbles began to appear alongside the wall of the bed, increasing in size until the bubble diameters approached that of the tube at a gas velocity around $3U_{mf}$. This marked the beginning of the slugging regime for this material.

Also worth noting is the slowly decreasing ratio of pressure drop to average bed height after the point of minimum fluidization. Over this range of fluidization the pressure drop remains a nearly constant value after the point of minimum fluidization. The mean bed height, however, continues to increase and so the slight decrease in $\Delta p_b/\bar{h}$ is visible in each of the graphs, as expected.

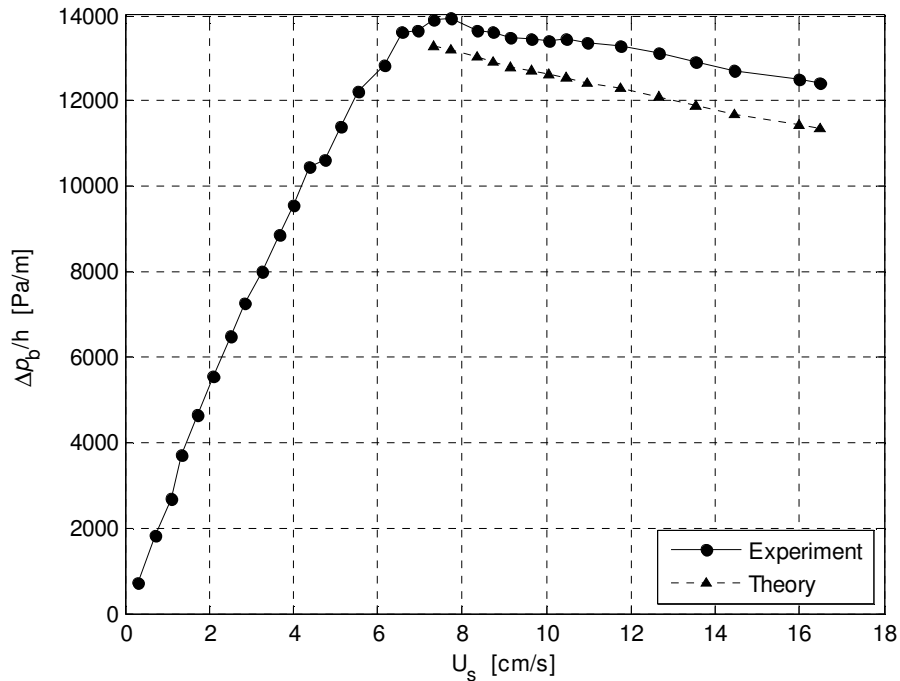


Figure 4.2: Pressure drop over mean bed height plotted against superficial gas velocity for the EconoProp material

Experimental values of pressure drop were within 10% of those predicted for the EconoProp bed material. The bubbling regime for this material was smaller, from minimum fluidization to a gas velocity of $2.5 U_{mf}$. Slugging occurred beyond this point, noticeable by the periodic lifting and falling of entire portions of the bed.

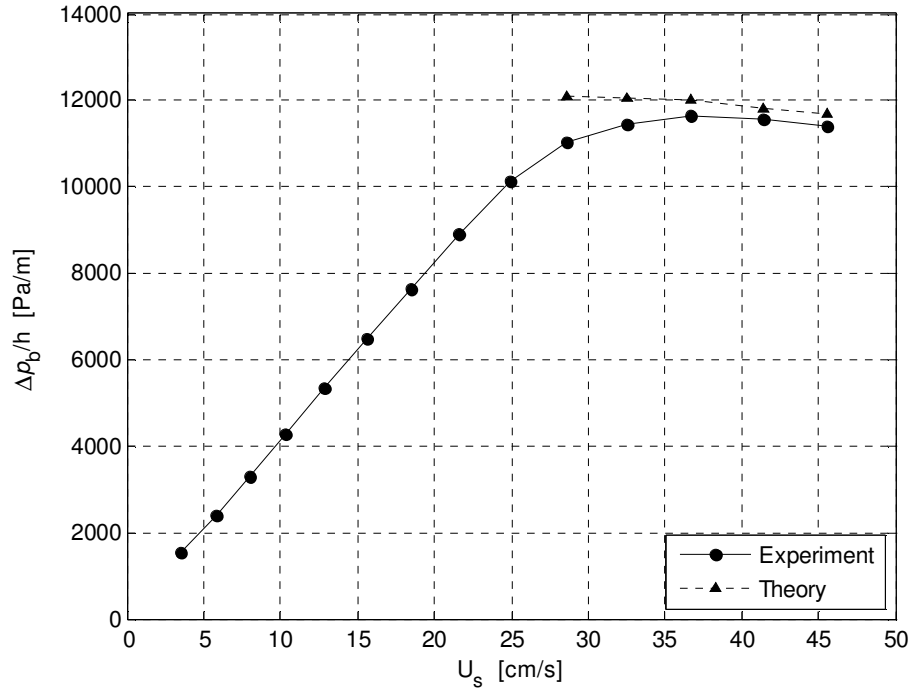


Figure 4.3: Pressure drop over mean bed height plotted against superficial gas velocity for the Carbo material

Pressure drop behavior for the CarboHSP material was similar to the other materials, with the noted exception of a smoother transition to fluidization. This may be attributed to the higher amount of interstitial space between particles of this size, as well as the greater variability in diameter for particles of this type. Slugging was achieved at a gas velocity of $2 U_{mf}$, giving the result of a more rapid transition from bubbling to slugging for larger particles.

The minimum fluidization velocity was estimated by connecting the two linear regions of pressure drop behavior, and determining the corresponding value of U_s at the intersection. As it turned out, the particle Reynolds number at fluidization, $Re_{p,mf}$, remained below 20 for each of the materials. This verified the use of the simplified equation 1.8 for particles with small Reynolds numbers.

By dividing the superficial gas velocity by the minimum fluidization velocity found this way, and plotting all three materials in the same manner, this result is more easily portrayed. Figure 4.4 shows pressure drop over mean bed height plotted for all three materials. Each data set was plotted against U_s/U_{mf} , with the minimum fluidization velocity for each material determined from Figures 4.1-4.3.

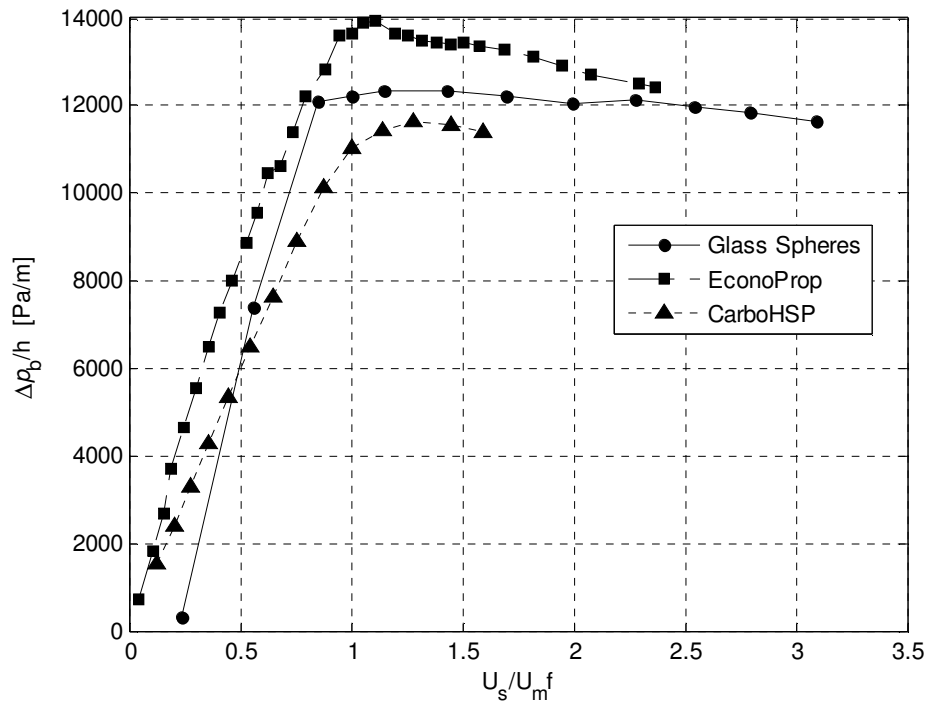


Figure 4.4: Pressure drop over mean bed height plotted against normalized gas velocity for all materials

Plots of void fraction yield qualitatively similar results in regards to transitional behavior near the onset of fluidization. Figures 4.5-4.7 display plots of void fraction versus superficial gas velocity for each of the three materials.

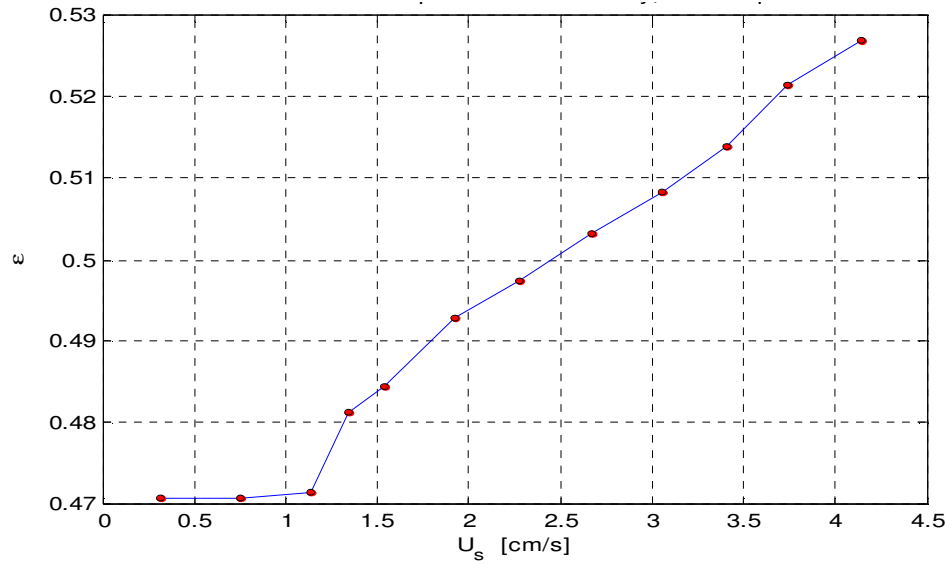


Figure 4.5: Void fraction plotted against superficial gas velocity for the Glass Spheres material

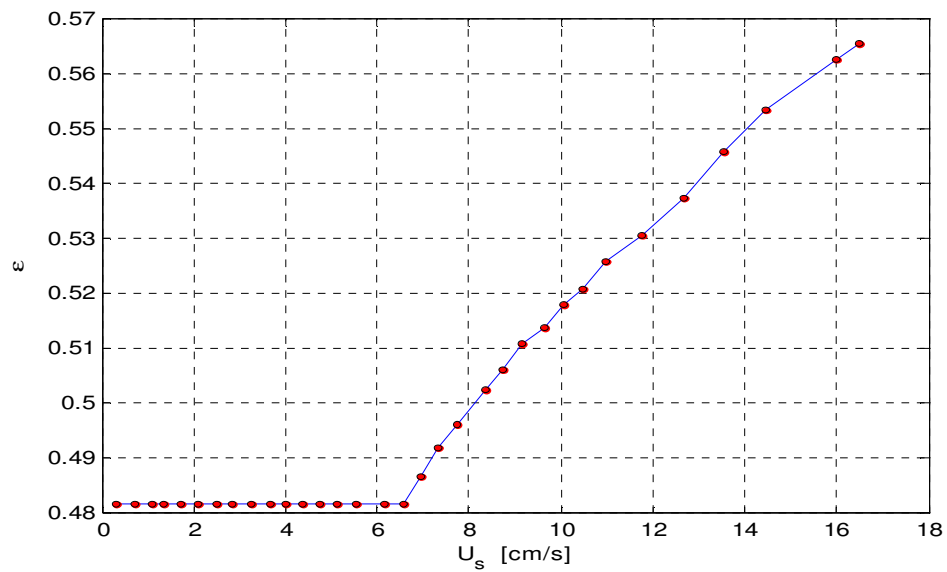


Figure 4.6: Void fraction plotted against superficial gas velocity for the EconoProp material

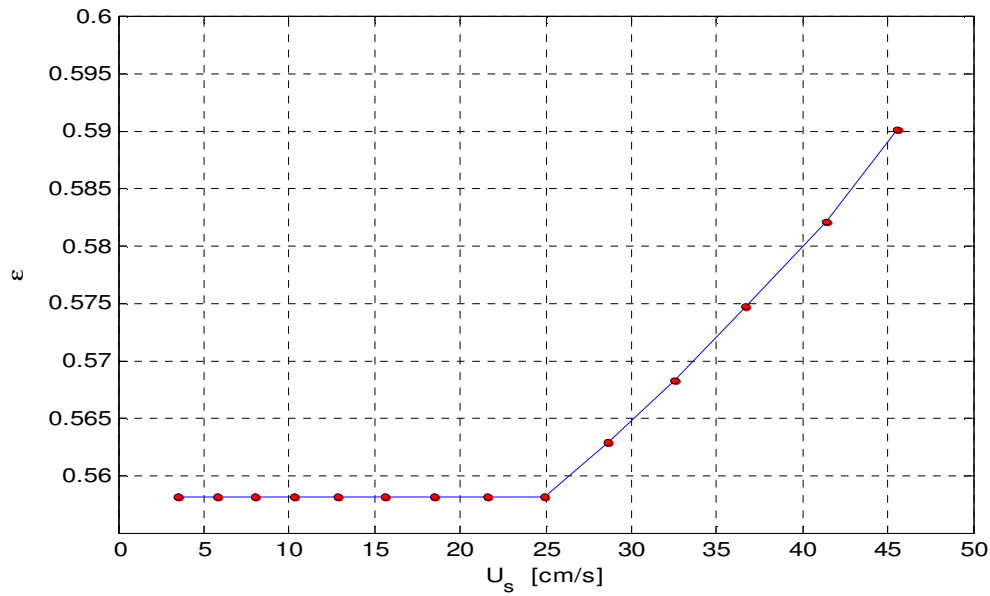


Figure 4.7: Void fraction plotted against superficial gas velocity for the CarboHSP material

From the simple fact that the bed height does not change until the onset of fluidization, an estimate for U_{mf} is possible by taking the superficial gas velocity at which the void fraction begins to rise. This is easily observed on the figures. By dividing the superficial gas velocity by the minimum fluidization velocity found this way, and plotting all three materials the same way, this result is more easily portrayed. Figure 4.8 shows the void fractions for all three materials, plotted against normalized gas velocity:

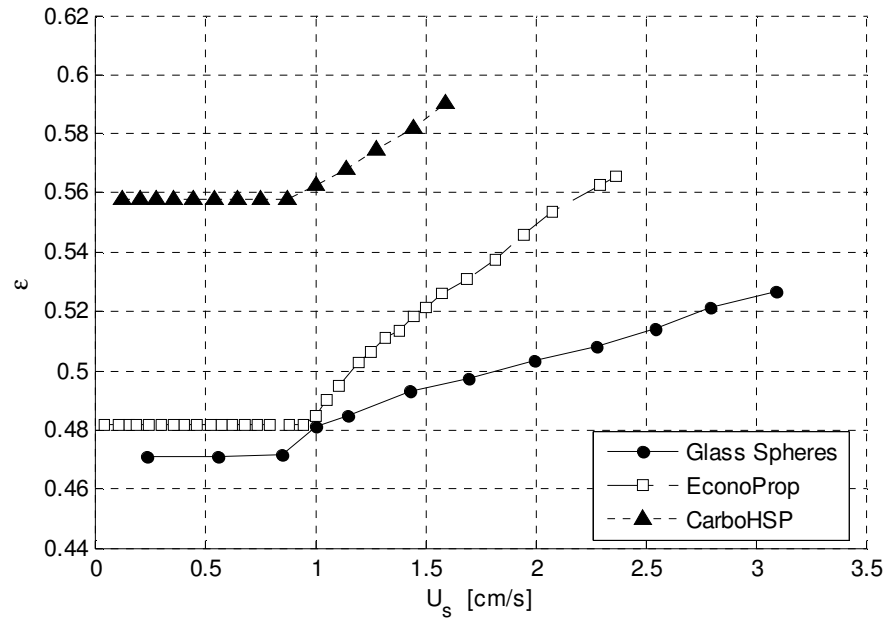


Figure 4.8: Void fraction plotted against normalized gas velocity for all materials

Plotting all three materials together displays the qualitative result of a constant bed height and, thus, void fraction up until the onset of fluidization. Discrepancies in void fraction values between the materials are congruent with the different mean particle diameters. CarboHSP exhibits the highest void fraction at rest, followed by EconoProp and the Glass Spheres.

The values of minimum fluidization velocity estimated from the flow regime diagram given by Reh (1968) were found by computing the Archimedes number corresponding to each particle, and determining the corresponding particle Reynolds number at minimum fluidization. Figure 4.9 shows the estimated $Re_{p,mf}$ values determine for each particle type.

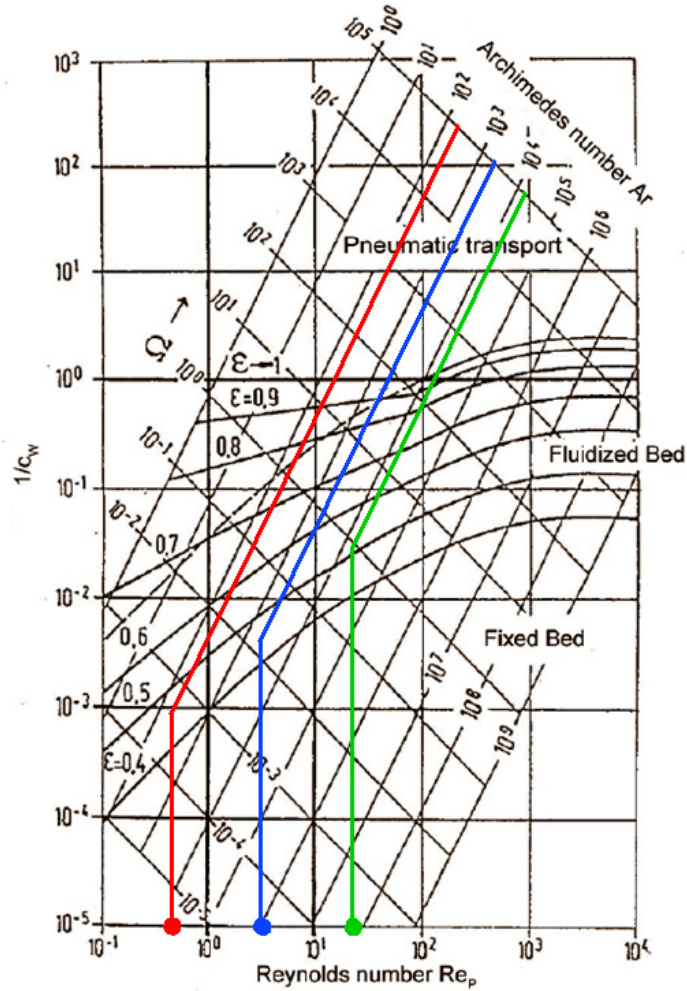


Figure 4.9: Flow regime diagram for vertical fluidized beds, including the bed materials used in this experiment. Red: Glass Spheres; Blue: EconoProp; Green: CarboHSP. Reh (1968)

The values of minimum fluidization velocity determined from equation 1.8, those estimated using the fluidized bed regime diagram, Figure 4.9, and those obtained through the pressure drop and void fraction measurements are given in Table 4.1.

Table 4.1: Comparison of minimum fluidization values determined through experiment, equation 1.8, and Figure 2.9

	Glass Spheres	EconoProp	CarboHSP
U_{mf} Determined from Pressure Drop [cm/s]	1.34	8.61	28.18
U_{mf} Determined from Void Fraction [cm/s]	1.34	6.98	28.18
U_{mf} , predicted from theory [cm/s]	1.43	9.97	32.05
Archimedes number [dimensionless]	182.8	3660.1	11121.1
U_{mf} Determined from flow regime diagram [cm/s]	2.38	14.25	42.50

Minimum fluidization velocity estimates obtained through experiment agreed with those determined from equation 1.8. U_{mf} values estimated using the fluidized bed regime diagram are larger than both the experimental and the theoretical values by 50 – 100%. Exact agreement between values determined from the pressure drop and void fraction methods was the result of testing the beds while using the same discrete values of superficial gas velocity for each material. The minimum fluidization velocities obtained using the pressure drop method were used as they are the medians of the values obtained from the pressure drop, void fraction, and predicted estimates.

4.2 Bed Expansion Ratio

Plots of mean bed expansion ratio versus normalized gas velocity are shown in Figure 4.10-4.12.

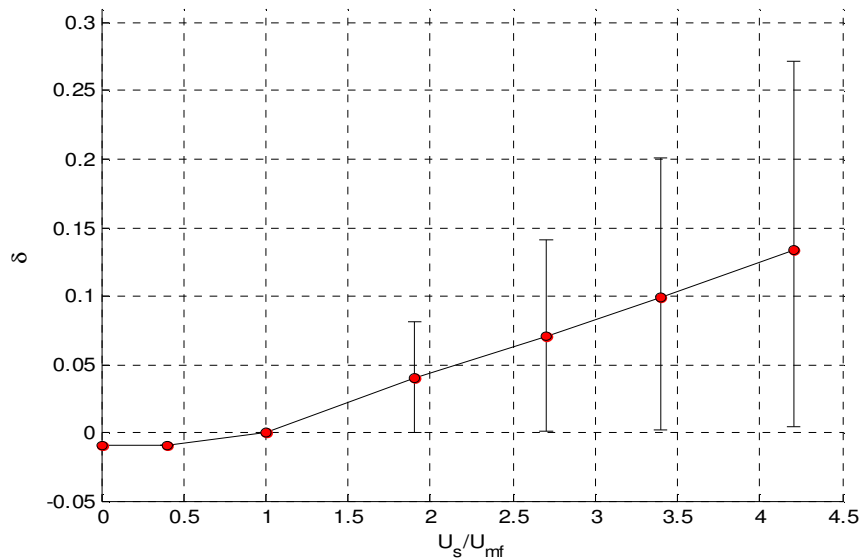


Figure 4.10: Mean bed expansion ratio versus normalized gas velocity for the Glass Spheres material. Also shown are the relative fluctuation heights described by equation 1.5

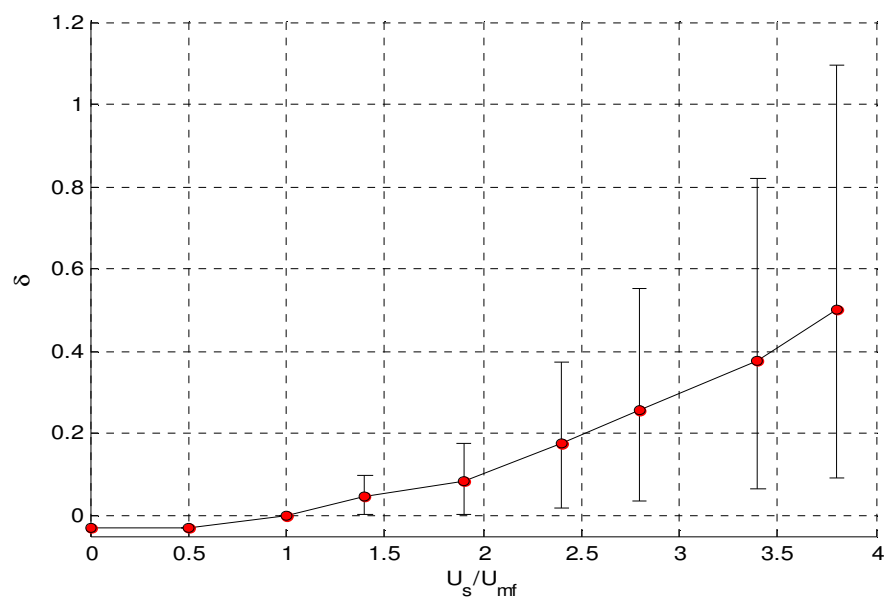


Figure 4.11: Mean bed expansion ratio versus normalized gas velocity for the EconoProp material. Also shown are the relative fluctuation heights described by equation 1.5

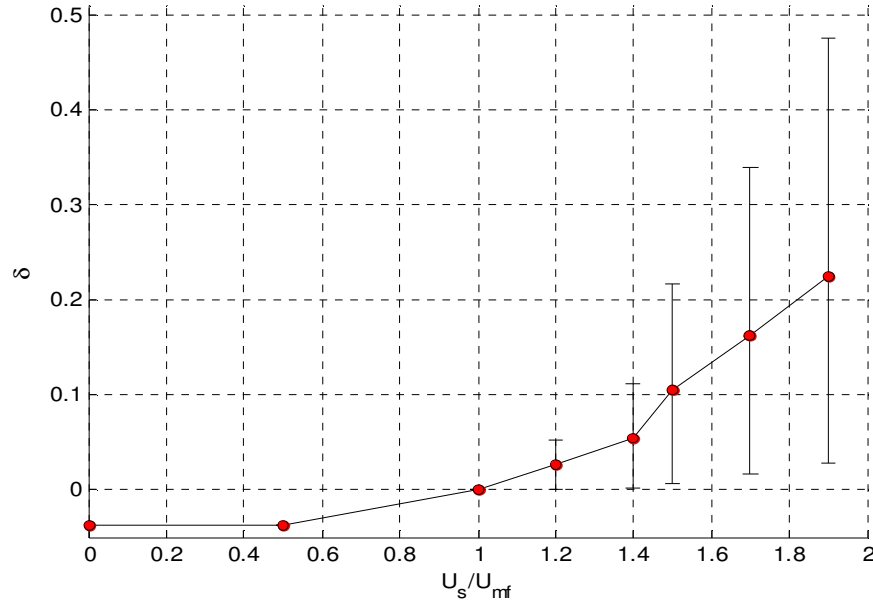


Figure 4.12: Mean bed expansion ratio versus normalized gas velocity for the CarboHSP material. Also shown are the relative fluctuation heights described by equation 1.5

In the case of the glass spheres, the bed expansion ratio displays a linear increase in mean bed expansion ratio following the onset of fluidization. Naturally, the value of $\bar{\delta}$ takes a value of zero at minimum fluidization, since at this point $\bar{h} = h_{mf}$. Notable is the increase in mean bed height fluctuation, denoted by the error bars. In all three plots the upper and lower error bars have lengths of $\delta(\bar{h}_{max})$ and $\delta(\bar{h}_{min})$, respectively. The magnitudes of these values give a picture of the bed height fluctuation at different flow regimes.

As noted in the case of the glass spheres, bubbling commenced immediately following the onset of fluidization. Bubble diameters increased with superficial gas velocities until they approached the diameter of the chamber, resulting in slugging at around $3U_{mf}$. This steady increase in bubble size is portrayed by the increasing amount of bed height fluctuation, visible in Figure 4.10.

Similar behavior is evident in the plots of the EconoProp and CarboHSP materials. The main exception here is that the mean bed expansion ratio of the EconoProp bed increases at a rate that is less linear. The plot of the CarboHSP bed shows an even greater increase in $\bar{\delta}$ with normalized gas velocity. In all three of the materials, the lower ends of the fluctuation, $\delta(\bar{h}_{min})$, rest nearly on the $\bar{\delta}=0$ line, especially in the case of the Glass Spheres. This suggests that the bed collapse after the release of bubbles and/or slugs brings the instantaneous bed height down to a level nearly that at minimum fluidization, h_{mf} .

Examining the mean bed expansion ratio values at $U_s/U_{mf}=2$, we find another trend. The mean bed expansion ratio for each of the three materials at this normalized gas velocity is larger for an increasing particle diameter. Physically speaking, the mean bed height relative to h_{mf} for each of the materials is higher at the same relative superficial gas velocity for the larger particles. The same is true for fluctuation values at similar normalized gas velocities. This is indicative of the more rapid transition to the slugging regime for larger bed materials.

Bed expansion ratio results from simulation are shown in Figure 4.13. In each of the figures, one of four parameters of interest are varied: the particle-particle restitution coefficient, the particle-wall restitution coefficient, the boundary condition, and the solid phase stress model.

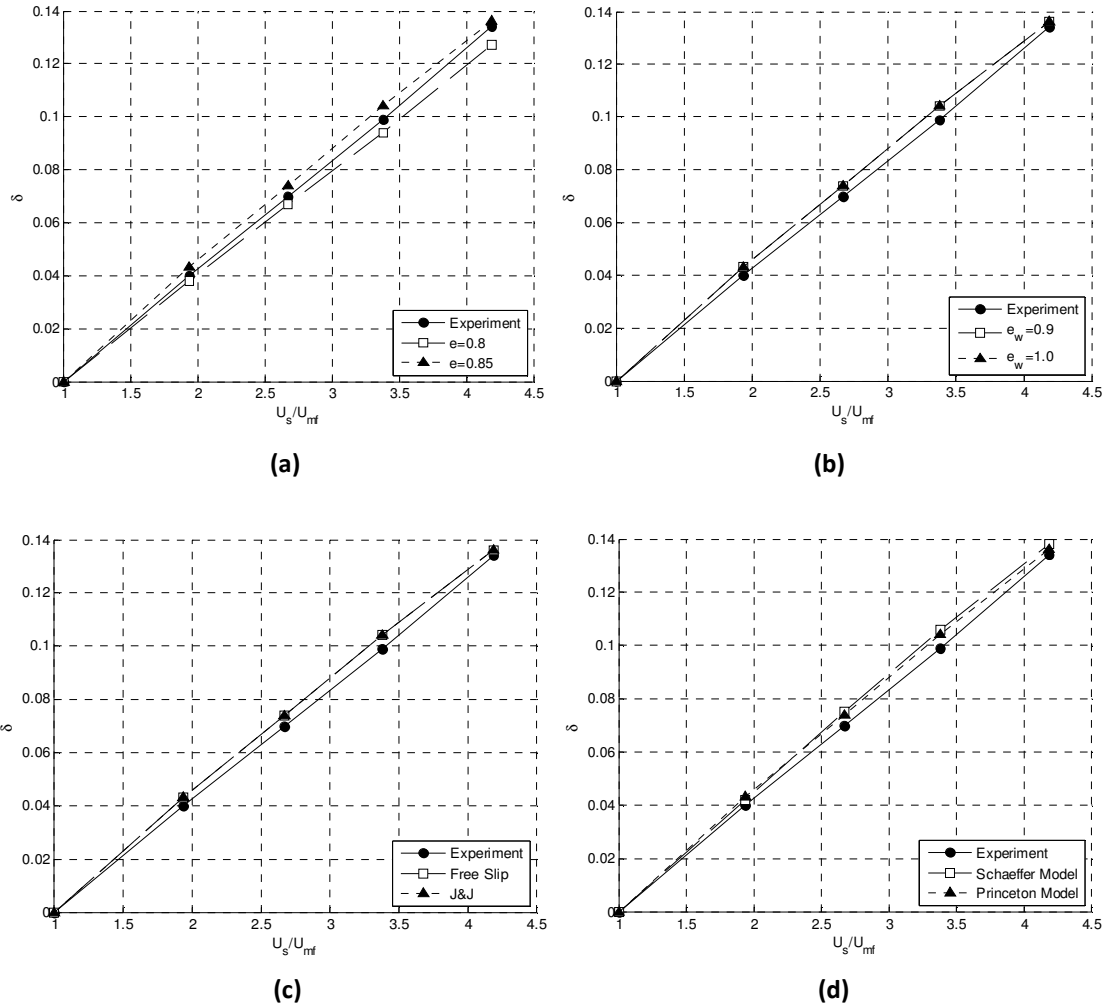


Figure 4.13: Comparison of mean bed expansion ratio versus normalized bed height for the Glass Spheres material for experiment and simulation. (a) Particle-particle restitution coefficient is varied (b) Particle-wall restitution coefficient is varied (c) Boundary condition is varied (d) Solid phase stress model is varied

It appears that the only parameter that produced a significant change when varied is the particle-particle restitution coefficient. This follows from the findings of Taghipour et al. (2005), who reported that the bed expansion is seen to decrease with lower value of e . Indeed, the only simulation run with a particle-particle restitution

coefficient value of 0.8 was also the only data set with mean bed expansion ratio values lower than those obtained from experiment.

In each case the simulated values fell within 6% of experimental bed height ratios, with the highest discrepancy being in the bubbling regime. The simulated and experimental data exhibit a near-linear dependence on superficial gas velocity for this material.

Figure 4.14 portrays the same comparison between experiment and simulation for the EconoProp bed material.

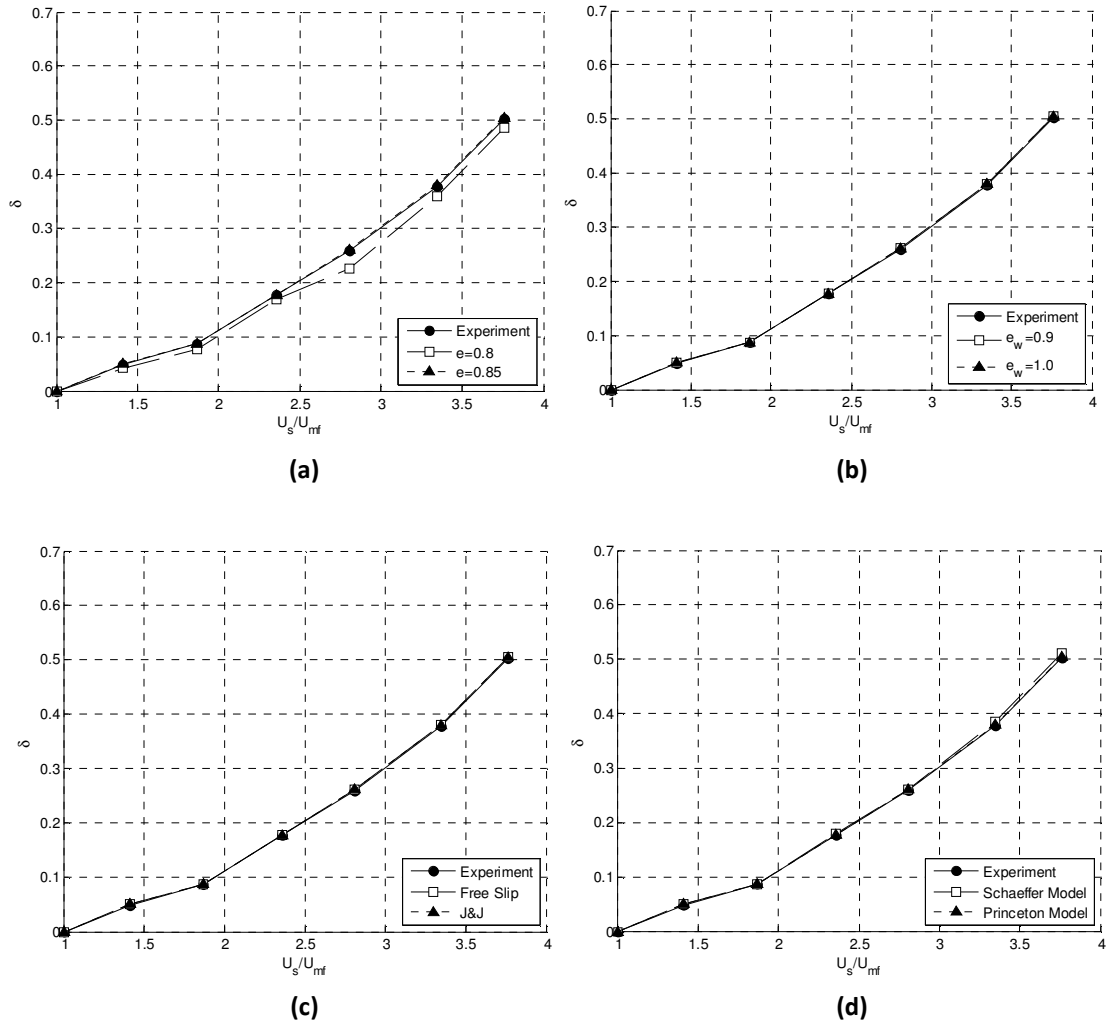


Figure 4.14: Comparison of mean bed expansion ratio versus normalized bed height for the EconoProp material for experiment and simulation. (a) Particle-particle restitution coefficient is varied (b) Particle-wall restitution coefficient is varied (c) Boundary condition is varied (d) Solid phase stress model is varied

The same trend is seen for the EconoProp material. Though the relationship between mean expanded bed ratio is less linear, the simulated data matches very closely with experiment. Mean bed expansion ratio increases more rapidly in the slugging regime. The simulation run with a particle-particle restitution coefficient of

0.8 yields lower values of mean bed expansion ratio, as expected. Figure 4.15 shows the same plots for the largest material, CarboHSP.

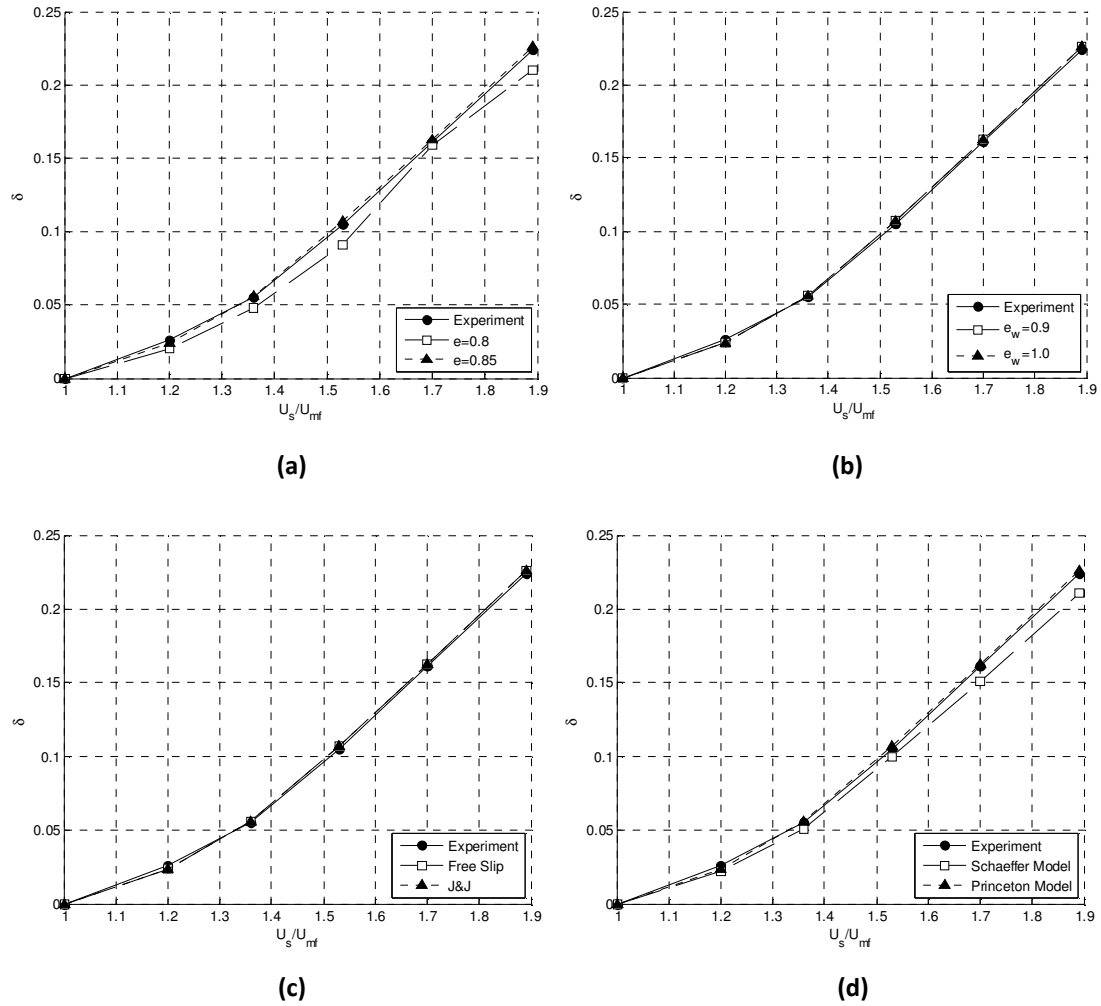


Figure 4.15: Comparison of mean bed expansion ratio versus normalized bed height for the CarboHSP material for experiment and simulation. (a) Particle-particle restitution coefficient is varied (b) Particle-wall restitution coefficient is varied (c) Boundary condition is varied (d) Solid phase stress model is varied

In general, the larger bed materials exhibit higher expansion ratios at a given normalized gas velocity. This results from a more rapid transition from the bubbling

to the slugging regimes as demonstrated by the materials with larger mean particle diameters.

The lower values of mean bed expansion ratio seen for all materials simulated with $e = 0.8$ follow from the higher inelasticity of particle-particle collisions. As discussed in Reuge et al. (2008), a decrease in this coefficient leads to higher kinetic energy fluctuations. However, a higher portion of this energy is dissipated through inelastic collisions. This leads to higher pressure fluctuations throughout the bed, but to lower bed height and granular temperature values.

Variability in the particle-wall restitution coefficient yielded no substantial change in bed expansion values. This result is to be expected, as the bulk of the material has no contact with the wall while under fluidization. The bed expansion plots showing simulations for e_w values of 0.9 and 1.0 were included to show this, and to keep consistent with the parameters changed when determining granular temperature.

For the same reason, there is not much variability when considering the boundary conditions. These results are consistent with those of Reuge et al. (2008) who noted “nearly identical results” when comparing the simulations using free-slip at the wall versus Johnson-Jackson boundary conditions.

There was some variability when comparing the simulations using the Schaeffer versus Princeton models of solid phase stresses. The Princeton model yielded values that were closer to those achieved from experiment. This is also consistent with 3D simulations performed by Reuge et al. (2008), who noted that the Princeton model gave “always significantly better results” than the Schaeffer model.

4.3 Cylinder Transfer Function

Time signals from the impact hammer and the wall-mounted accelerometer were recorded via LabVIEW and analyzed in Fourier space. Figure 4.16 shows an example of this impulse-response analysis, depicting plots taken from the LabVIEW program shown in Appendix A.

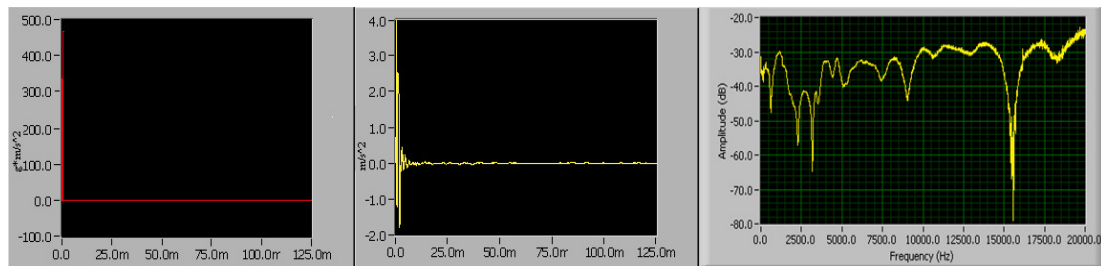


Figure 4.16: From left to right: (A) Time signal of the impulse hammer. The x-axis is given in ms. (B) Time signal of the accelerometer response. The x-axis is given in ms. (C) Corresponding transfer function. Amplitude is given in decibels.

The transfer functions resulting from three individual impacts at different vertical positions on the cylinder wall are shown in Figure 4.17. Each hit was diametrically opposed to the accelerometer mount such that the direction of the impulse hammer was normal to the accelerometer.

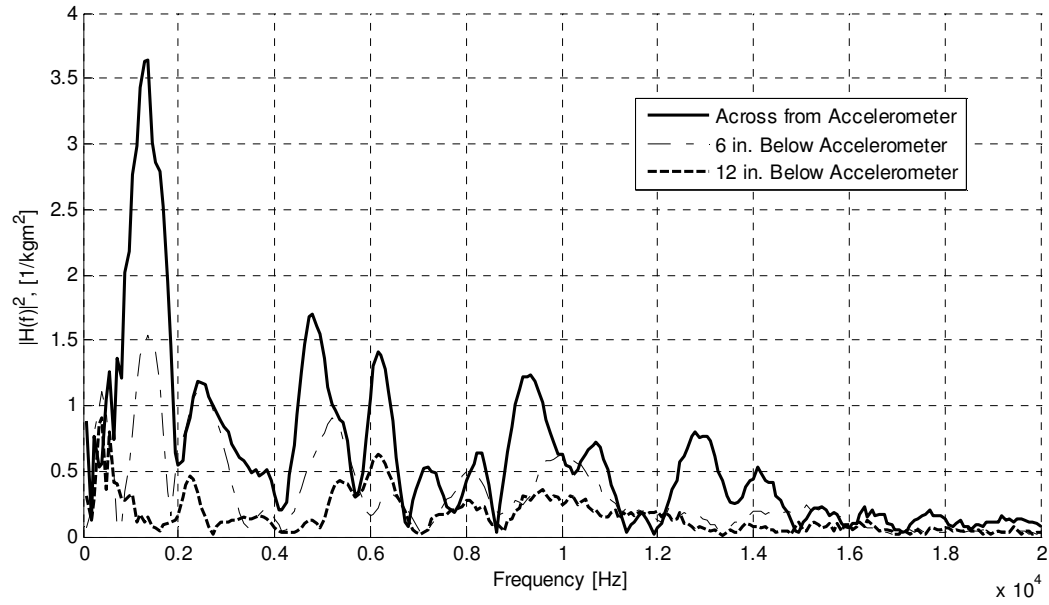


Figure 4.17: $|H(f)|^2$ computed from hammer impacts at various locations on the cylinder wall, at a circumferential location that was diametrically opposite from the accelerometer

It is clear that the magnitude of $|H(f)|^2$ decreases as the distance of the impulse hammer impact from the accelerometer increases. This corresponds to energy lost over the cylinder wall at greater distances. Also noteworthy is the increased rigidity of the structure when moving down towards the reservoir chamber, which is rigidly attached to the outer steel structure.

To visualize the effects of impulse forces at different circumferential positions, transfer functions corresponding to these impacts are plotted in Figure 4.18. Each of the hammer impacts were performed at a vertical distance of 7.6 cm (3.0 in) below the accelerometer. The areas of interest, denoting the position of the accelerometer at 0° , were 0° , 90° , 180° , and 270° , moving clockwise while looking down. The transfer functions for each of these areas were calculated as the average of five consecutive

impacts. The vertical scales of each plot are held constant to highlight magnitude differences.

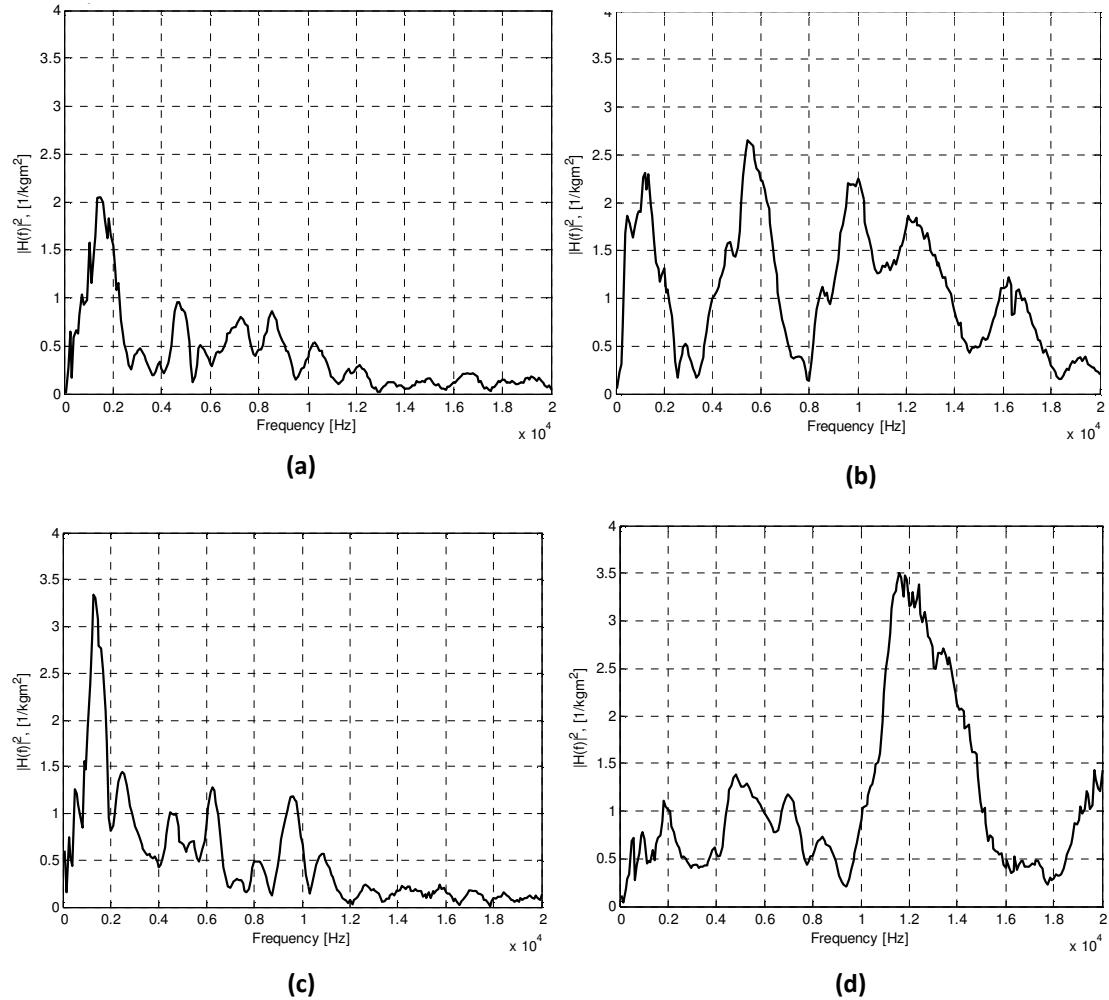


Figure 4.18: Transfer function resulting from hammer impacts at different circumferential positions at a vertical location 3" below the accelerometer. Each plot represents the average of 5 hits. (a) 0° from direction of accelerometer reading (b) 90° (c) 180° (d) 270°

The transfer functions resulting from “in-line” hammer impacts – that is, those in the same or opposing directions (0° and 180°) to the accelerometer – are clearly different from those resulting from side impacts (90° and 270°). The most important distinction is the notably higher magnitude of $|H(f)|^2$ in the 10-20 kHz frequency

range of interest resulting from the side impacts. The importance of averaging over 8 circumferential positions and spanning vertically over the portion of the tube that is touched by bed material is realized from the previous figures.

Averages of the transfer function over the entire cylinder wall were computed under four conditions. During the first three, the fluidization chamber was filled with the same amount of bed material used in the other portions of this experiment corresponding to the three bed materials tested. Lastly, the empty chamber was tested for structural response to compare the effects on energy propagation caused by packed bed material. Computed values of the integral of the average transfer function in each case, defined by equation 2.15, are given in Table 4.2.

Table 4.2: I^2 values computed from equation 2.15 with the fluidized chamber filled with each material type, as well as with an empty chamber.

	Glass Spheres	EconoProp	CarboHSP	Empty Cylinder
I^2 [$\text{kg} \cdot \text{s}^{-1}$]	1.10×10^7	3.31×10^7	9.80×10^6	8.97×10^7

Values of I^2 found with the cylinder full of bed material vary within an order of magnitude of one another. The bed material filled with the CarboHSP yielded the average transfer function with the lowest magnitude, while the EconoProp-filled chamber gave the highest. Physically, this can be explained by the CarboHSP absorbing and dissipating more of the energy from the impact hammer than the EconoProp particles. This suggests higher inelasticity for the CarboHSP particles.

The average transfer function found from the empty cylinder had the highest magnitude. This is expected, as a structure without particles touching the wall should realize less energy dissipation than that of a structure filled with a bed material.

When employing equation 2.16 for each material, the corresponding values of I^2 given in Table 4.2 were used.

4.4 Mean-Squared Acceleration at the Wall

In a manner similar to that of the cylinder transfer function, the mean-squared acceleration at the wall is computed by integrating the power spectral density of the accelerometer time signal in the 10-20 kHz frequency range. Following equation 2.14, the first step consists of finding the mean-squared acceleration due to noise. This quantity was found by recording the accelerometer time signal with the bed at rest. Figure 4.19 displays the power spectral density according to these conditions for the Glass Spheres-filled fluidization chamber, in decibels.

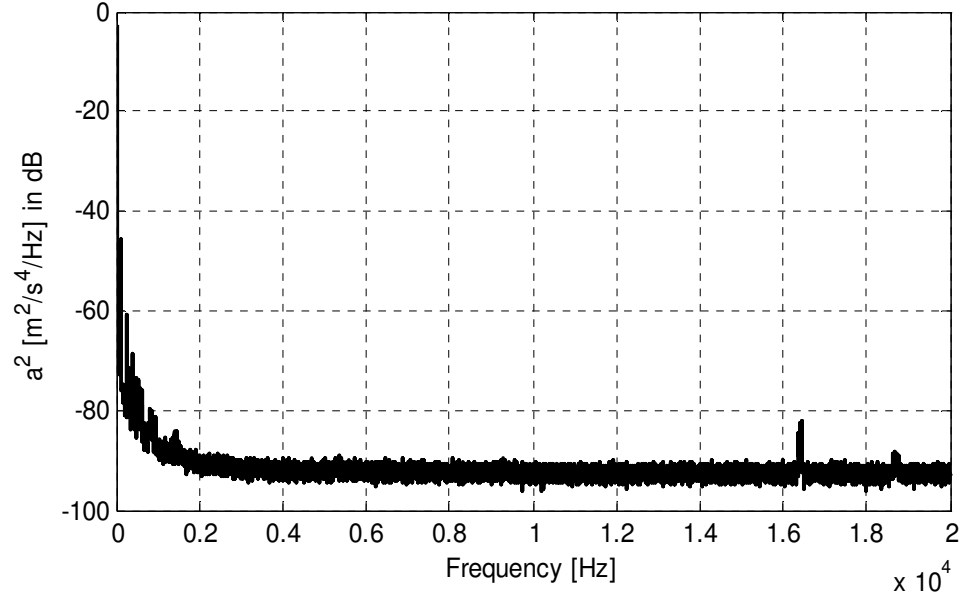


Figure 4.19: Power spectral density of the accelerometer signal taken with the bed at rest

Integration of this function from 10-20 kHz yields a_n^2 . Values of this mean-squared acceleration did not vary significantly due to different types of bed material used. This follows from the fact that any significant vibration of the structure when the bed is not fluidized is caused mainly by outside forces, e.g. vibrations of the surrounding building. These low-frequency effects are shown in the initial spike seen in the 0-1 kHz range of Figure 4.19.

The acceleration power spectral densities obtained from running the fluidized bed at various velocities for each material are shown in Figures 4.20-4.22.

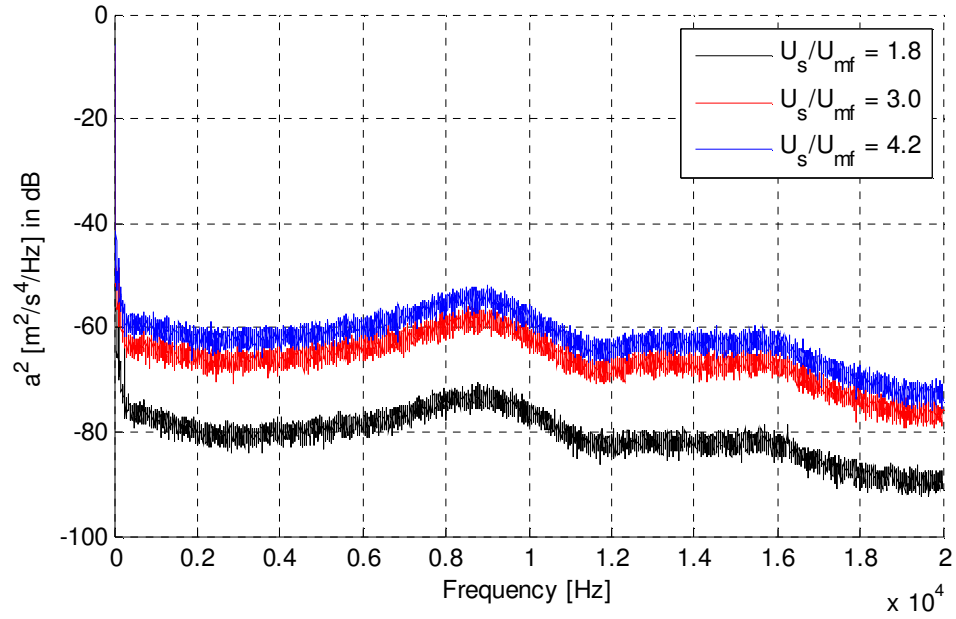


Figure 4.20: Power spectral density of accelerometer signals taken at various superficial gas velocities for the Glass Spheres material. Legend locations correspond to respective locations in the graph (e.g. the top-most entry in the legend corresponds to the top-most data in the plot)

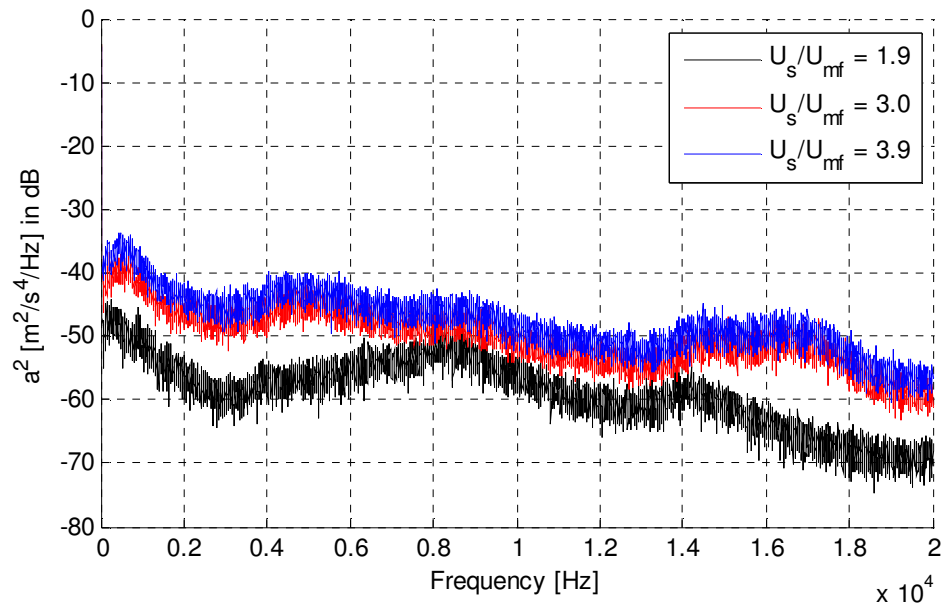


Figure 4.21: Power spectral density of accelerometer signals taken at various superficial gas velocities for the EconoProp material. Legend locations correspond to respective locations in the graph (e.g. the top-most entry in the legend corresponds to the top-most data in the plot)

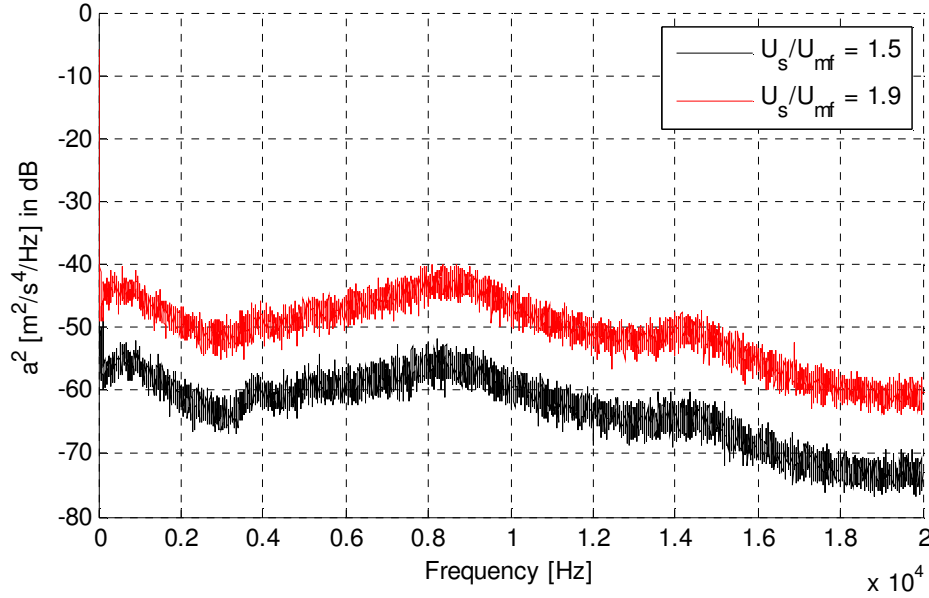


Figure 4.22: Power spectral density of accelerometer signals taken at various superficial gas velocities for the CarboHSP material. Legend locations correspond to respective locations in the graph (e.g. the top-most entry in the legend corresponds to the top-most data in the plot)

The acceleration power spectral densities are dominated by white noise, as predicted (Cody et al., 1996). No resonant frequencies are present in the spectrums shown.

The increase in wall acceleration is obvious with increasing gas velocity. This shifting of the noise levels to higher values corresponds to the physical mechanism of higher particle velocities when they collide with the wall. As shown in the graphs for the Glass Spheres and EconoProp, there is also a significant drop in the rate of this increase caused by higher gas velocities.

Integration of these individual power spectral densities yields the total mean-squared acceleration, a_m^2 , at various fluidization velocities. By subtracting the noise term a_n^2 from each of these values, the experimental values of a^2 are found.

4.5 Average Particle Normal Velocity

The use of equation 2.16 gives particle normal velocity profiles for each of the three materials. The quantity a^2 was determined for various gas velocities, as noted. This procedure was repeated three times for each of the materials, and the average normal particle velocities are plotted in Figures 4.23-4.25.

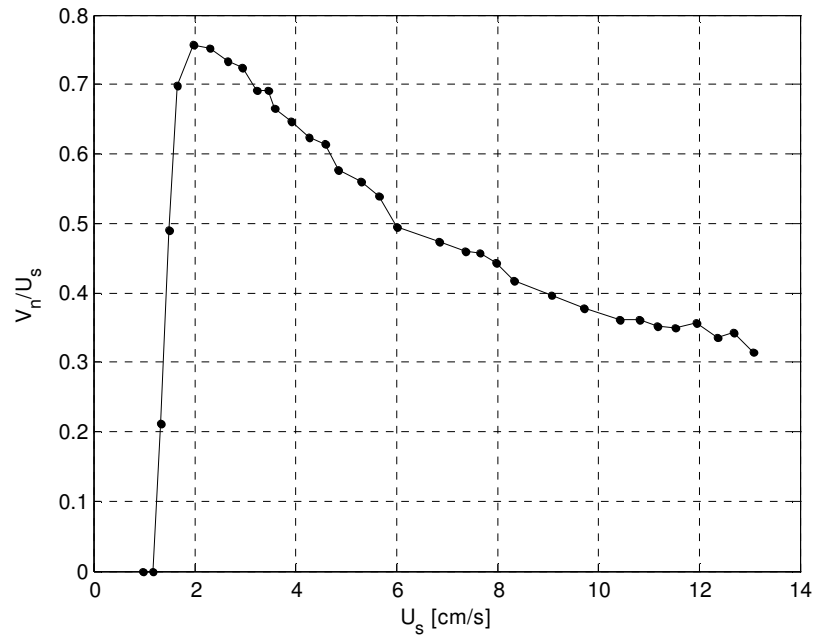


Figure 4.23: Particle velocity normal to the wall, divided by superficial gas velocity, plotted against superficial gas velocity for the Glass Spheres material. Data shown is the mean of three separate runs

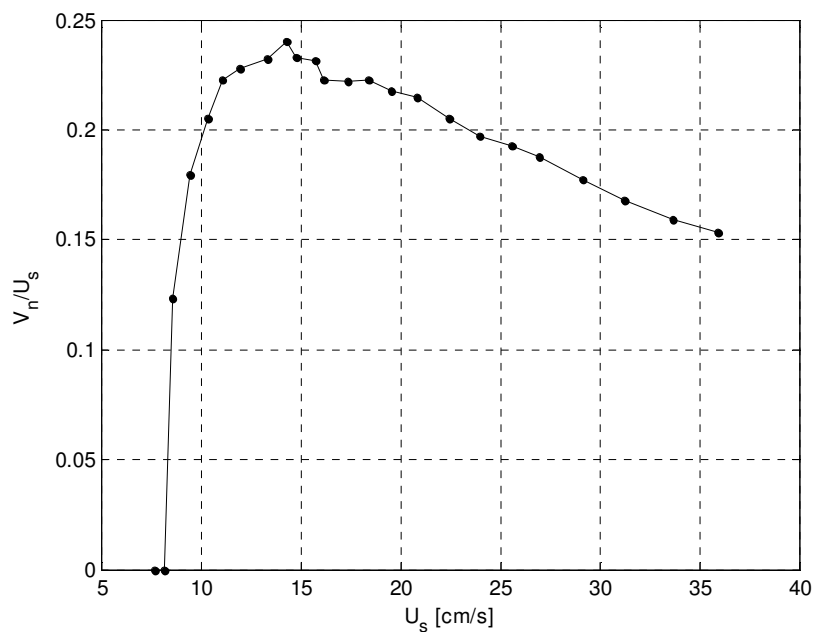


Figure 4.24: Particle velocity normal to the wall, divided by superficial gas velocity, plotted against superficial gas velocity for the EconoProp material. Data shown is the mean of three separate runs

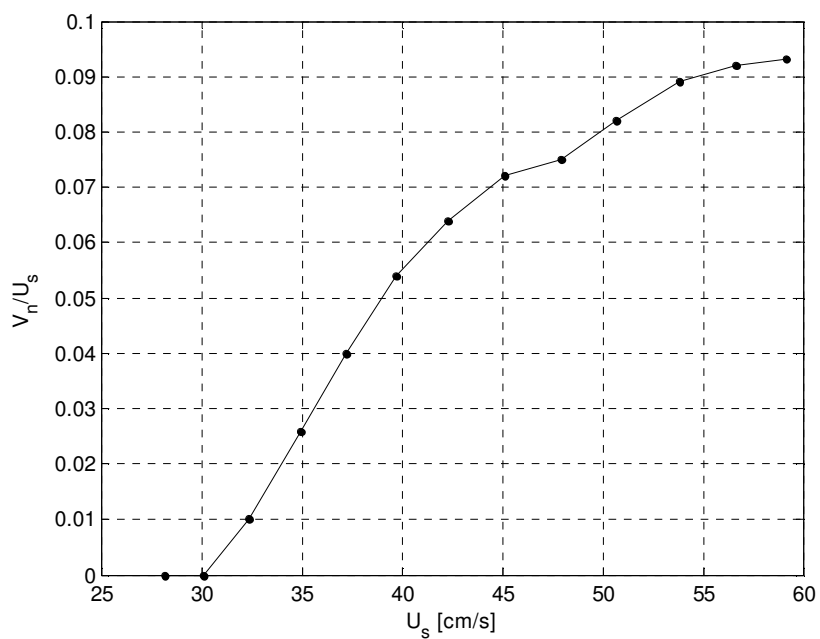


Figure 4.25: Particle velocity normal to the wall, divided by superficial gas velocity, plotted against superficial gas velocity for the CarboHSP material. Data shown is the mean of three separate runs

The plots of experimentally-determined normal particle velocity versus normalized gas velocity for the three Geldart B materials show qualitative similarities to the results obtained by Cody et al. (1996). In the case of the monodisperse Glass Spheres, a nearly linear region of gain is followed by a drop to a nearly-constant value at higher gas velocities. This corresponds to a quadratic increase in V_n in this section. This initial region is indicative of the beginning of bubbling following the onset of fluidization. The subsequent decrease in normalized particle velocity measurements corresponds to the increased dilution of the system due to bed expansion. As the interstitial space between particles is increased, a smaller percentage of the gas kinetic energy is transferred to random particle motion, resulting in the decrease seen after $2U_s/U_{mf}$.

The experimental particle normal velocity plots for the EconoProp and bed material exhibits similar behavior. The regions of initial increase are followed by a transition and subsequent decrease. Plotting V_n/U_s for all three materials together against the normalized gas velocity makes it easier to observe similarities and differences among the different regimes of each particle type.

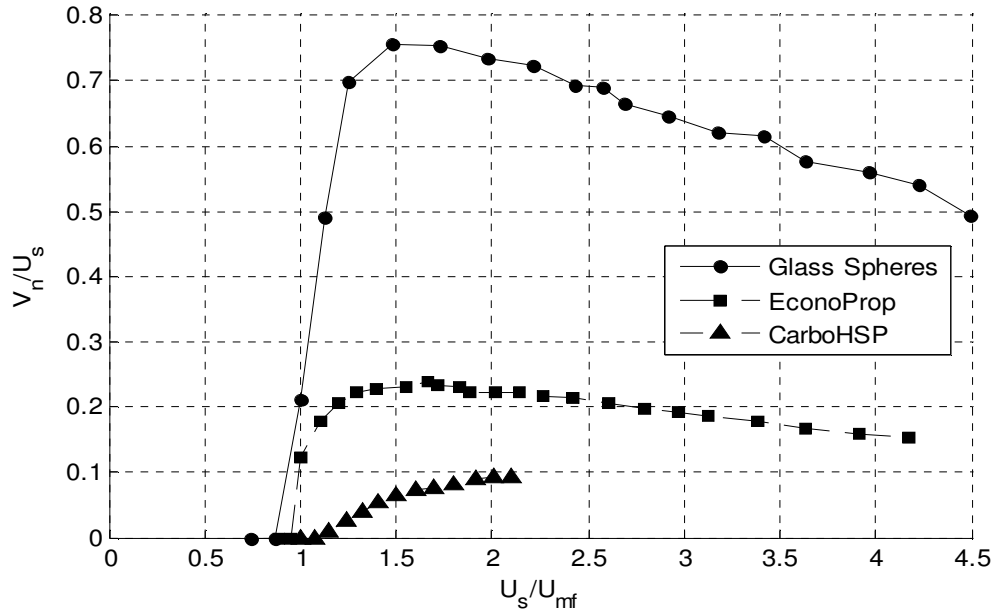


Figure 4.26: Particle velocity normal to the wall, divided by superficial gas velocity, plotted against normalized gas velocity for all materials. Data shown is the mean of three separate runs

Figure 4.26 displays the experimentally-measured normal particle velocities tested for each material, plotted against U_s/U_{mf} . The region of quadratic increase in V_n is seen in all three cases, followed by transition to a region of linear increase in particle normal velocity with increasing superficial gas velocity. Physically, the region of quadratic increase corresponds to the bubbling regime of the fluidized bed, while the linear dependence is indicative of the slugging regime.

The visual results mentioned earlier regarding fluidization regimes for each bed material agree with these results. Bubbling was seen to occur at or immediately following the beginning of fluidization, matching the quadratic increase in V_n seen occurring at $1 U_s/U_{mf}$. The onset of slugging for the Glass Spheres, EconoProp, and CarboHSP materials were $3 U_s/U_{mf}$, $2.5 U_s/U_{mf}$, and $2 U_s/U_{mf}$, respectively. The values

of U_g/U_{mf} at which the transition from quadratic to linear dependence ends agrees with these values.

4.6 Comparison of Normal Particle Velocity Results with Simulation

Simulations were carried out by (Didwania et al., to appear) at the same U_g/U_{mf} values used for the experimental data. Four main parameters were varied throughout simulation: the particle-particle restitution coefficient, e (0.8 or 0.85); the particle-wall restitution coefficient, e_w (0.9 or 1.0); the boundary condition type (free-slip at the wall or Johnson & Jackson); and the solid phase stress model (Schaeffer or Princeton). Each plot presented displays three sets of data: the experimental data and the simulation data produced using the Schaeffer and the Princeton models. Each plot produced is thus one of the eight possible variances of the first three parameters. All 24 plots (8 for each material type) are displayed in the Appendix B. Only the most important plots are presented in this section.

Figure 4.27 displays several comparisons among simulation and experimental values of particle normal velocity plotted against normalized gas velocity for the Glass Spheres material.

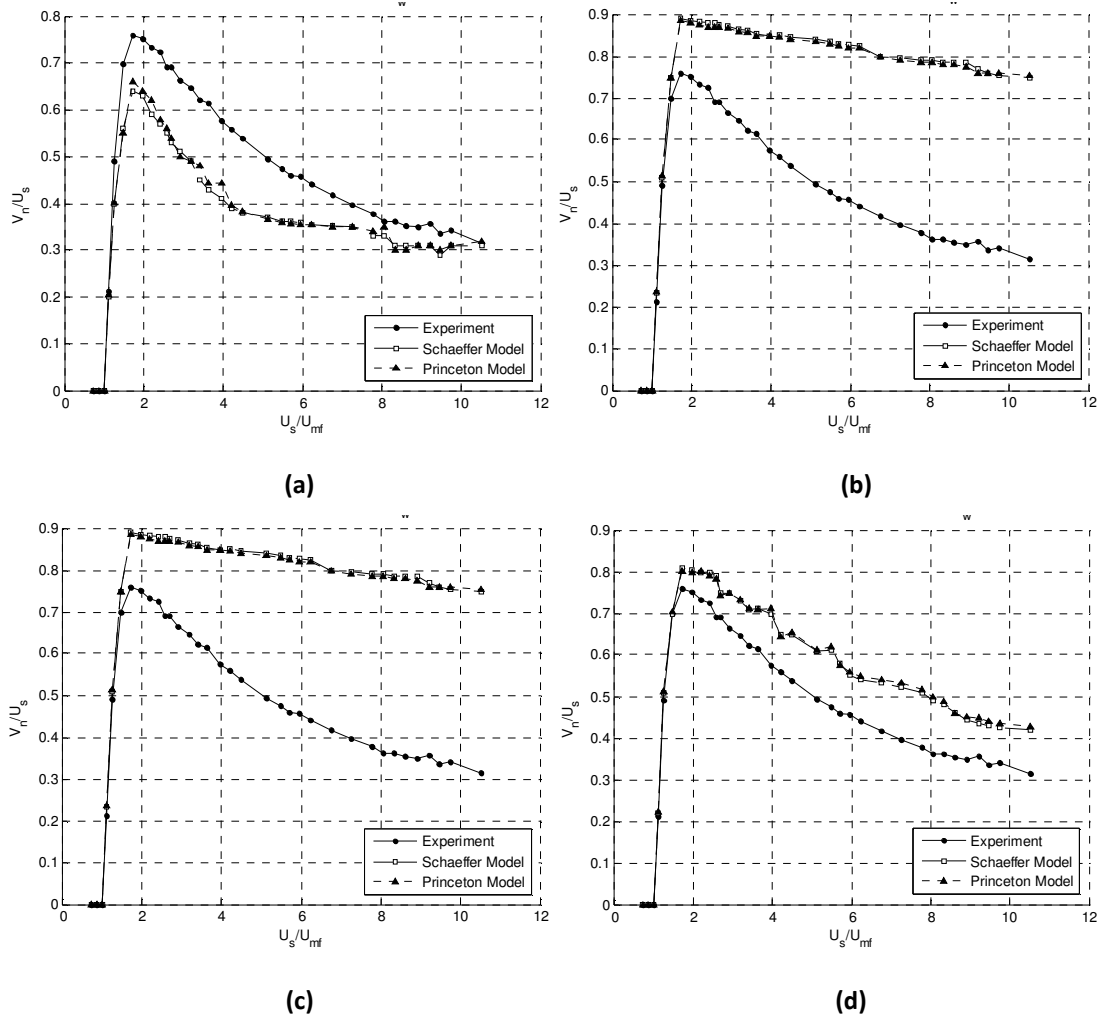


Figure 4.27: Simulated and experimental particle normal velocity data for the Glass Spheres material using various parameter combinations as described above each graph. Data is plotted against normalized gas velocity

Immediately evident in these plots is a common trend. Figure 4.27(a) is the only plot in which the simulated values of normal particle velocity run lower than those obtained from experiment. Similar to the results of the mean bed expansion ratios, a lower particle-particle restitution coefficient is congruent with higher energy dissipation between particles, with the result of lesser bed expansion and a smaller granular temperature. Also notable is a more rapid rate of V_n/U_s decrease for the $e =$

0.8 plots than for those with a value of 0.85. This is indicative of the smaller percentage of the kinetic energy passed from the gas to the particles being retained in the form of granular temperature.

Figures 4.27(b)-(d) display predicted particle velocities higher than those obtained from experiment, with those computed using the free-slip boundary condition exhibiting values up to 120% higher than the experimentally-determined velocities. It is evident that the values produced using the Johnson-Jackson boundary conditions are significantly lower than those obtained under the free-slip assumption.

Comparing Figure 4.27(b) & (c) shows very little discrepancy between particle velocities found using different particle-wall restitution coefficients. This is in agreement with earlier bed expansion ratio results, which exhibited minimal differences in δ calculated from simulations using value of $e_w = 0.9$ or 1.0 .

Finally, comparing the simulated data from each of the previous four figures, there is very little difference between particle velocities computed from either the Schaeffer or the Princeton stress models.

Figure 4.28 shows the same set of plots for the EconoProp material.

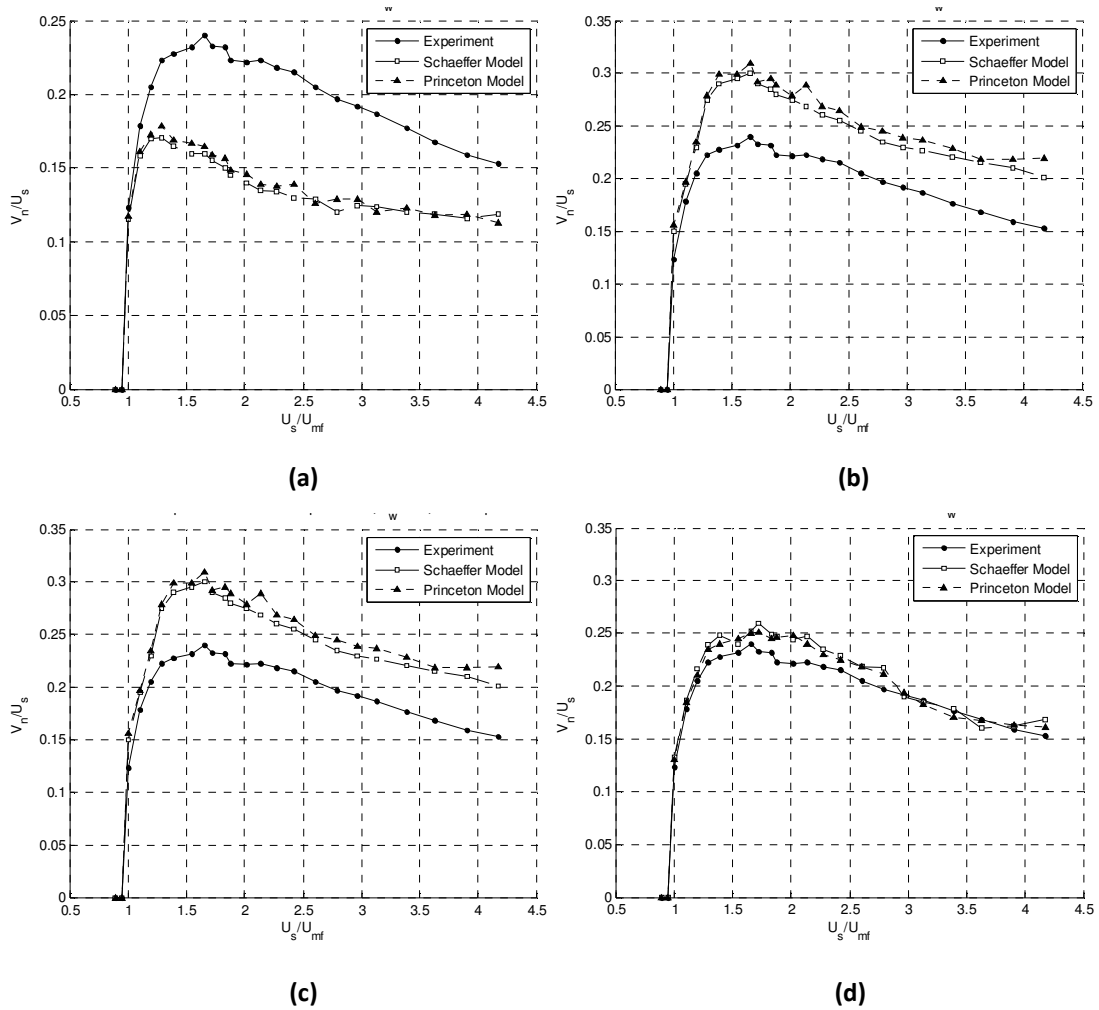


Figure 4.28: Simulated and experimental particle normal velocity data for the EconoProp material using various parameter combinations as described above each graph. Data is plotted against normalized gas velocity

Very similar qualitative results are seen between the experimental and simulated values of particle normal velocity computed for the Glass Spheres and EconoProp materials. Notably, the particle-particle restitution coefficient of 0.8 again produces the only particle velocity values below those obtained from experiment, with slight exception to Figure 4.28(d). The higher energy dissipation resulting from an $e = 0.8$ value yields, in this case, V_n/U_s values slightly over 50% of those obtained using a particle-particle restitution coefficient of 0.85 .

As before, little variability is seen between simulations using either of the two different particle-wall restitution coefficients. Values of particle normal velocity obtained using the Johnson-Jackson boundary conditions show the best agreement with experimentally-determined values, as before. Likewise, the amount of variability between values obtained using either of the two solids phase stress models is small, though more noticeable than in the case of the glass spheres.

The rate of decrease in normalized particle velocity after the initial quadratic behavior is nearly constant among all four plots in Figure 4.28. This is in contrast to the plots of the Glass Spheres material, showing variability in this factor between data sets produced while using different particle-particle restitution coefficient values and boundary conditions.

Plots comparing simulation and experimental data of particle normal velocity for the final material, CarboHSP, are shown in Figure 4.29.

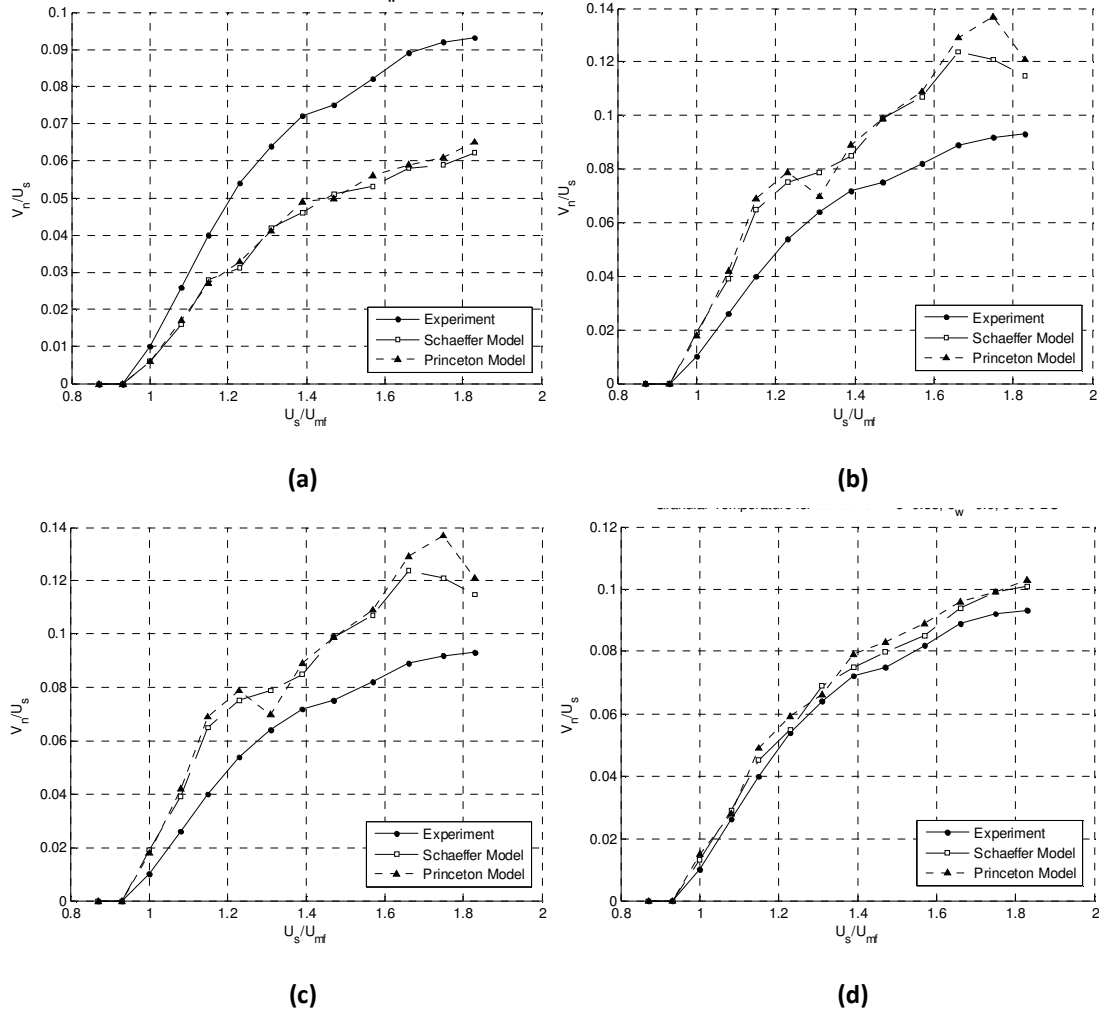


Figure 4.29: Simulated and experimental particle normal velocity data for the CarboHSP material using various parameter combinations as described above each graph. Data is plotted against normalized gas velocity

The trend of higher particle normal velocity with an increased particle-particle restitution coefficient is continued with the CarboHSP material. Notable in this case, however, is the significantly smaller rate of increase of the quantity V_n/U_s . As seen in Figure 4.27 & 4.28, the initial rate of increase remained nearly constant between the different parameter combinations used. The decreased rate corresponding to the $e = 0.8$ value is indicative of a higher percentage of energy that is dissipated in the initial

bubbling regime by the CarboHSP particles during this particular simulation. On the other hand, Figures 4.29(b) & (c) show a higher rate of increase of the simulated particle velocity. The simulation with the best fit, as before, employ the Johnson & Jackson boundary conditions with a particle-particle restitution coefficient of 0.85 . This result leads to an initial conclusion that the partial slip model is more effective in modeling the system described in this experiment. It is noted that the discrepancy between models using the partial slip and the free slip boundary conditions may be diminished significantly when considering a larger experiment. Considering a tube with a much larger diameter, for example, it would be expected that the effects of the confining boundary play less of a role in the overall dynamics of the bed.

5. Conclusions

Experiments were performed on a laboratory-scale, cold-flow gas fluidized bed. Results were compared with those obtained through numerical simulation to validate certain parameters used in the constitutive equations used to describe the two-phase flow. Quantities such as mean bed height, mean expansion ratio, void fraction, minimum fluidization velocity, and pressure drop across the bed were obtained and compared to established theory to provide an initial validation of the experiment. The granular temperature near the wall of the fluidized bed was measured using an acoustic shot noise probe and compared to simulated values.

Bed expansion ratio values determined through experiment were compared with those obtained from simulation. Good qualitative and quantitative agreement was found in these data sets, with variability visible due mainly to different particle-particle restitution coefficients used in the model. Data sets resulting from changes in other parameters yielded little or no difference in mean bed expansion values.

The granular temperatures determined using three different materials were all qualitatively similar when displayed as a function of gas velocity. Particularly, initial increases in particle velocity were proportional to the square of the superficial gas velocity being tested. After a common transitional period, a linear relationship was observed between particle velocity normal to the wall and superficial gas velocity. This behavior of particle velocity agreed with that obtained from a similar experiment using particles in the Geldart B regime (Cody et al., 1996).

Further, all of the simulated data were in agreement with this qualitative behavior, with quantitative variability present owing to the use of different parameters in the models. Comparisons among experimental data and those obtained from simulations using various combinations of the parameters of interest will be used to fit these values. The parameters which yielded the highest variability in particle normal velocity when changed were the particle-particle restitution coefficient and the boundary condition at the surface of the cylinder.

Appendix A: Data Acquisition System

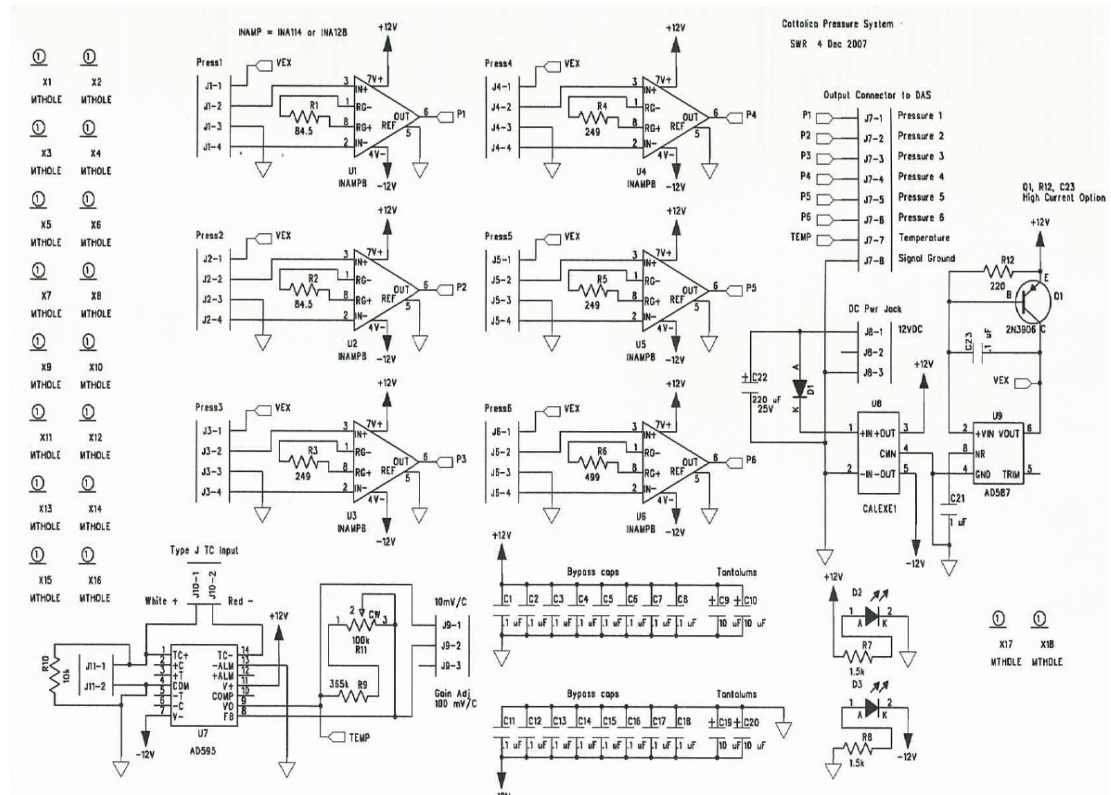


Figure A.1: Signal processing circuit diagram

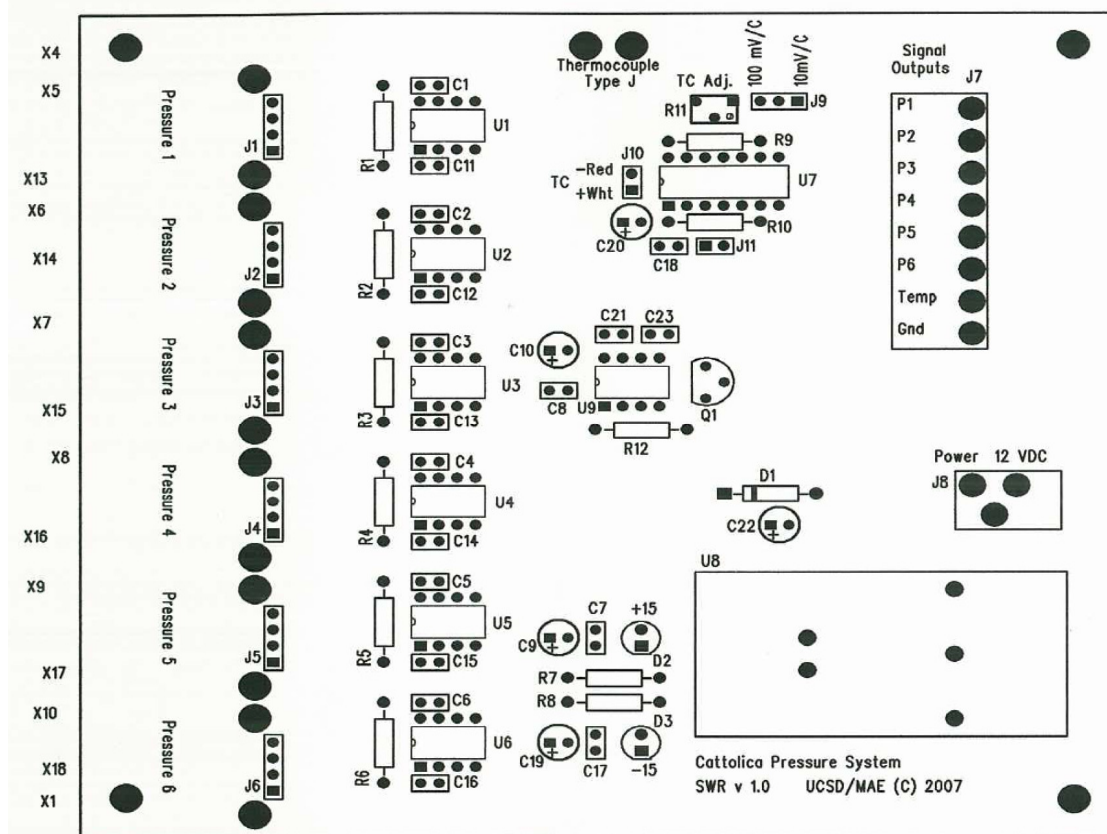


Figure A.2: Signal processing circuit board schematic

Table A.1: Bill of materials for signal processing circuit

Item #	Ref. #	Qty.	Part Name	Description	Value
1	Q1	1	2N3906	GENERAL PURPOSE PNP SILICON TRANSISTOR	
2	U9	1	AD587	HIGH PRECISION 10V REFERENCE	
3	U7	1	AD594	TYPE J THERMOCOUPLY CONDITIONER IC	
4	U8	1	CALEXE1	DC-DC CONVERTER (12VDC TO +/- 15VDC)	
5	C1	1	CAPCERSM	CERAMIC CAP SMALL .100 CENTERS	.1 μ F
6	C2	1	CAPCERSM	CERAMIC CAP SMALL .100 CENTERS	.1 μ F
7	C3	1	CAPCERSM	CERAMIC CAP SMALL .100 CENTERS	.1 μ F
8	C4	1	CAPCERSM	CERAMIC CAP SMALL .100 CENTERS	.1 μ F
9	C5	1	CAPCERSM	CERAMIC CAP SMALL .100 CENTERS	.1 μ F
10	C6	1	CAPCERSM	CERAMIC CAP SMALL .100 CENTERS	.1 μ F
11	C7	1	CAPCERSM	CERAMIC CAP SMALL .100 CENTERS	.1 μ F
12	C8	1	CAPCERSM	CERAMIC CAP SMALL .100 CENTERS	.1 μ F
13	C11	1	CAPCERSM	CERAMIC CAP SMALL .100 CENTERS	.1 μ F
14	C12	1	CAPCERSM	CERAMIC CAP SMALL .100 CENTERS	.1 μ F
15	C13	1	CAPCERSM	CERAMIC CAP SMALL .100 CENTERS	.1 μ F
16	C14	1	CAPCERSM	CERAMIC CAP SMALL .100 CENTERS	.1 μ F
17	C15	1	CAPCERSM	CERAMIC CAP SMALL .100 CENTERS	.1 μ F
18	C16	1	CAPCERSM	CERAMIC CAP SMALL .100 CENTERS	.1 μ F
19	C17	1	CAPCERSM	CERAMIC CAP SMALL .100 CENTERS	.1 μ F
20	C18	1	CAPCERSM	CERAMIC CAP SMALL .100 CENTERS	.1 μ F
21	C21	1	CAPCERSM	CERAMIC CAP SMALL .100 CENTERS	.1 μ F
22	C23	1	CAPCERSM	CERAMIC CAP SMALL .100 CENTERS	.1 μ F
23	C9	1	CAPTANT	DECOUP CAP RADIAL BODY: .270 X .130	10 μ F

24	C10	1	CAPTANT	DECOUP CAP RADIAL BODY: .270 X .130	10 μ F
25	C19	1	CAPTANT	DECOUP CAP RADIAL BODY: .270 X .130	10 μ F
26	C20	1	CAPTANT	DECOUP CAP RADIAL BODY: .270 X .130	10 μ F
27	C22	1	CAPTANT	DECOUP CAP RADIAL BODY: .270 X .130	220 μ F
28	J10	1	CONSIP-4P	GENERIC 2 PIN SIP HEADER .100 CENTERS	
29	J11	1	CONSIP-4P	GENERIC 2 PIN SIP HEADER .100 CENTERS	
30	J8	1	CONSIP-4P	GENERIC 2 PIN SIP HEADER .100 CENTERS	
31	J9	1	CONSIP-4P	GENERIC 2 PIN SIP HEADER .100 CENTERS	
32	J1	1	CONSIP-4P	GENERIC 2 PIN SIP HEADER .100 CENTERS	
33	J2	1	CONSIP-4P	GENERIC 2 PIN SIP HEADER .100 CENTERS	
34	J3	1	CONSIP-4P	GENERIC 2 PIN SIP HEADER .100 CENTERS	
35	J4	1	CONSIP-4P	GENERIC 2 PIN SIP HEADER .100 CENTERS	
36	J5	1	CONSIP-4P	GENERIC 2 PIN SIP HEADER .100 CENTERS	
37	J6	1	CONSIP-4P	GENERIC 2 PIN SIP HEADER .100 CENTERS	
38	J7	1	CONRA-8P	RIGHT ANGLE 8-PIN M/F HORIZON PCB CONN	
39	D1	1	DIODE	GENERIC RECTIFYING DIODE 1N4003 TYP.	
40	U1	1	INAMP8	BURR-BROWN (TEXAS INST) INA114 Inst. Amp.	
41	U2	1	INAMP8		
42	U3	1	INAMP8		
43	U4	1	INAMP8		
44	U5	1	INAMP8		
45	U6	1	INAMP8		
46	D2	1	LEDX	LIGHT EMITTING DIODE3	
47	D3	1	LEDX	LIGHT EMITTING DIODE	
48	X1	1	MTHOLE	MOUNTING HOLE	
49	X2	1	MTHOLE	"	
50	X3	1	MTHOLE	"	
51	X4	1	MTHOLE	"	
52	X5	1	MTHOLE	"	
53	X6	1	MTHOLE	"	
54	X7	1	MTHOLE	"	
55	X8	1	MTHOLE	"	
56	X9	1	MTHOLE	"	
57	X10	1	MTHOLE	"	
58	X11	1	MTHOLE	"	
59	X12	1	MTHOLE	"	
60	X13	1	MTHOLE	"	
61	X14	1	MTHOLE	"	
62	X15	1	MTHOLE	"	
63	X16	1	MTHOLE	"	
64	X17	1	MTHOLE	"	
65	X18	1	MTHOLE	"	
66	R1	1	RES-1/4W	RES BODY: 100 CENTERS: 500	84.5
67	R2	1	RES-1/4W	RES BODY: 100 CENTERS: 500	84.5
68	R3	1	RES-1/4W	RES BODY: 100 CENTERS: 500	249
69	R4	1	RES-1/4W	RES BODY: 100 CENTERS: 500	249
70	R5	1	RES-1/4W	RES BODY: 100 CENTERS: 500	249
71	R6	1	RES-1/4W	RES BODY: 100 CENTERS: 500	499
72	R7	1	RES-1/4W	RES BODY: 100 CENTERS: 500	1.5k
73	R8	1	RES-1/4W	RES BODY: 100 CENTERS: 500	1.5k
74	R9	1	RES-1/4W	RES BODY: 100 CENTERS: 500	365k
75	R10	1	RES-1/4W	RES BODY: 100 CENTERS: 500	10k
76	R12	1	RES-1/4W	RES BODY: 100 CENTERS: 500	220
77	R11	1	TRIMPOT	TRIMPOT 3 PINS	100k

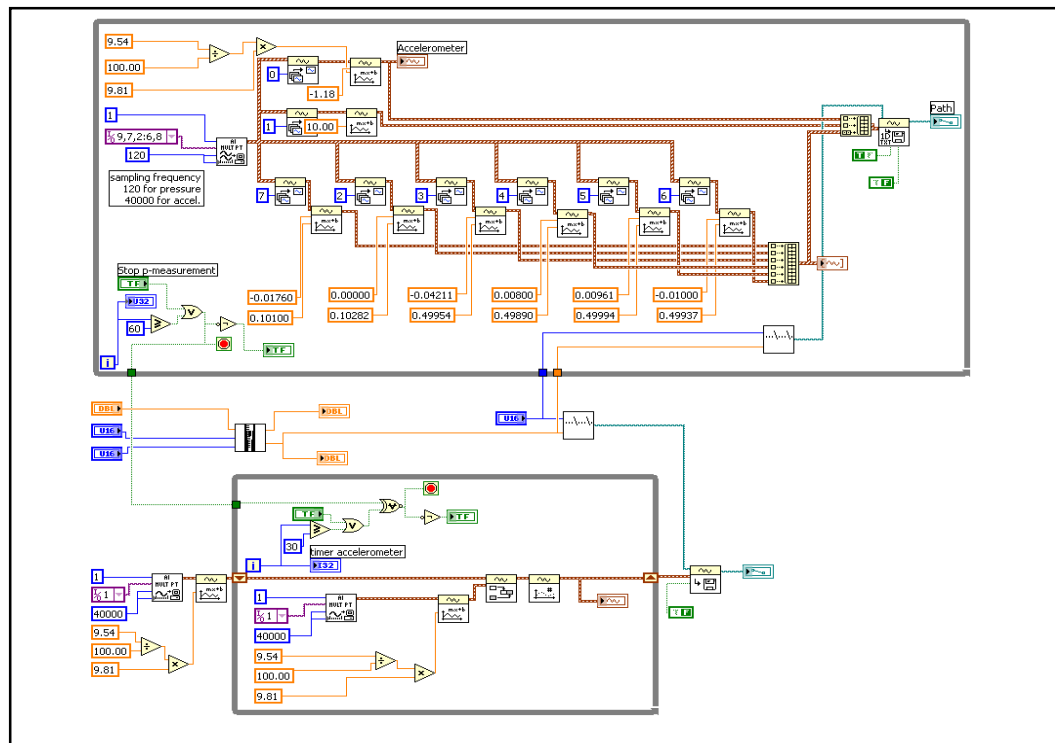


Figure A.3: Schematic of LabVIEW vi used to capture accelerometer and pressure data and write to file

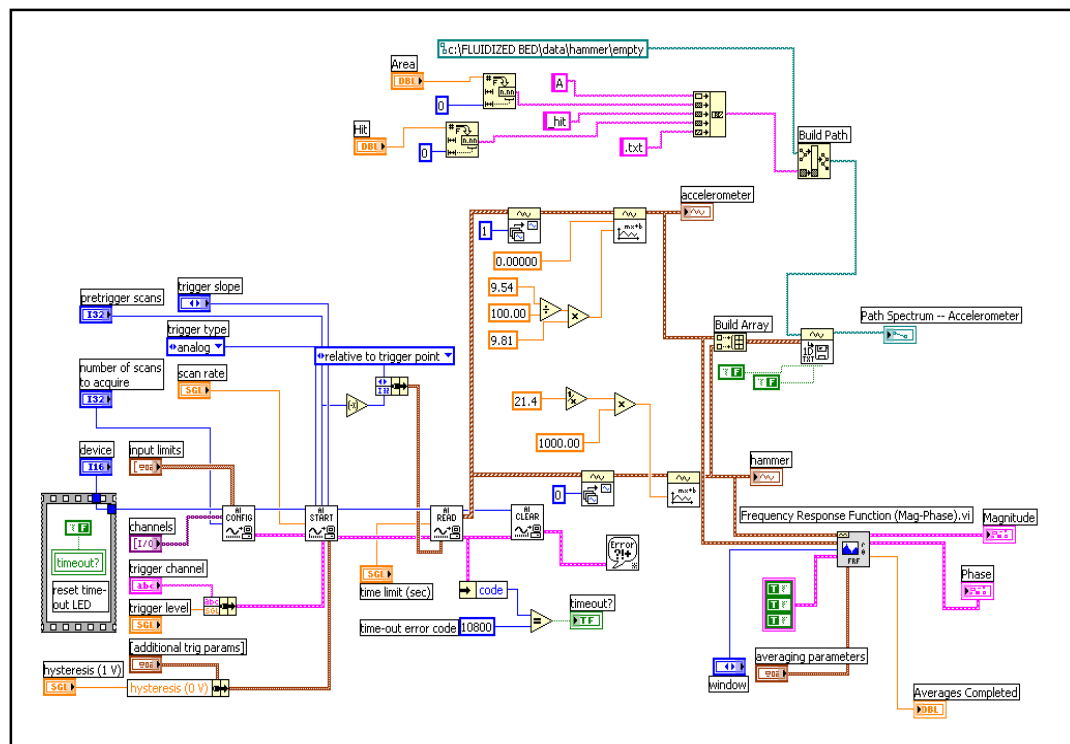


Figure A.4: Schematic of LabVIEW vi used to capture accelerometer and impulse hammer data and compute the transfer function

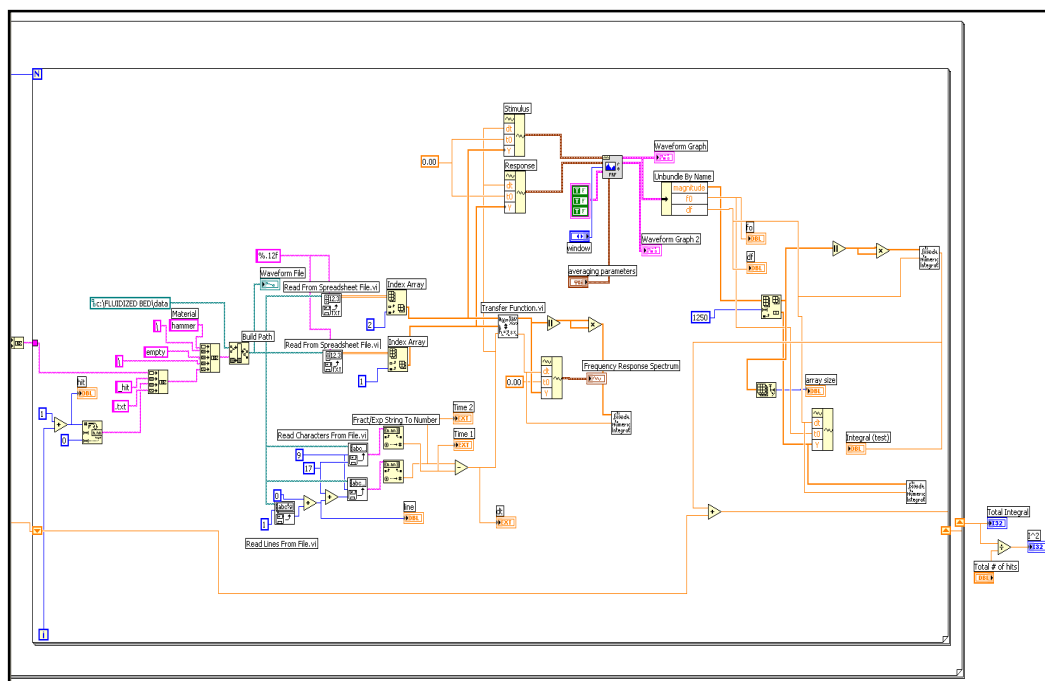


Figure A.5: Schematic of LabVIEW vi used to calculate average transfer functions by specified region, as well as calculate I^2 values

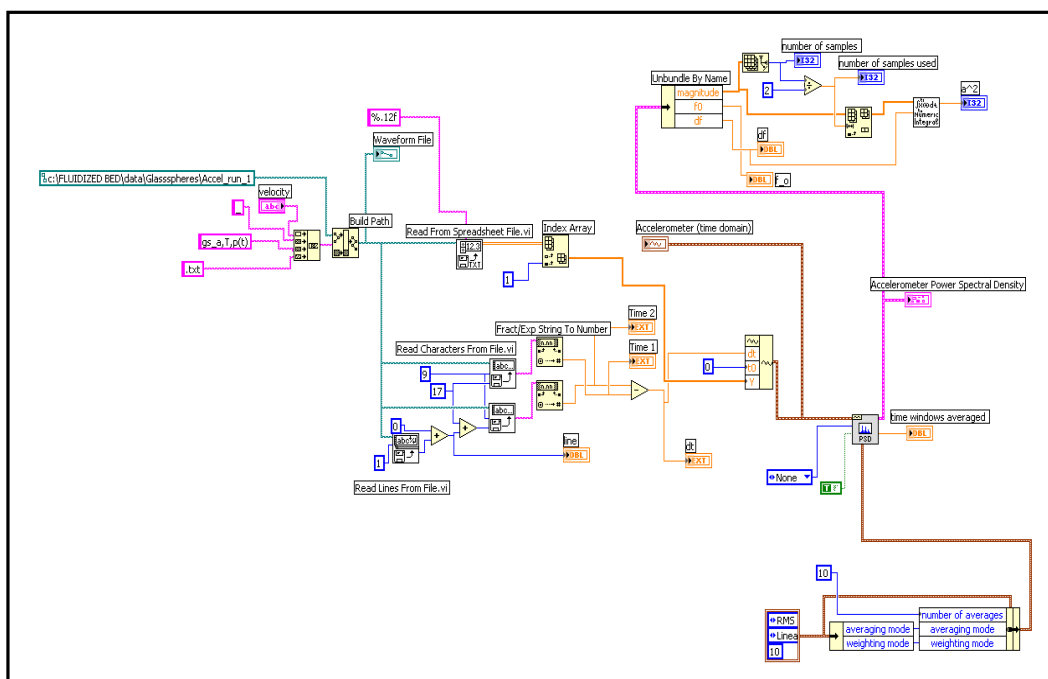
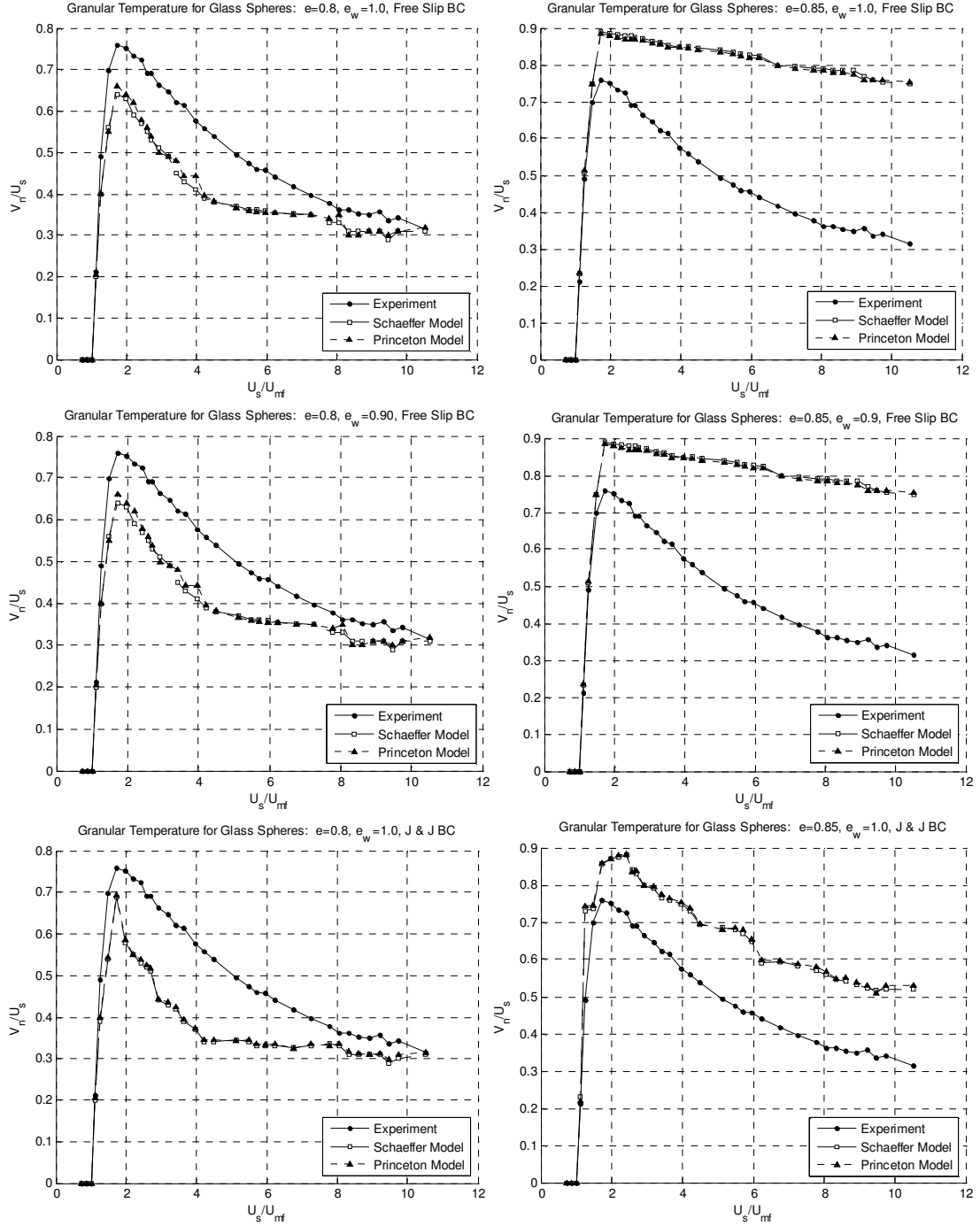
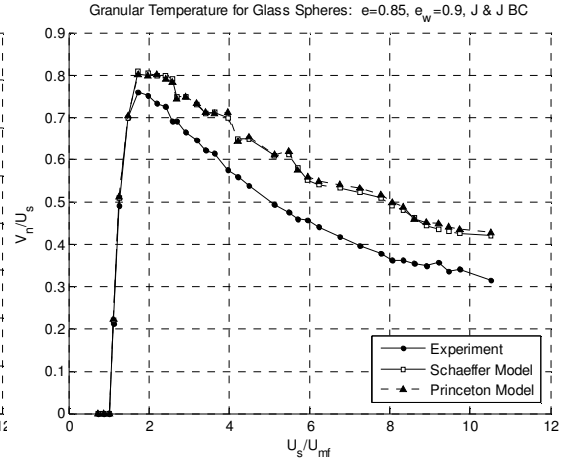
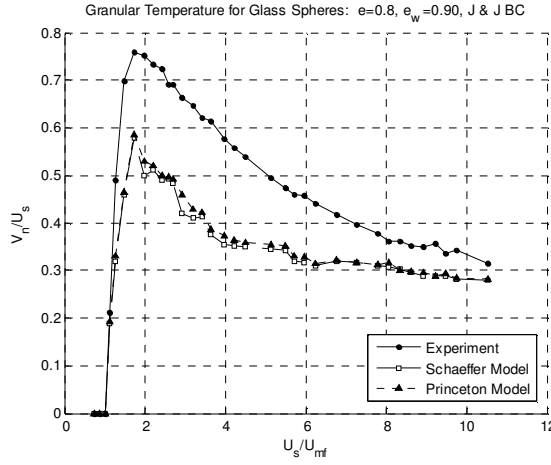


Figure A.6: Schematic of LabVIEW vi used to calculate the acceleration PSD of accelerometer time signals, and compute a^2 values

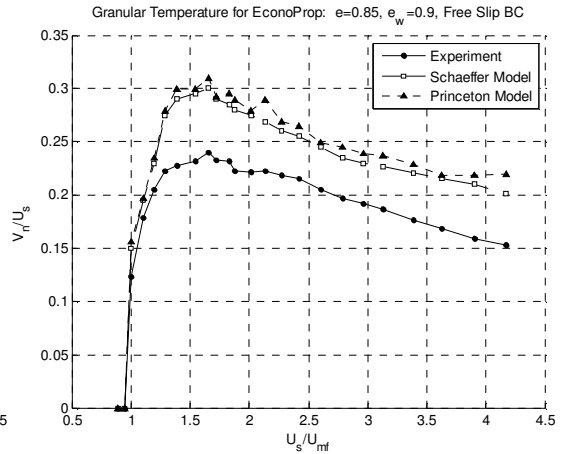
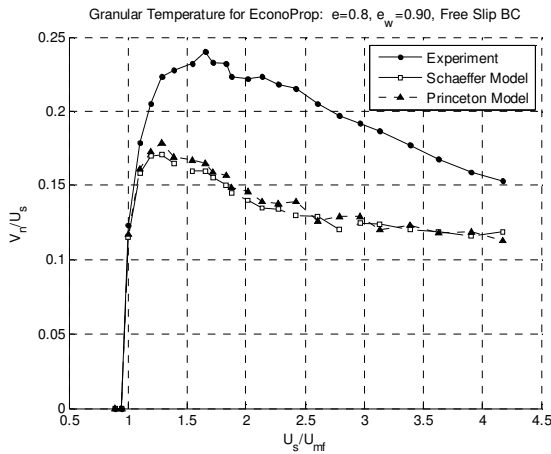
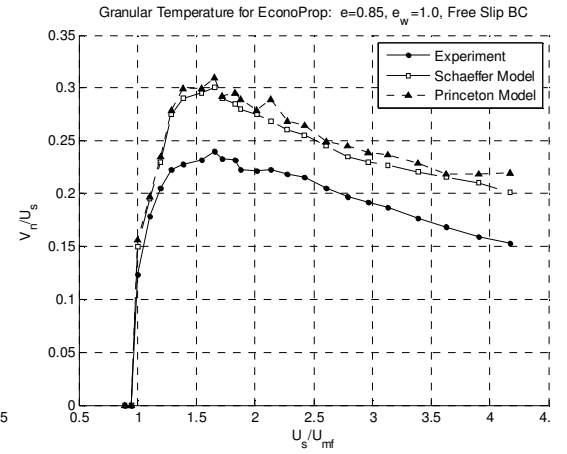
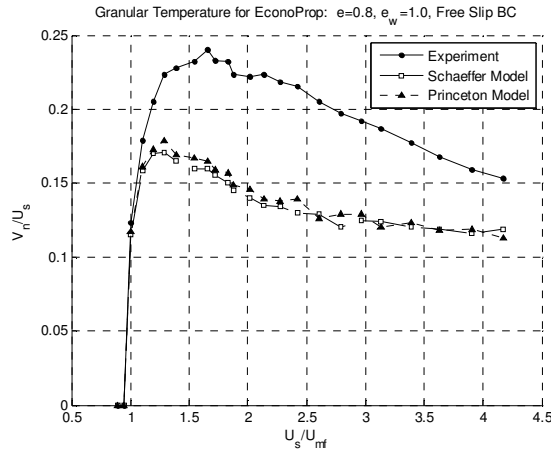
Appendix B: Experimental and Simulated Particle Normal Velocity Plots

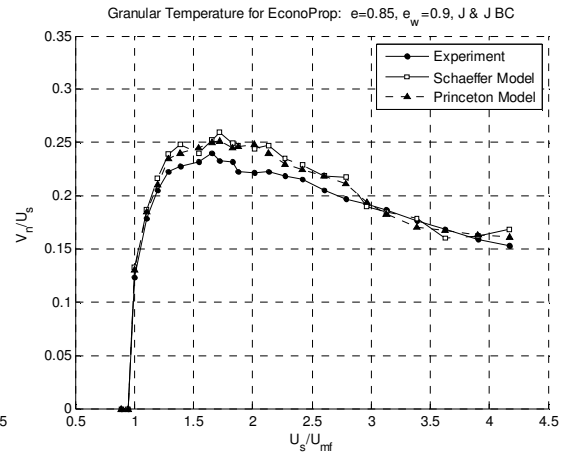
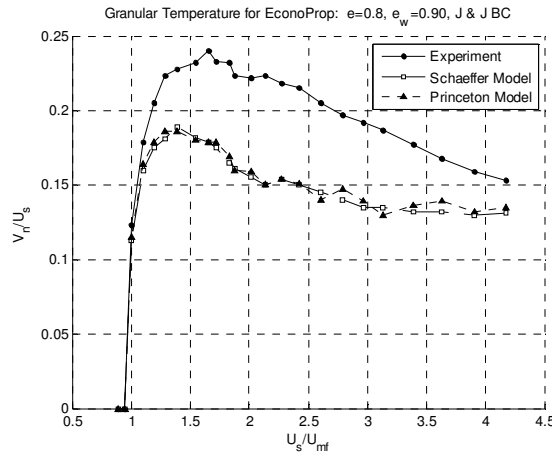
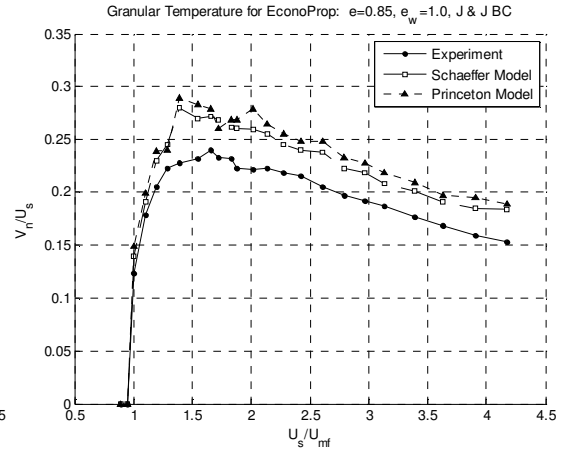
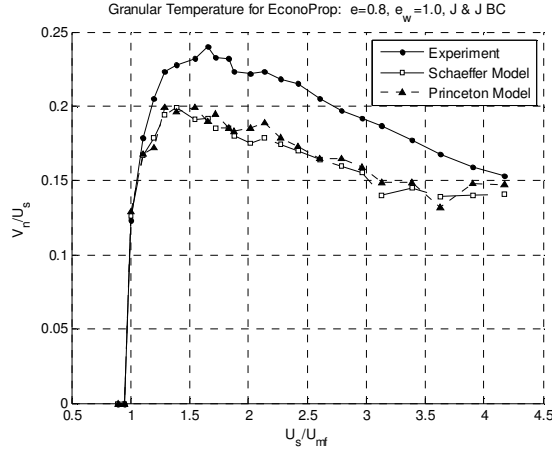
Glass Spheres



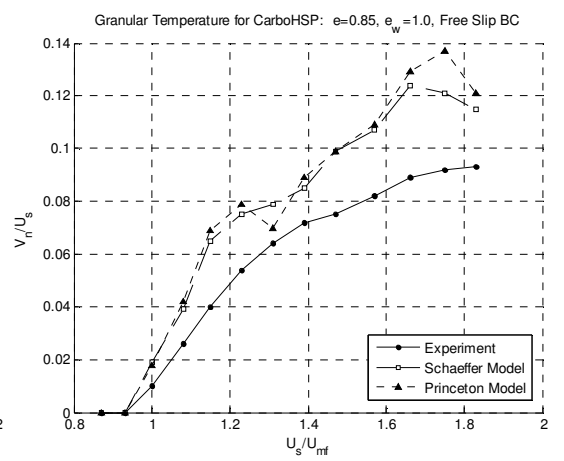
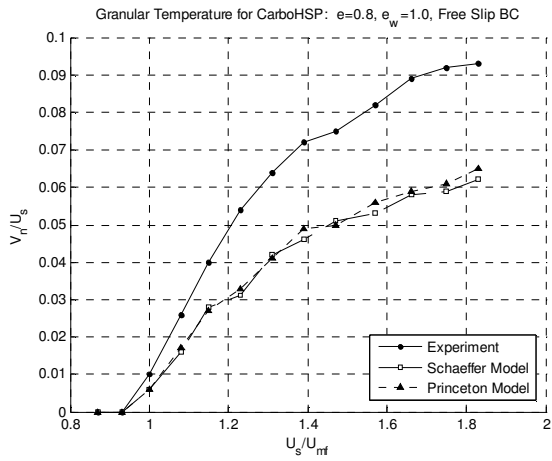


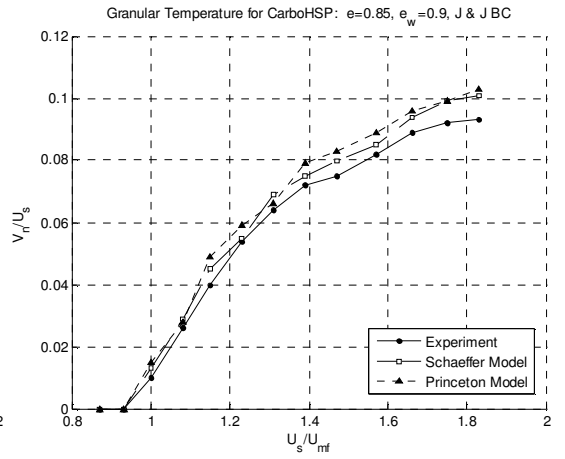
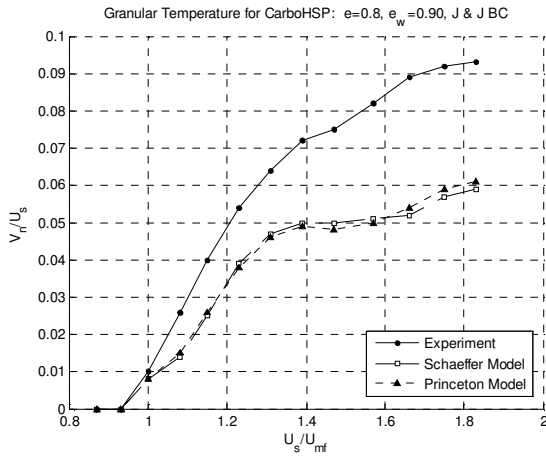
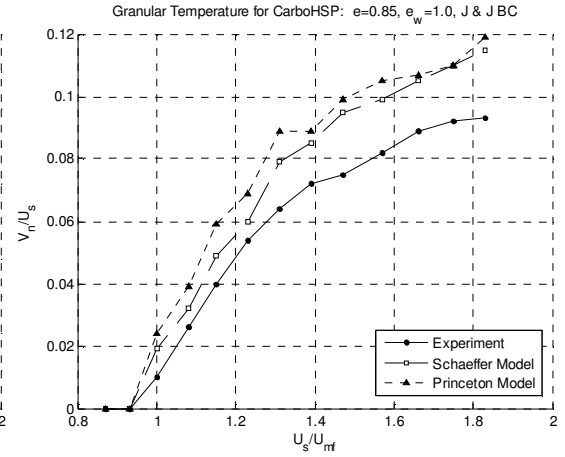
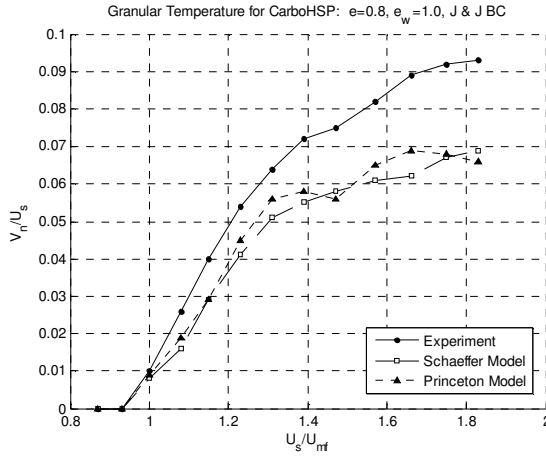
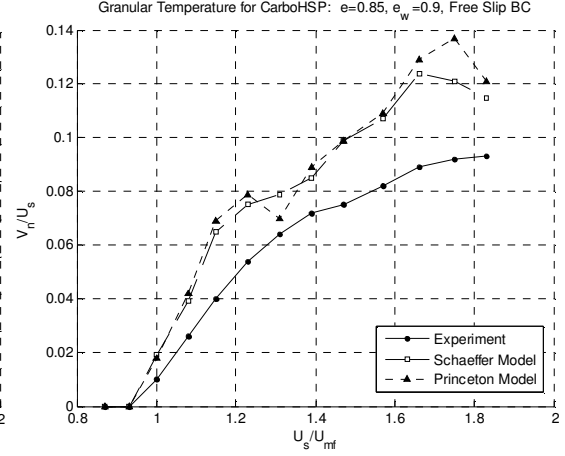
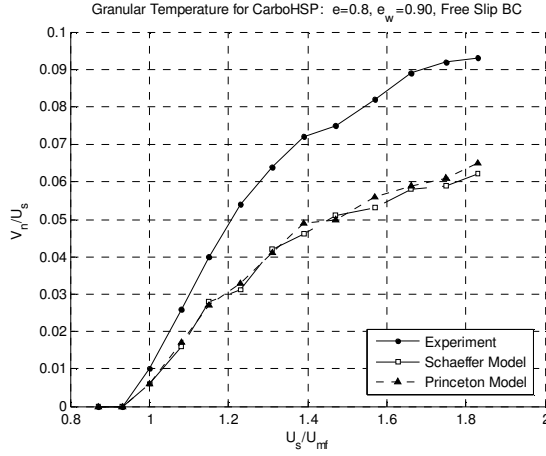
EconoProp





CarboHSP





References

- Bi, Hsiaotao T. 2007. A critical review of the complex pressure fluctuation phenomenon in gas-solids fluidized beds. *Chemical Engineering Science*, **62**(13), 3473–3493.
- Biggs, Mark, Glass, Don, Xie, L., Zivkovic, Vladimir, Buts, Alex, & Curt Kounders, M. 2008. Granular temperature in a gas fluidized bed. *Granular Matter*, **10**(2), 63–73.
- Campbell, C S. 1990. Rapid Granular Flows. *Annual Review of Fluid Mechanics*, **22**(1), 57–90.
- Campbell, C S, & Rahman, K. 1992. An improved particle pressure transducer. *Measurement Science and Technology*, **3**(8), 709–712.
- Cody, G. D., Goldfarb, D. J., Storch, G. V., & Norris, A. N. 1996. Particle granular temperature in gas fluidized beds. *Powder Technology*, **87**(3), 211–232.
- Cody, G. D., Bellows, R. J., Goldfarb, D. J., Wolf, H. A., & Storch, G. V. 2000. A novel non-intrusive probe of particle motion and gas generation in the feed injection zone of the feed riser of a fluidized bed catalytic cracking unit. *Powder Technology*, **110**(1-2), 128–142.
- Cody, George D., Johri, Jayati, & Goldfarb, David. 2008. Dependence of particle fluctuation velocity on gas flow, and particle diameter in gas fluidized beds for monodispersed spheres in the Geldart B and A fluidization regimes. *Powder Technology*, **182**(2), 146–170.
- Didwania, A. 2008. *Private communications*.
- Didwania, A. 2009. *Private communications*.
- Didwania, A. 2010. *Private communications*.
- Didwania, A., Mandich, K., Cattolica, R., (to appear), Wall Granular Temperature in a Bubbling Fluidized Bed: Simulations and Acoustic Shot Noise Experiments, *To Be Submitted to Chemical Engineering Science*
- Dijkhuizen, W., Bokkers, G. A., Deen, N. G., van Sint Annaland, M., & Kuipers, J. A. M. 2007. Extension of PIV for measuring granular temperature field in dense fluidized beds. *AIChE Journal*, **53**(1), 108–118.
- Durian, Douglas J. 1997. Particle Motions in a Gas-Fluidized Bed of Sand. *Phys. Rev. Lett.*, **79**(18), 3407–.
- S. Ergun, Fluid flow through packed columns, *Chem. Eng. Prog.*, **48**, 89 (1952)
- Fluent. 2005 (January). *Fluent 6.2 user guide*. Fluent Inc.
- Geldart, D. 1973. Types of gas fluidization. *Powder Technology*, **7**(5), 285–292.
- Gidaspow, D. 1994. *Multiphase Flow and Fluidization*. Academic Press.

- Goldhirsch, Isaac. 2008. Introduction to granular temperature. *Powder Technology*, **182**(2), 130–136.
- Hofbauer, H. *Wirbelschichttechnik, Unterlagen zur Vorlesung, 4.Auflage*.
- Horowitz, P., & Hill, W. 1989. *The Art of Electronics*. second edn. Cambridge University Press.
- Johnson, P.C. and Jackson, R., 1987, Frictional-collisional constitutive relations for granular materials with application to plane shearing, *Journal of Fluid Mechanics* **176** (1987), pp. 67–93.
- Jung, J., Gidaspow, D., & Gamwo, I.K. 2005. Measurement of Two Kinds of Granular Temperatures, Stresses, and Dispersion in Bubbling Beds. *Industrial & Engineering Chemistry Research*, **44**(5), 1329–1341.
- Kravanja, P., *Cold flow studies in a stationary gas-solid fluidized bed*, Master's thesis, 2008.
- Kunii, D., & Levenspiel, O. 1991. *Fluidization Engineering*. Butterworth-Heinemann.
- Landau, L.D., and Lifshitz, E.M., *Theory of Elasticity*, Pergamon, Oxford, 2nd edn., 1970
- M'chirgui, A., Tadrist, H., & Tadrist, L. 1997. Experimental investigation of the instabilities in a fluidized bed origin of the pressure fluctuations. *Physics of Fluids*, **9**(3), 500–509.
- Newland, D.E. 1993. *An introduction to random vibrations, spectral and wavelet analysis*. 3 edn. Longman Scientific & Technical.
- NI. 2000 (July). *LabVIEW Measurements Manual*. National Instruments.
- NI. 2004 (March). *LabVIEW Analysis concepts*. National Instruments.
- Nicastro, M. T., & Glicksman, L. R. 1984. Experimental verification of scaling relationships for fluidized bed. *Chemical Engineering Science*, **39**(9), 1381–1391.
- Ogawa, Satoru, Umemura, Akira, & Oshima, Nobunori. 1980. On the equations of fully fluidized granular materials. *Zeitschrift für Angewandte Mathematik und Physik (ZAMP)*, **31**(4), 483–493.
- Paschedag, Anja R. 2004. *CFD in der Verfahrenstechnik - Allgemeine Grundlagen und mehrphasige Anwendungen*. Wiley VCH Verlag GmbH & Co KGaA.
- Polashenski, William, & Chen, John C. 1997. Normal solid stress in fluidized beds. *Powder Technology*, **90**(1), 13–23.
- Puncochar, A., *et al.* 1985. EVALUATION OF MINIMUM FLUIDIZING VELOCITY IN GAS FLUIDIZED BED FROM PRESSURE FLUCTUATIONS*. *Chemical Engineering Communications*, **35**(1), 81–87.
- Ranade, Vivek V. 2002. *COMPUTATIONAL FLOW MODELING FOR CHEMICAL REACTOR ENGINEERING*. Academic Press.

- Randall, R.B. 1987. *Frequency analysis*. Brüel&Kjaer.
- Reh, L. 1968. Verbrennung in der Wirbelschicht. *Chemie Ingenieur Technik - CIT*, **40**(11), 509–515.
- Sasic, Srdjan, Leckner, Bo, & Johnsson, Filip. 2007. Characterization of fluid dynamics of fluidized beds by analysis of pressure fluctuations. *Progress in Energy and Combustion Science*, **33**(5), 453–496.
- Schaeffer, D.G., 1987. Instability in the evolution equations describing incompressible granular flow. *Journal of Differential Equations* **66**, 61–74.
- Srivastava, A. and Sundaresan, S., 2003 A, Analysis of a frictional–kinetic model for gas–particle flow, *Powder Technology* **129** (1–3) (2003), pp. 72–85
- Syamlal, M., Rogers, W., & O'Brian, T.J. 1993 (December). *MFIX Documentation Theory Guide Technical Note*. U.S. Department of Energy Office of Fossil Energy, Morgantown Energy Technology Center P.O. Box 880 Morgantown, West Virginia 26507-0880.
- F. Taghipour, N. Ellis and C. Wong, Experimental and computational study of gas–solid fluidized bed hydrodynamics, *Chemical Engineering Science* **60** (24) (2005), pp. 6857–6867.
- Tartan, Mehmet, & Gidaspow, Dimitri. 2004. Measurement of granular temperature and stresses in risers. *AIChE Journal*, **50**(8), 1760–1775.
- van der Schaaf, J., Schouten, J. C., Johnsson, F., & van den Bleek, C. M. 2002. Non-intrusive determination of bubble and slug length scales in fluidized beds by decomposition of the power spectral density of pressure time series. *International Journal of Multiphase Flow*, **28**(5), 865–880.
- van der Ziel, A., and Kailath, T., *Noise: Sources, Characterization, Measurement*, Prentice Hall, Englewood Cliffs, NJ, 1970
- van Ommen, J. Ruud, Schouten, Jaap C., vander Stappen, Michel L. M., & van den Bleek, Cor M. 1999. Response characteristics of probe-transducer systems for pressure measurements in gas-solid fluidized beds: how to prevent pitfalls in dynamic pressure measurements. *Powder Technology*, **106**(3), 199–218.
- van Wachem, B. G. M., van der Schaaf, J., Schouten, J. C., Krishna, R., & van den Bleek, C. M. 2001. Experimental validation of Lagrangian-Eulerian simulations of fluidized beds. *Powder Technology*, **116**(2-3), 155–165.
- Wildman, R. D., & Huntley, J. M. 2000. Novel method for measurement of granular temperature distributions in two-dimensional vibro-fluidised beds. *Powder Technology*, **113**(1-2), 14–22.
- Xie, H. Y., & Geldart, D. 1997. The response time of pressure probes. *Powder Technology*, **90**(2), 149–151.

Xie, L., Biggs, M. J., Glass, D., McLeod, A. S., Egelhaaf, S. U., & Petekidis, G. 2006. Granular temperature distribution in a gas fluidized bed of hollow microparticles prior to onset of bubbling. *EPL (Europhysics Letters)*, **74**(2), 268–274.